

UC Davis

UC Davis Electronic Theses and Dissertations

Title

Presentation of Physical and Chemical Cues from Microgel Scaffolds to Guide Cell Behavior

Permalink

<https://escholarship.org/uc/item/1dk77822>

Author

Lowen, Jeremy Michael

Publication Date

2023

Peer reviewed|Thesis/dissertation

Presentation of Physical and Chemical Cues from Microgel Scaffolds to Guide Cell
Behavior

By

JEREMY LOWEN
DISSERTATION

Submitted in partial satisfaction of the requirements for the degree of

DOCTOR OF PHILOSOPHY

in

Biomedical Engineering

in the

OFFICE OF GRADUATE STUDIES

of the

UNIVERSITY OF CALIFORNIA

DAVIS

Approved:

Kent Leach, Chair

Alyssa Panitch

Steven George

Eduardo Silva

Committee in Charge

2023

Acknowledgements

The completion of this work would not have been possible without the support from countless people. I would like to thank my advisor and mentor Dr. Kent Leach, who has motivated me to push through many of the challenges I have faced during my graduate work. He truly leads by example, and his dedication to research and passion for science inspires my own scientific pursuits. I would also like to thank my dissertation committee members for their invaluable feedback: Dr. Alyssa Panitch, Dr. Steven George, and Dr. Eduardo Silva. I am thankful to the many amazing members of the Leach Lab who have made performing research an enjoyable experience and made the laboratory a wonderful place to work in. I would also like to acknowledge UC Davis, a campus where I completed both my undergraduate and graduate degrees. The amazing community at UC Davis is a large part of the reason I chose to pursue my graduate work here, and the entire BMEGG community has lent invaluable support. Finally, I would like to thank my friends and family, who have provided a support net that has allowed me to accomplish so many of my goals. I could not have made it through graduate school without your friendship, love, and support.

Abstract

Hydrogels are commonly used in tissue engineering due to their biocompatibility, high water content, and similar mechanical properties to natural tissues. Traditional bulk hydrogels are hindered by nanoporosity which limits cell migration and interaction. While porosity can be introduced with strategies such as porogen leaching or freeze-drying, these steps are often incompatible with cells and limit the injectability of the hydrogel. Granular, microgel annealed scaffolds are an emerging platform which addresses these issues due to their modularity and inherent microporous void space. The ability to tune individual microgels allows for complex scaffold designs well suited to heterogeneous tissue found throughout the body. This work establishes a rapid annealing method for fabricating microgel scaffolds and investigates how microgel size, stiffness, and biochemical cues can be tuned to influence cell spreading and phenotype.

First, we developed a light-based technique for rapidly annealing microgels across a range of diameters. Utilizing 8-arm PEG-vinyl sulfone, we stoichiometrically controlled the number of arms available for crosslinking, functionalization, and annealing. We fabricated small and large microgels to explore how microgel diameter impacts void space and the role of porosity on cell spreading, cell aggregation, and macrophage polarization. Mesenchymal stromal cells (MSCs) spread rapidly in both formulations, yet the smaller microgels supported a higher cell density. When seeded with macrophages, the smaller microgels promoted an M1 phenotype, while larger microgels promoted a more regenerative M2 phenotype. As another application, we leveraged the inherent porosity of annealed microgels to induce cell aggregation. Finally, we implanted our microgels to examine how different size microgels influence endogenous cell invasion and

macrophage polarization. The use of ultraviolet light allows for microgels to be noninvasively injected into a desired mold or wound defect before annealing, and microgels of different properties combined to create a heterogeneous scaffold.

We next use our established microgel platform to develop microgels for the repair of bone and cartilage using instructive peptides and changes in stiffness to create osteogenic and chondrogenic microgels, respectively. The microgels outperformed bulk hydrogel controls evidenced by significant upregulation of osteogenic and chondrogenic markers by MSCs. We leveraged this microgel platform to create a bilayer scaffold and assess the ability of microgels to spatially control the differentiation of MSCs. Osteochondral bilayer scaffolds exhibited distinct regions of osteogenic and chondrogenic differentiation as a function of microgel population. Spatial transcriptomics confirmed osteogenic and chondrogenic genes were upregulated in their respective microgel regions. These studies highlight the modularity of microgels and the importance of microporous void space.

Finally, we combined microgels with poly(3,4-ethylenedioxythiophene) polystyrene sulfonate (PEDOT:PSS) to explore the interplay of void volume and conductivity to synergistically promote myogenic differentiation. PEDOT:PSS increased the conductivity of microgels over 2-fold while maintaining stiffness, annealing strength, and viability of associated myoblastic cells. Murine C2C12 myoblasts exhibited an upregulation of the late-stage differentiation marker myosin heavy chain as a function of both porosity and conductivity. The earlier stage marker, myogenin, was influenced only by porosity. Human skeletal muscle derived cells upregulated Myod1, IGF-1, and IGFBP-2, at earlier timepoints on conductive microgel scaffolds compared to non-conductive scaffolds.

These data further demonstrate how the inherent porosity in microgel scaffolds is beneficial to cell differentiation.

Collectively, this dissertation demonstrates the versatility of microgels to serve as an instructive niche to regulate cell function. The engineering of microgel scaffolds could direct cell spreading, macrophage phenotype, MSC differentiation, and myoblast differentiation. Microgel size, stiffness, and biochemical cues are all factors that can be tuned to match specific tissue properties.

Table of Contents

Acknowledgements	ii
Abstract	iii
Chapter 1: Introduction	1
1.1 Problem Statement	1
1.2 Hypothesis and Specific Aims	4
1.3 Significance	4
1.4 Thesis Overview	5
1.5 References	7
Chapter 2: Functionally graded biomaterials for use as model systems and replacement tissues	10
2.1 Introduction	10
2.2 Methods for the fabrication of functionally graded materials	13
2.3 Application of functionally graded materials in model systems and engineered tissues	39
2.4 Conclusion and Future Outlook	48
2.5 References	51
Chapter 3: Multisized Photoannealable Microgels Regulate Cell Spreading, Aggregation, and Macrophage Phenotype through Microporous Void Space	74
3.1 Introduction	74
3.2 Materials and Methods	76
3.3 Results and Discussion	86
3.4 Conclusion	109
3.5 References	111
Chapter 4: Osteogenic and Chondrogenic Microgels for Spatial Differentiation of Mesenchymal Stromal Cells	118
4.1 Introduction	118
4.2. Materials and methods	120
4.2.1 PEG-DWIVA fabrication	120
4.3 Results	127
4.4 Discussion	142
4.5 Conclusion	146
4.6 References	147

Chapter 5: Conductive microgel annealed scaffolds enhance myogenic potential of myoblastic cells	153
5.1 Introduction	153
5.2 Materials and Methods.....	155
5.3 Results.....	162
5.4 Discussion.....	173
5.5 References.....	178
Chapter 6: Results and Future Directions	185
6.1 Results and Implications	185
6.2 Future Directions and Limitations.....	187
6.3 Final Conclusions.....	190
6.4 References.....	191

Chapter 1: Introduction

1.1 Problem Statement

Hydrogels are a staple in tissue engineering due to their biocompatibility and structural similarity to tissues found in the body.^[1,2] Their high water content and tunability make them an ideal choice for culturing cells, with both natural and synthetic polymers being commonly used materials.^[3] Conventional hydrogels are crosslinked in bulk, resulting in a low surface-to-volume ratio and a nanoporous mesh size which can lead to poor cell infiltration.^[4,5] As a result, the inclusion of a porogen or a hydrolytic or matrix metalloproteinase (MMP)-sensitive crosslinker are often incorporated to enable cells to remodel their surrounding environment.^[6,7] However, these motifs can add additional steps to material synthesis and limit the injectability of the platform.

Recently, microgel annealed scaffolds have emerged as a promising alternative to bulk hydrogels, with microgel scaffolds possessing inherent porosity in the form of void space existing between the individual microparticles. Furthermore, microgel scaffolds decouple polymer properties from mesh size, allowing for independent tuning of factors such as stiffness or degradability from porosity. In addition to overcoming challenges posed by bulk hydrogels, microgels have the added benefits of modularity and injectability, making them a promising alternative for engineering heterogeneous scaffolds.

As microgel usage becomes more prominent, the options for microgel synthesis and assembly are rapidly expanding. Common methods of fabrication include microfluidics, batch emulsion, and extrusion fragmentation, each of which offer differences in polydispersity, mechanical strength, porosity, and injectability.^[5] Our lab

uses microfluidic production due to the high monodispersity they offer in terms of microgel diameter, which is important for exploring differences in void space.^[8,9] Of chief importance is how the microgels are annealed together. Common microgel assembly techniques often contain several primary drawbacks. The use of enzymatic catalysis to anneal microgels can take up to 90 minutes at elevated temperatures,^[8] which could limit clinical accessibility. Enzymatic catalysis may also require the use of costly reagents such as Factor XIII.^[8,10] Furthermore, the annealing strength of the particles may not be sufficient to withstand significant force. A robust and quick method to anneal microgels of different sizes is needed to increase clinical accessibility. Thus, we designed a system to strongly anneal microgels in as little as 1 minute.

An important parameter of microgel design is microparticle size. The diameter of the microgel directly contributes to how the particles pack together and therefore the resultant porosity. While the effects of porosity on cell migration and proliferation have been well studied in bulk hydrogels, it has yet to be thoroughly investigated in a microgel platform.^[7,11] Similarly, while changes in porosity have been shown to affect cell differentiation and even macrophage polarization in bulk hydrogels, the effect of microgel size on these phenotypes warrants further interrogation.^[12,13] As a result, we modeled how microgel diameter correlates to differences in void space and interrogated how different size microgels regulate cell spreading, aggregation, and macrophage phenotype.

After establishing how microgel diameter influences cell behavior, we next harnessed the modularity of microgels to form a heterogeneous scaffold for formation of osteochondral tissue. Osteochondral lesions involve both the articular cartilage and the

underlying subchondral bone. Damage to the subchondral bone can introduce fissures that penetrate calcified cartilage resulting in the exchange of cytokines and prostaglandins that further result in tissue damage.^[14] Common treatments for osteochondral repair include microfracture and autologous or allogenic chondrocyte implantation. However, these have drawbacks of fibrocartilage formation which is mechanically inferior, donor site morbidity, and tissue availability, respectively.^[15-17] Therefore, we designed an osteochondral bilayer scaffold composed of osteogenic and chondrogenic microgels to spatially control differentiation of mesenchymal stromal cells (MSCs). While previous work has investigated microgels with different levels of mineralization for osteochondral repair,^[18] we interrogated the novel combination of mechanical cues and instructive peptides to direct MSCs.

Finally, we considered the application of microgels for muscle tissue engineering. The current gold standard of treatment is the autologous muscle graft which results in donor site morbidity.^[19] Tissue engineering aims to provide an alternative treatment, with electrically conductive biomaterials gaining rapid popularity due to their ability to direct cell differentiation and maturation and capitalize on the inherent bioelectricity of muscle tissue.^[20] Previously, microgels have been mixed with silver nanoparticles to form a conductive mixture that could be 3D printed.^[21] However, the influence of conductive microgels on muscle cell regeneration was not examined. We added the conductive polymer poly(3,4-ethylenedioxythiophene) polystyrene sulfonate (PEDOT:PSS) to our microgels to investigate the interplay between microporosity and conductivity on myogenesis.

This dissertation focuses on developing a microgel platform that can be applied to several key issues in tissue engineering. We developed a method to rapidly anneal microgels, investigated the effect of different microgel sizes on cell phenotype, and designed microgels for repair of osteochondral and muscle tissues.

1.2 Hypothesis and Specific Aims

Hypothesis: Microgel size, stiffness, and bioinstructive cues can direct cell spreading, macrophage phenotype, MSC differentiation, and myoblast differentiation

Aim 1: Determine how microgel diameter influences cell spreading, aggregation, and macrophage polarization in an annealed scaffold.

Aim 2: Modulate microgel stiffness and peptide presentation to promote osteogenic and chondrogenic differentiation of MSCs.

Aim 3: Combine the microporosity of microgel scaffolds with the conductivity of PEDOT:PSS to enhance myogenic differentiation.

1.3 Significance

The successful completion of these studies contributes to the toolbox of biomaterials for tissue engineers. Microgels are a highly versatile platform, with widespread potential due to their modularity and tunability.^[22] Compared to enzymatic assembly methods, our light-based annealing technique which assembles microgels in

one minute greatly increases the ease-of-use of this platform. Furthermore, the ability to cryopreserve microgels without losing functionality alongside their injectability improves their clinical accessibility. Given these advantages, the potential for microgel annealed scaffolds to become a standard platform over conventionally used bulk hydrogels is immense.

Aim 1 seeks to understand how differences in microgel diameter influence cell spreading and macrophage polarization. Aim 2 builds on our understanding of microgel diameter and further functionalizes microgels with instructive peptides and mechanical cues to direct MSC differentiation with applications toward osteochondral scaffolds. Aim 3 adds PEDOT:PSS as an additional functional moiety to promote myogenesis. These aims combine to showcase how different microgel characteristics such as size, stiffness, and biochemical cues can be used to instruct cells. Overall, this dissertation establishes unique microgel chemistry and showcases how microgels can be applied to several clinically relevant cell types.

1.4 Thesis Overview

Chapter 2 discusses the importance of functionally graded materials in tissue engineering and emphasizes how the natural heterogeneity throughout the body can benefit from a biomaterial which is highly tunable and versatile. Chapter 3 will present data from Aim 1 including microgel annealing, and how microgel size can influence cell phenotype including macrophage polarization. Chapter 4 presents data from Aim 2 and discusses the fabrication of osteogenic and chondrogenic microgels. Chapter 5 presents results from Aim 3 which includes the creation of electrically conductive microgels for

myogenesis. Chapter 6 highlights conclusions and limitations of these studies and discusses future directions.

1.5 References

- [1] K.Y. Lee, D.J. Mooney, Hydrogels for Tissue Engineering, *Chem. Rev.* 101 (2001) 1869–1880.
- [2] S. Chaudhary, E. Chakraborty, Hydrogel based tissue engineering and its future applications in personalized disease modeling and regenerative therapy, *Beni-Suef Univ. J. Basic Appl. Sci.* 11 (2022) 3.
- [3] I.M. El-Sherbiny, M.H. Yacoub, Hydrogel scaffolds for tissue engineering: Progress and challenges, *Glob. Cardiol. Sci. Pract.* 2013 (2013) 38.
- [4] Q. Feng, D. Li, Q. Li, X. Cao, H. Dong, Microgel assembly: Fabrication, characteristics and application in tissue engineering and regenerative medicine, *Bioact. Mater.* 9 (2022) 105–119.
- [5] V.G. Muir, T.H. Qazi, J. Shan, J. Groll, J.A. Burdick, Influence of Microgel Fabrication Technique on Granular Hydrogel Properties, *ACS Biomater. Sci. Eng.* 7 (2021) 4269–4281.
- [6] M.P. Lutolf, J.L. Lauer-Fields, H.G. Schmoekel, A.T. Metters, F.E. Weber, G.B. Fields, J.A. Hubbell, Synthetic matrix metalloproteinase-sensitive hydrogels for the conduction of tissue regeneration: Engineering cell-invasion characteristics, *Proc. Natl. Acad. Sci. U.S.A.* 100 (2003) 5413–5418.
- [7] N. Annabi, J.W. Nichol, X. Zhong, C. Ji, S. Koshy, A. Khademhosseini, F. Dehghani, Controlling the Porosity and Microarchitecture of Hydrogels for Tissue Engineering, *Tissue Eng., Part B.* 16 (2010) 371–383.

- [8] J.M. de Rutte, J. Koh, D. Di Carlo, Scalable High-Throughput Production of Modular Microgels for In Situ Assembly of Microporous Tissue Scaffolds, *Adv. Funct. Mater.* 29 (2019) 1900071.
- [9] J.M. Lowen, G.C. Bond, K.H. Griffin, N.K. Shimamoto, V.L. Thai, J.K. Leach, Multisized Photoannealable Microgels Regulate Cell Spreading, Aggregation, and Macrophage Phenotype through Microporous Void Space, *Adv. Healthcare Mater.* (2023) 2202239.
- [10] D.R. Griffin, W.M. Weaver, P.O. Scumpia, D. Di Carlo, T. Segura, Accelerated wound healing by injectable microporous gel scaffolds assembled from annealed building blocks, *Nat. Mater.* 14 (2015) 737–744.
- [11] C. Ji, A. Khademhosseini, F. Dehghani, Enhancing cell penetration and proliferation in chitosan hydrogels for tissue engineering applications, *Biomaterials.* 32 (2011) 9719–9729.
- [12] M. Dadsetan, T.E. Hefferan, J.P. Szatkowski, P.K. Mishra, S.I. Macura, L. Lu, M.J. Yaszemski, Effect of hydrogel porosity on marrow stromal cell phenotypic expression, *Biomaterials.* 29 (2008) 2193–2202.
- [13] W. Bu, Y. Wu, A.M. Ghaemmaghami, H. Sun, A. Mata, Rational design of hydrogels for immunomodulation, *Regener. Biomater.* 9 (2022) rbac009.
- [14] S.I.M. Lepage, N. Robson, H. Gilmore, O. Davis, A. Hooper, S. St. John, V. Kamesan, P. Gelis, D. Carvajal, M. Hurtig, T.G. Koch, Beyond Cartilage Repair: The Role of the Osteochondral Unit in Joint Health and Disease, *Tissue Engineering Part B: Reviews.* 25 (2019) 114–125.

- [15] A.R. Martín, J.M. Patel, H.M. Zlotnick, J.L. Carey, R.L. Mauck, Emerging therapies for cartilage regeneration in currently excluded 'red knee' populations, *Npj Regener. Med.* 4 (2019) 12.
- [16] G.D. Smith, G. Knutsen, J.B. Richardson, A clinical review of cartilage repair techniques, *The Journal of Bone and Joint Surgery. British Volume.* 87-B (2005) 445–449.
- [17] E. Cavalli, C. Levinson, M. Hertl, N. Broguiere, O. Brück, S. Mustjoki, A. Gerstenberg, D. Weber, G. Salzmann, M. Steinwachs, G. Barreto, M. Zenobi-Wong, Characterization of polydactyly chondrocytes and their use in cartilage engineering, *Sci Rep.* 9 (2019) 4275.
- [18] P. Xia, S. Yan, G. Li, J. Yin, Preparation of Assemblable Chondral and Subchondral Bone Microtissues for Osteochondral Tissue Engineering, *ACS Appl. Mater. Interfaces.* 14 (2022)
- [19] S. Jana, S.K.L. Levengood, M. Zhang, Anisotropic Materials for Skeletal-Muscle-Tissue Engineering, *Adv. Mater.* 28 (2016) 10588–10612.
- [20] R. Dong, P.X. Ma, B. Guo, Conductive biomaterials for muscle tissue engineering, *Biomaterials.* 229 (2020) 119584.
- [21] M. Shin, K.H. Song, J.C. Burrell, D.K. Cullen, J.A. Burdick, Injectable and Conductive Granular Hydrogels for 3D Printing and Electroactive Tissue Support, *Adv. Sci.* 6 (2019) 1901229.
- [22] A.S. Caldwell, B.A. Aguado, K.S. Anseth, Designing Microgels for Cell Culture and Controlled Assembly of Tissue Microenvironments, *Adv. Funct. Mater.* 30 (2020) 1907670.

Chapter 2: Functionally graded biomaterials for use as model systems and replacement tissues

The purpose of this chapter is to provide the reader context for the studies in this dissertation. Herein, I discuss how tissues in the body are complex and can require heterogeneous materials for repair. I discuss established techniques for fabricating functionally graded materials and their applications. Given the recent emergence of microgels, there is a lack of research on heterogeneous microgel scaffolds which motivates the need for this research.

2.1 Introduction

Gradient-based biomaterials are an exciting advancement in the field of materials science and tissue engineering that are designed to mimic naturally occurring gradients in composition, signaling cues, and other constituents found *in vivo*. The advancement of technologies such as dynamic biomaterials, 3D bioprinters, and stem cell programming has fueled the growth of the tissue engineering field. Functionally graded materials (FGMs) represent one such advancement where biomaterials are designed to imitate the natural heterogeneity found in tissues throughout the body. In their simplest form, FGMs are composed of two constituent materials or phases which spatially change from one to the other. FGMs were first investigated in the 1980s for the design of heat-resistant materials for spacecraft that could withstand high temperature gradients (temperatures

Published as: J.M. Lowen, J. K. Leach, Functionally graded biomaterials for use as model systems and replacement tissues, *Adv. Funct. Mater.* 2020, 30 1909089.

up to 2000 K with a gradient of 1000 K).^[1, 2] Thereafter, the benefits of non-homogeneous materials have been exploited to design materials with specific structural, chemical, and morphological characteristics to influence mechanical properties and cell signaling.

Mechanical and biochemical gradients are found throughout the body and provide structural integrity at transitional interfaces of tissues (**Figure 2.1**). Bone is one example of a natural gradient in both radial and longitudinal directions. In the radial direction, bone consists of a dense outer structure (cortical bone) that changes to a softer and more porous internal material (cancellous bone).^[3, 4] Longitudinally, bone is composed of collagen fibers aligned to bear the necessary compressive and torsional forces to enable locomotion, resist mechanical stresses, and provide protection for internal organs. By varying its structural properties, bone can withstand external loading while enabling the transportation of nutrients and waste. Tendon-to-bone integration exhibits spatial variations in mineral concentration and collagen fiber orientation that enables efficient force transmission while minimizing stress.^[5, 6] Articular cartilage is yet another highly graded tissue interface where collagen fibers are aligned parallel to the articular surface and are increasingly perpendicular as they approach subchondral bone.^[7] Gradients are evident in cell signaling as well, with cells migrating in response to gradients of soluble chemoattractants, surface-attached molecules, and stiffness.^[8] Thus, gradients in stimuli, whether derived from composition, mechanical forces, or soluble cues, have an important effect on tissue development, regeneration, and homeostasis.

The design of FGMs have the potential to recreate the biological function of these heterogeneous tissues and increase our understanding of how to integrate biomaterials *in vivo*. The variety of techniques employed to form FGMs often utilize homopolymers,

copolymers, or composite materials to create FGMs with a wide range of properties. This review will describe recent advances in the field of FGMs and how they are applicable for new models of tissue development, repair, and for replacement tissues.

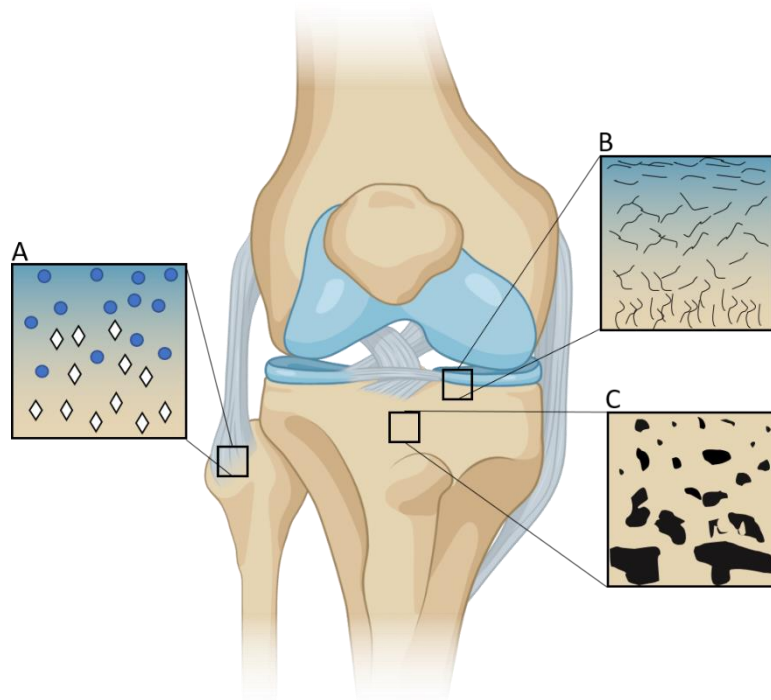


Figure 2.1 Native functional gradients enable tissues to withstand compressive and torsional forces and facilitate nutrient transport. (A) Mineralization gradient as ligament inserts into bone at the enthesis. Blue circles depict fibroblasts while white rhombuses depict hydroxyapatite. **(B)** Gradient of collagen fiber alignment in articular cartilage illustrates parallel collagen fibers in the superficial zone that become perpendicularly aligned toward the subchondral bone. **(C)** Porosity gradient from cortical to trabecular bone facilitates a transition from high strength and toughness that provides protection from the external environment to a more porous network that is home to stem and progenitor cells and increased cell exchange and nutrient transport.

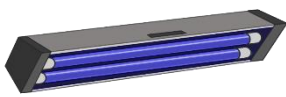
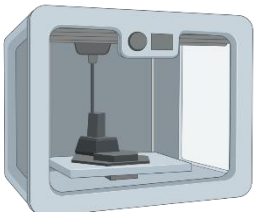
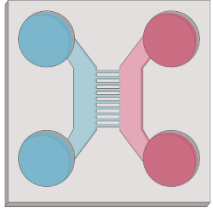
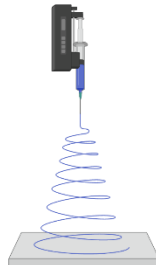
2.2 Methods for the fabrication of functionally graded materials

Gradients of composition, porosity, stiffness, and biochemical concentration are among the most frequently studied due to their known effects on cell behavior. Gradients may be continuous or discrete and extend in a linear or non-linear fashion. Scaffolds for softer tissues will often use more compliant biomaterials such as hydrogels, while harder tissue substitutes make increased use of stiff, slowly resorbing polymers and ceramics due to their ability to withstand higher mechanical load. With the increased use of FGMs in tissue engineering, several methods have been developed for incorporating gradients into biomaterials including light-based methods, 3D printing, microfluidics, electrospinning, freeze-drying, and solvent casting/particulate leaching (**Table 2.1**). The following section will discuss the fabrication of FGMs using these common methods.

2.2.1 Light-based methods

Light-based methods for the synthesis of materials and gradients rely on the incorporation of a photosensitive component, whereupon exposure to a designated wavelength initiates a chemical reaction that results in the formation or disintegration of crosslinking bonds. Hydrogels, highly tailorable polymeric networks capable of absorbing high amounts of water (70-99%),^[9] are widely used as photoresponsive substrates.^[10, 11] Hydrogels are appealing due to their capacity to mimic the fibrous and viscoelastic characteristics of the native extracellular matrix (ECM), as well as their hydrated nature and biocompatibility. Hydrogels are derived from natural proteins or polysaccharides such as collagen, fibrin, or alginate, or synthetic polymers such as polyethylene glycol (PEG), polyacrylamide (PA), and polyvinyl alcohol (PVA) to name a few. These polymers can be

Table 2.1 Methods for generating gradients in biomaterials

Method	Advantages	Disadvantages
Light-based 	<ul style="list-style-type: none"> • High resolution • Rapid manufacturing • Inexpensive 	<ul style="list-style-type: none"> • Cytotoxicity • DNA damage
3D printing 	<ul style="list-style-type: none"> • Rapid prototyping • Freedom of design 	<ul style="list-style-type: none"> • Limited to “printable” material • Post-processing
Microfluidics 	<ul style="list-style-type: none"> • Single cell handling • Reduced reagent consumption • Inexpensive 	<ul style="list-style-type: none"> • Non-standard cell culture • Small volumes
Electrospinning 	<ul style="list-style-type: none"> • Scalable • Inexpensive • Versatile 	<ul style="list-style-type: none"> • Toxicity (solvents) • Extensive optimization required • Acellular

functionalized to respond to light, chemicals, pH, ionic concentration, temperature, and magnetic and electrical fields.^[12] Furthermore, these materials may be engineered to be hydrolysable or degradable over time and have tunable biophysical properties through manipulation of crosslinker concentration, applied wavelength, and duration of irradiation.

Photolithography is useful for creating gradients by regulating the light that reaches a photolabile material. A photomask controls the distribution of light based on regions of translucency, providing the opportunity to dictate crosslinking down the axis (**Figure 2.2A**).^[13] PA gels were formed with opposing gradients of stiffness and protein concentration using photolithography.^[14] Gradient photomasks were designed with translucent regions to allow light penetration and opaque regions to attenuate light transmission. Polymerization was initiated by Irgacure 2959 and exposure to 254 nm UV light. Gel crosslinking correlated with the design of the photomask and resulted in soft and stiff regions ranging from 46.7 kPa to 126.7 kPa. When fibroblasts were seeded on gradient gels, cells preferentially migrated towards the stiffer end of the gel. Immobilized collagen gradients were then created by conjugating type 1 collagen to the PA gels using N-hydroxyl succinimide (NHS) and sulfo-succinimidyl-diazirine (SDA) chemistry. The collagen was exposed to 365 nm UV light, which superimposed an opposing collagen gradient on top of the rigidity gradient. When combining opposing mechanical and biochemical gradients, fibroblast migration was reversed toward the softer elastic modulus and higher collagen concentration. Human mesenchymal stromal cells (MSCs) followed a similar trend of migrating up a stiffness gradient when seeded on collagen-coated PA gels.^[15] Adipose derived stromal cells (ASCs) were entrapped within a gelatin methacryloyl (GelMA) hydrogel with a continuous stiffness gradient.^[16] ASCs seeded in

low stiffness regions (~8 kPa) exhibited increased cellular and nuclear volume and enhanced mechanosensitive protein localization in the nucleus, while the reverse was seen high stiffness regions (~30 kPa). Conversely, when ASCs were seeded on top of a gradient PA hydrogel, ASCs exhibited more cell spreading and nuclear localization of Lamin A and YAP at higher stiffnesses (**Figure 2.2C**).^[17]

As an alternative to photomasks that are fixed to control light transmission, the mask can be pulled across the biomaterial to create a spatiotemporal gradient of UV exposure time (**Figure 2.2A**).^[18] Methacrylated hyaluronic acid (HA) hydrogels with stiffness ranging from 3 to 100 kPa were produced and seeded with human MSCs.^[19] Cells exhibited increased spreading and proliferation on the stiffer regions compared to MSCs on softer portions of the gels. Stiffness gradients were produced in PA gels from 1-240 kPa using a similar technique.^[20] Beyond manipulating hydrogel mechanical properties alone, polymers such as polyethylene glycol monoacrylate (PEGMA) have been used to create hydrogels with accelerated degradation that correspond to increased UV exposure time.^[21] Surface charge has also been controlled with photomask-generated gradients. Sulfhydryl-to-sulfonate surface gradients were created by sliding a mask over a surface functionalized with 3-mercaptopropyltrimethoxysilane (MTS), which oxidized an increasing amount of thiol groups with longer exposure time.^[22, 23] Solutions of platelet free plasma (PFP), fibrinogen, and albumin were then washed over the surface to observe the combined effect of surface charge and the nature of the adsorbed protein on platelet adhesion. Surface charge gradients adsorbed with PFP promoted adhesion that was inversely related to the negative surface charge density, gradients with fibrinogen showed

maximum adhesion in the center, and gradients with albumin resulted in low overall adhesion.

As an alternative to traditional photomasks, maskless photolithography is achievable with projection photolithography. A UV light source illuminates a digital micromirror device that uses an array of fluctuating mirrors to regulate the output intensity of light of the desired image to be projected.^[24] Compared to mask-based photolithography, this method only requires an 8-bit image grayscale image and is not limited to the resolution or movement of a photomask. This system can be used with both photocrosslinkable and photodegradable hydrogels to create stiffness gradients with submicron resolution or pattern distinct regions of hydrogels for functionalization.^[24, 25]

Photon irradiation has been increasingly employed to generate light-based gradients since the discovery of two-photon irradiation in 1990.^[26] Two-photon photolithography uses a highly focused laser beam that raster scans material and may be used to efficiently cleave coumarin-derived photocages.^[27] 6-bromo-7-hydroxy coumarin (Bhc) is a common photocaging molecule used to protect amines and thiols. Upon activation, Bhc can immobilize gradients of molecules such as maleimide-functionalized growth factors (*e.g.*, vascular endothelial growth factor, VEGF).^[27, 28] As a model of angiogenesis, endothelial cells migrated into gels with VEGF gradients, but no migration was observed with gels lacking immobilized VEGF or without a gradient (*i.e.*, homogeneously immobilized VEGF).^[27]

Photolabile crosslinkers are often used when mixing two distinct hydrogel precursor solutions to create a continuous gradient between two solutions. These solutions may be mixed at different rates using a syringe or peristaltic pump, pumped into

a glass mold, and the resultant graded solution is crosslinked by exposure to light.^[29, 30] Flow rates vary from 0-50 mL/h with flow rates on the lower end (~100 μ L/min) used to prevent mixing of the gradient before crosslinking. Constructs typically range from 50-500 mm³ but can vary widely depending on application.^[31, 32] Gradients of stiffness within a copolymer hydrogel have been created by loading polymers of different molecular weight into each syringe, while hydrogels presenting gradients in peptide presentation (*i.e.*, HAVDI, which mimics N-cadherin) were created in a similar fashion.^[33, 34] Methacrylated alginate hydrogels possessing gradients of stiffness and adhesive peptide (RGD, Arg-Gly-Asp) concentration were seeded with MSCs to test the role of multiple interactions on cell differentiation and proliferation.^[32] More MSCs were observed in regions of lower stiffness and higher RGD concentration. Gradients of short interfering RNA (siRNA) have also been formed to spatially control gene expression, showcasing the versatility of biological processes applicable to this platform.^[31] In particular, human embryonic kidney (HEK293) cells transfected with destabilized green fluorescent protein (deGFP) displayed a gradient of fluorescence intensity upon spatial presentation of deGFP siRNA.

While homopolymers may be mixed at different rates, interpenetrating network (IPN) hydrogels can be formed by mixing two monomers that polymerize independently when exposed to different light sources. Acrylate and epoxy monomers were mixed with radical and cationic photoinitiators to create functionally graded IPNs by spatial exposure to different wavelengths of light.^[35] Scaffolds with porosity gradients have also been created by combining organic (polyethylene glycol diacrylate, PEGDA) and inorganic (methacrylated star polydimethylsiloxane, PDMS_{star}-MA) macromers and suspending

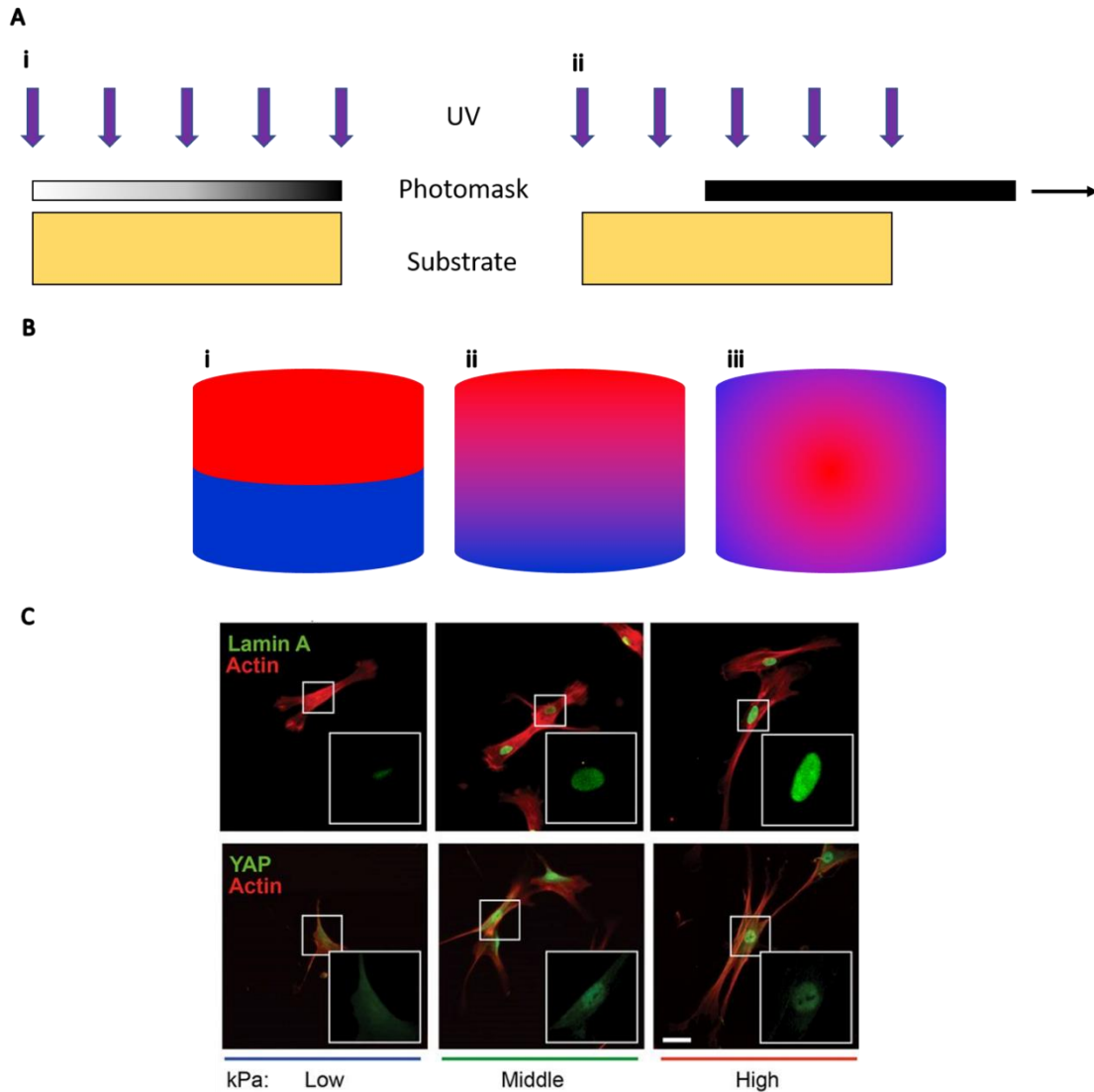


Figure 2.2 (A) UV generation of continuous gradients with photomasks. (i) UV light penetrates a photomask with a gradient in translucency to create a linear gradient on the substrate below. **(ii)** A photomask is pulled across a substrate to create a spatiotemporal gradient of UV exposure time. **(B) Cross-sectional view of gradient patterns. (i)** Discrete linear gradient which is often a result of combining individually fabricated materials. **(ii)** Continuous linear gradient used to interrogate the relationship of continuous stiffness changes on cell adhesion or differentiation. **(iii)** Radial gradient. An example of a non-linear gradient such as oxygen tension within and surrounding a cell spheroid. **(C)**

ASCs exhibit more spreading and nuclear localization of Lamin A and YAP as substrate stiffness increases from low (2 kPa) to high (40 kPa); scale bar = 50 μm . Panel C reprinted from Reference 17 with permission from the National Academy of Sciences.

them in aqueous or organic solvents after crosslinking.^[36] These gradient scaffolds exhibited swelling values from 5.5 to 12, stiffnesses of 40 to 405 kPa, and the ability to spatially control PDMS_{star-MA} distribution, pore size, and bioactivity, which could be utilized for rapid screening of cell-material interactions.

Photocrosslinking may be used to fuse independent hydrogel solutions and form a discrete gradient by stacking crosslinked layers (**Figure 2.2B**). A prehydrogel solution of PEGDA or GelMA was deposited inside a PDMS well and crosslinked by exposure to UV light. The next layer was deposited on top and crosslinked in the same manner. Each layer can be composed of different concentrations of biomolecules or hydrogels to effectively create a gradient across the finished construct.^[37] Fibroblasts migrated and exhibited distinct morphologies on these materials possessing a stiffness gradient, with cells on more compliant areas remaining round while cells on stiffer regions becoming more spindle-like.^[37]

Light-based gradient fabrication utilizes methods with high resolution and facilitates high throughput formation. The light-responsive photoinitiator functions through the generation of free radicals that crosslink macromers, yet this approach may impair cell or DNA damage due to UV light.^[38] Common photoinitiators include Irgacure 2959 and Irgacure 1173. Irgacure 2959 is most common due to its high free radical generation

efficiency and higher water solubility.^[39] Careful modulation of UV and photoinitiator exposure must be maintained to prevent cell damage.

2.2.2 3D Printing

3D printing is an exciting approach to create complex structures with more biocompatible, and even cell-loaded, materials that were previously required to be formed by micromachining or with sacrificial polymers. 3D printing can generate FGMs by precisely depositing materials based on predesigned models.^[40] There are multiple types of bioprinters including inkjet printers which use air pressure or mechanical pulses to eject droplets of polymer or bioink and microextrusion printers which employ pneumatic, piston, and screw-based mechanisms to produce flow of bioink.^[41] Continuous Liquid Interface Production (CLIP) printers utilize carefully controlled oxygen inhibition and UV curable resin to rapidly extrude constructs from a resin vessel^[42], while freeform reversible embedding of suspended hydrogels (FRESH) printers use a thermoreversible support bath to print hydrogels in complex, 3D structures.^[43] Bioprinters can be used with a variety of materials including hydrogels, synthetic polymers that can be readily extruded, and ceramics (**Table 2.2**).

Poly(ϵ -caprolactone) (PCL) is a synthetic polymer commonly used for printing due to its biocompatibility, processability, and ease in forming gradients.^[44] For example, PCL fibers were photochemically decorated with propargyl benzophenone using a gradient photomask and an azide-modified IKVAV peptide to guide neuronal cell growth.^[45] Unlike PCL fibers lacking a gradient, neuronal cells exhibited increased alignment and migration up the peptide gradient of IKVAV-gradient PCL fibers. Polylactic acid (PLA) and poly(ethyleneoxide terephthalate)/ poly(butylene terephthalate) (PEOT/PBT) copolymers

are also popular due to their physico-chemical properties, safety profile, and regulatory approval for orthopedic applications.^[46] These polymers were sequentially deposited to create surface energy and stiffness gradients for osteochondral regeneration.^[46] As surface energy increased, more proteins were adsorbed, forming more anchor points for cells and instructing their final shape and degree of spreading. PCL scaffolds were printed in the shape of sheep menisci and loaded with connective tissue growth factor (CTGF) and transforming growth factor- β 3 (TGF β 3) to induce recruitment and fibrochondrocytic differentiation of endogenous cells.^[47] Compared to non-loaded scaffolds, the treatment group resulted in superior meniscus regeneration with zonal properties. PCL has also been used in combination with collagen for interfacial tissue engineering to resemble the transition between tissues.^[48] PCL fibers were printed to form scaffolds with a pore size of 200 μ m, followed by controlled immersion of the scaffolds in a 1,6 hexanediamine/isopropanol solution in order to create an amine (NH₂)-density gradient along the length of the substrate. The scaffolds were subsequently covered with collagen *via* carbodiimide chemistry, which promoted adhesion of cells on the scaffolds and induced increases in metabolic activity up the collagen gradient. Collagen is a common choice for cartilage tissue engineering due to its prevalence in native cartilage, as well as its high biocompatibility and ability to support cell adhesion. Collagen was printed at different concentrations to alter the compressive modulus from <1 kPa to 30 kPa without affecting cell viability.^[49] In an effort to replicate the zonal distribution of cartilage that is present *in vivo*, collagen type II was sequentially printed with increasing chondrocyte density.^[50] Alginate is another common hydrogel used in biofabrication due to its biocompatibility, low cost, and gelation under mild conditions.^[51] Gradients in pore size within alginate were

Table 2.2. Applications of functionally graded materials.

Application	Composition	Gradient Type	Reference
Angiogenesis	<ul style="list-style-type: none"> • 6-bromo-7-hydroxy coumarin • VEGF 	<ul style="list-style-type: none"> • Biochemical 	[27]
Cartilage	<ul style="list-style-type: none"> • Poly(ϵ-caprolactone) • Chondroitin sulfate • Bioactive glass 	<ul style="list-style-type: none"> • Mineralization • Adhesive 	[48]
Cartilage	<ul style="list-style-type: none"> • Poly(ϵ-caprolactone) • Chitosan • Collagen 	<ul style="list-style-type: none"> • Porosity • Biochemical 	[49]
Dural	<ul style="list-style-type: none"> • Poly(ϵ-caprolactone) • Collagen • Polylactic acid 	<ul style="list-style-type: none"> • Stiffness • Biochemical 	[50]
Neural growth	<ul style="list-style-type: none"> • Poly(ϵ-caprolactone) • IKVAV peptide 	<ul style="list-style-type: none"> • Biochemical 	[45]
Osteochondral	<ul style="list-style-type: none"> • Hydroxyapatite • Poly(ϵ-caprolactone) 	<ul style="list-style-type: none"> • Mineralization • Porosity 	[51]
Osteochondral	<ul style="list-style-type: none"> • Alginate • Methylcellulose 	<ul style="list-style-type: none"> • Porosity 	[52]
Osteochondral	<ul style="list-style-type: none"> • β-tricalcium phosphate • TGF-β1 • Poly(N-acryloyl glycinamide) 	<ul style="list-style-type: none"> • Stiffness • Biochemical 	[53]
Osteochondral	<ul style="list-style-type: none"> • Silk fibroin • Silk-CaP 	<ul style="list-style-type: none"> • Mineralization 	[54]
Tendon-to-bone	<ul style="list-style-type: none"> • Poly(lactic co-glycolic acid) • Simulated body fluid 	<ul style="list-style-type: none"> • Stiffness • Mineralization 	[55,56]
Tendon-to-bone	<ul style="list-style-type: none"> • Collagen • Glycosaminoglycans 	<ul style="list-style-type: none"> • Alignment • Biochemical 	[57]

formed for spatiotemporal gene delivery by modulating the ratio of methylcellulose to alginate and washing the methylcellulose out post-fabrication.^[52] By controlling porosity, the investigators achieved both rapid and transient transfection of osteogenic and chondrogenic genes to induce complex tissue formation such as the bone-soft tissue interface. Porosity gradients were also created in an IPN of alginate and gelatin with pore

sizes ranging from 80-2125 μm , demonstrating the potential of 3D printing in developing bio-based scaffolds with controlled pore size.^[53]

Ceramics are commonly used to form engineered tissues such as bone, as these carbonated phosphates can withstand high temperatures, abrasion, and mechanical stresses.^[54] Functionally-graded ceramics are promising for use in the transition zone between the chondral and osseous phases at the bone-cartilage interface. Gradients of β -tricalcium phosphate (β -TCP) were printed with a potent, chondroinductive growth factor (transforming growth factor beta 1, TGF- β 1) in a poly(N-acryloyl glycinamide) (PNAGA) gel to promote osteogenic and chondrogenic differentiation of human MSCs.^[55] Hydroxyapatite (HAp) is another calcium phosphate (CaP)-based ceramic that has been 3D printed for use at the osteochondral interface. HAp was combined with PCL to fabricate constructs with gradients in composition and porosity.^[56] These scaffolds demonstrated an inverse relationship between porosity and compressive modulus that was independent of ceramic concentration. By inclusion of the ceramic phase, these scaffolds had an average compressive modulus between 86 – 220 MPa, which is within the physiological range of trabecular bone. GelMA is a photo-crosslinking bioink that can be combined with ceramics to create gradient constructs. A GelMA/HAp tri-layered scaffold was fabricated with increasing concentrations of GelMA and HAp in each layer and implanted in a rabbit osteochondral defect.^[57] Compared to a monophasic scaffold, the tri-layered scaffold resulted in faster cartilage regeneration. Bioactive glass (BG) is a ceramic that releases ions which promote cell adhesion, proliferation, and differentiation.^[58] A gradient scaffold consisting of a top layer of poly(N-acryloyl 2-glycine) (PACG)-GelMA-Mn²⁺ and bottom layer of PACG-GelMA-BG was 3D printed for

osteocondral repair.^[59] After implantation in a rat osteochondral defect, subchondral bone formation in the gradient scaffold was significantly greater compared to scaffolds without Mn²⁺ and BG. These findings demonstrate the promise of producing gradient materials that may have utility in modeling or replacing damaged interfacial connective tissues.

Inkjet printing can create functionally graded ceramic structures in a more continuous fashion compared to additive manufacturing. Complex 3D geometries of alumina and zirconia powder-based inks were inkjet printed in an effort to provide better control over material combinations.^[60] This experiment illustrated the potential to create a smooth transition between multiple ceramics with high accuracy with regard to drop positioning. Inkjet printing can also be used to create gradients of growth factors on substrates.^[61] Gradients of basic fibroblast growth factor (FGF-2) and bone morphogenetic protein-2 (BMP-2) were printed on coverslips to test the capacity of growth factor combinations to promote osteogenic differentiation of the murine multipotent C2C12 cell line.^[62] FGF-2 had an inhibitory effect on osteogenic differentiation, while ALP expression was highest in BMP-2 only conditions that increased up the concentration gradient. Growth factor gradients have also been generated by creating a gradient of heparin-binding domains to attract heparin-binding growth factors (HBGFs) such as FGF-2. Gradients in heparin-binding domains were created in hyaluronate-based hydrogels with heparin sulfate proteoglycan-derived perlecan/HSPG2 domain I (**Figure 2.3B**).^[63] MC3T3 pre-osteoblasts and MDA-MB-231 breast cancer cells migrated up a FGF-2 gradient formulated using 3D printing.

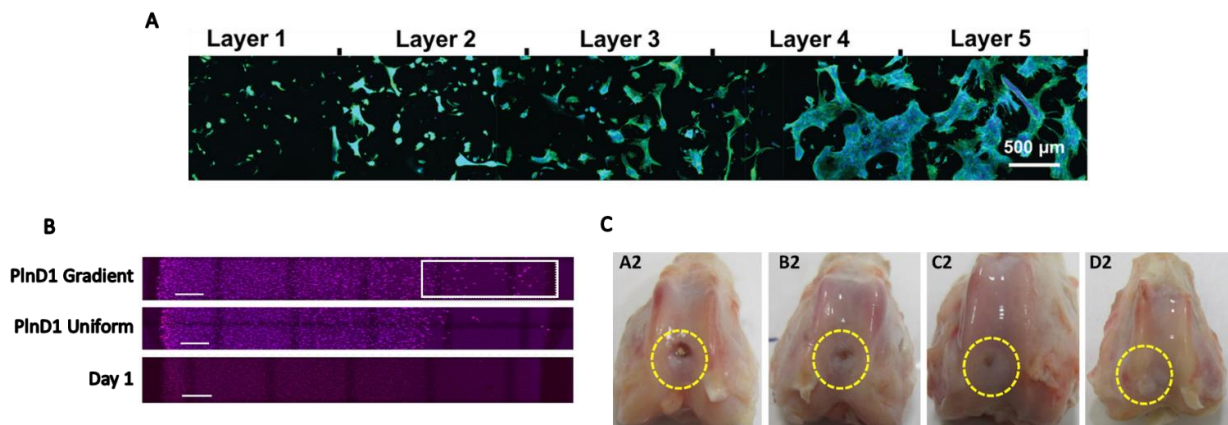


Figure 2.3 Cellular response to FGMs. (A) ASCs exhibit increased spreading and proliferation as stiffness of annealed microgels increases from Layer 1 to Layer 5. Image reproduced from Reference 73 with permission from John Wiley and Sons. (B) MDA-MB-231 breast cancer cells exhibit increased migration by day 7 towards the region of interest (white box) on a perlecan domain I gradient compared to uniform perlecan distribution and a day 1 control, scale bar = 1mm. Reprinted from Reference 61 with permission from Elsevier. (C) Biphasic HAp and CS scaffolds (D2) outperformed monophasic CS (C2), HA (B2), and sham (A2) groups in a rabbit osteochondral defect model. Reprinted from Reference 149 with permission from Elsevier.

Bioprinting facilitates rapid, on-demand prototyping of constructs possessing complex architectural and chemical cues. Printing in three dimensions enables formation of increasingly complex gradients, with the ability to integrate multiple materials by employing multiple print heads. However, materials utilized in 3D printing must be viscous enough to maintain structure post-printing but be shear-thinning to enable extrusion from

the print head.^[64] Post-processing may also be necessary to remove support material or facilitate crosslinking.

2.2.3 Microfluidics

Microfluidic platforms capitalize on their precise control of fluid flow to generate gradients of bioactive factors and shear stress, which provide the opportunity to study model systems *in vitro* on a miniaturized scale. Such platforms can be combined with other technologies such as 3D printing and electrospinning to produce highly tailored gradient scaffolds. Their small scale facilitates high-throughput analysis at the single cell level, significantly reduces reagent cost, and provides highly responsive dynamic gradients by modulating flow rates.^[65] A large portion of microfluidic devices are fabricated through soft lithography techniques and utilize polydimethylsiloxane (PDMS) as their substrate.^[66]

Microfluidic systems are under development to model biochemical gradients that are observed *in vivo* and study their effect on cell behavior. Microfluidic gradients can be generated using tree-shape devices, Y-shape devices, membrane-based devices, pressure balance, droplet generation, and others.^[65] Embryonic stem cells (ESCs) were exposed to orthogonal gradients of morphogens to promote localized differentiation of motor neurons in the neural tube, while a rotating gradient was applied to highly metastatic fibrosarcoma HT1080 cells to influence migration.^[67] Microfluidic devices facilitate the application of non-linear concentration gradients that are involved in cell migration, differentiation, and growth.^[68] Asymmetrical grids of channels promoted nonlinear diffusion that creates exponential and sigmoidal gradients.^[68] The applicability

of this design was demonstrated by assessing fibroblast cell viability in response to non-linear hydrogen peroxide (H_2O_2) concentrations .

Bilayered microfluidic devices have been used to guide the differentiation of stem and progenitor cells *in vitro*. Within a bilayered microfluidic device, MSCs were suspended in agarose in the bottom compartment, which was separated by a microporous membrane from the top layer that contained 3 media channels for growth, osteogenic, and chondrogenic media.^[69] This design exposed the cells to a gradient of soluble cues due to the mixing of the three media channels after diffusion through the membrane. Osteogenesis was achieved in cells exposed primarily to osteogenic media, while those cells stimulated by chondrogenic media primarily underwent chondrogenesis. Cells exposed to the middle of the device exhibited a gradient of differentiation between the two lineages. A similar bilayered device was created with the addition of decellularized omentum ECM to the bottom of the device to serve as a scaffold.^[70] The addition of natural ECM further recapitulates the complexity of the natural 3D microenvironment, providing an opportunity to use microfluidics to better model native tissues.

Biochemical gradients can be combined with mechanical gradients to interrogate the additive and synergistic effects of stimuli on cell behavior and function. Fibroblasts seeded on nanofibers of different spacings in a microfluidic device were sensitive to platelet-derived growth factor (PDGF-BB) dose.^[71] Fibroblasts underwent maximal chemotaxis at lower PDGF doses and closer nanofiber spacing, which enabled cells to spread over two fibers and have punctate sites of adhesion. Gradients of substrate stiffness may also be formed within microfluidic devices to explore the synergistic influence of chemical concentration and ECM compliance on cell function. Orthogonal

chemical and rigidity gradients were obtained by mixing PA solutions with different chemical concentrations in a microfluidic device. The solutions were blended at a Y-junction and subsequently irradiated while sliding a photomask over the device.^[72] The liquid pressure of cell-laden hydrogels resulted in convex PDMS deformations in the center of a microfluidic device, and UV patterning was applied to create a height gradient under the PDMS.^[73] When excess fluid was removed, the PDMS membrane flattened, applying increasing force towards the center of the device and generating a compressive force gradient. Porosity gradients are yet another form of stimuli attainable with microfluidics. The pore size in alginate nanogels was regulated by altering flow rates in the channel containing the monomer and the channel containing the CaCl₂ crosslinker.^[74] Nanogel diameter varied from 68-138 nm and pore size ranged from 11-24 nm. This technology could be utilized to tailor release rates of polypeptides or other compounds from the hydrogel. PEG microgels were fabricated and annealed to form a gradient in stiffness. Human MSCs seeded on the microgel scaffold exhibited increased proliferation and spreading up the stiffness gradient (**Figure 2.3A**).^[75]

Gradients created within microfluidic devices are useful to mimic native physiology on a small scale. For example, an oxygen gradient ranging from 2% to 21% was created to investigate the influence of oxygen tension on gene expression and metabolism on human ESC-derived hepatocytes.^[76] One side of a microfluidic device was exposed to a channel of a continuously flowing 95% N₂/5% CO₂ gas mixture to generate the oxygen gradient. Oxygen gradients were also created by infusing sodium sulfite, an oxygen scavenger, through a microfluidic device.^[77] When the device was loaded with endothelial cells and fibroblasts, biased vessel growth toward the scavenger channel was observed

in both chronic and intermittent hypoxia conditions. Thus, precise spatiotemporal gradients of oxygen are created by leveraging the minimal diffusion distance oxygen must travel in microfluidic devices and regulating fluid flow through the microdevices.

Microfluidic gradients are valuable to test the effect of chemical concentrations on cells in a high-throughput manner. Microfluidic chambers were created by overlapping PDMS layers to form grid-like channels used to test antimicrobial susceptibility.^[78] *E. coli* was seeded in the device and exposed to a unique concentration of ampicillin and gentamicin at each intersection, thereby enabling efficient testing of antibiotic doses with minimal reagents. The bacterial burden was minimized at intersections containing high doses of both antibiotics, demonstrating the synergistic effect of the drugs. In another example, microfluidic systems were used to study the efficacy of a colorectal cancer treatment, demonstrating increasing cell death up the concentration gradient.^[79] This is a valuable tool for determining both effective dose and diffusive properties of drugs. Alternatively, microfluidic devices can model gradients of cytotoxic chemicals and their dose-dependent effect on cells. Microfluidic devices were used to mimic environmental pollution by applying a gradient of benzopyrene to bronchial epithelial cells in a model of lung pathophysiology.^[80] The benzopyrene directionally induced cell shrinkage, cytoskeleton disintegration, reactive oxygen species (ROS), and inflammatory cytokines in the bronchial epithelium.

Cell migration, a process dependent on adhesivity, cell density, and chemotactic signals, can be studied utilizing gradients created in microfluidic devices. A gradient of laminin oligopeptide concentration was generated in an H-shaped microfluidic network between channels containing peptide-grafted collagen or untreated collagen.^[81] The

migration of chick dorsal root ganglion neurons was observed between the channels and in response to laminin peptides. Similarly, growth factor gradients were created in a 3D microfluidic device to interrogate osteoblast chemotaxis in bone regeneration.^[82] A microfluidic chip was developed for studying the responsiveness of lung cancer cells to phototaxis, the migration of cells or organisms toward or away from light.^[83] A light-gradient chip was laser inscribed and placed on top of a cell-culture chip with blue light illuminating the top. Lung cancer cells migrated to the darker side of the chip due potentially to the production of intracellular ROS proportional to the intensity of blue light.

Microfluidic chips can be combined with other technology to produce complex gradient scaffolds. A microfluidic device was designed with a valve-based flow-focusing junction (vFF), in which the size of the orifice was adjusted in real time by thin pressurized PDMS walls.^[84] This device was then connected to an extrusion printer to manufacture 3D scaffolds with varying porosity achieved by adjusting the valve diameter of the microfluidic device. In another example, a Y-junction microfluidic device was combined with electrospinning to produce nanofibers with a gradient of nanoparticles and biomolecules.^[85] Microfluidic platforms provide a technique to create highly reproducible gradients with small reagent volumes. These devices are useful to study single cell responses to functional gradients or to create precise gradients on a larger scale when combined with other technologies. However, microfluidics introduce non-standard cell culture techniques that require familiarization and limit experiments to relatively small volumes compared to conventional cell culture. Therefore, microfluidics represent an excellent platform to investigate specific cell-cell or cell-environment interactions but may not be appropriate for large scale studies.

2.2.4 Electrospinning

Electrospinning exploits the electrostatic repulsion between surface charges to continuously draw nanofibers from a viscoelastic fluid.^[86] Importantly, the fibers produced with polymers, ceramics, and small molecules possess dimensions on the nanometer scale, similar to the native ECM.^[87] The resulting fibers can be functionalized and aligned, making electrospinning an appealing choice for producing FGMs.^[88]

Electrospinning can create a substrate with gradients in various morphological and mechanical properties simply by dispersing one layer, changing the syringe to one containing a different material, and then depositing the next layer on top. Bilayer scaffolds were created by consecutively spinning polyhydroxybutyrate-co-hydroxyvalerate (PHBV) to generate nanofibers, followed by PLA or PCL to produce microfibers.^[89] The scaffold was inverted and another layer of microfibers was deposited, resulting in a trilayered scaffold with a nanofibrous middle structure. The PHBV nanofibers acted as a barrier membrane permeable to nutrients but blocking cell migration, while the microfibers supported cell proliferation. A PLA-PCL-collagen trilayered scaffold was synthesized in a similar fashion for use as a dural substitute.^[90] The inner layer of PLA was incorporated to prevent tissue adhesion, the midlayer with PCL to provide a watertight seal, and the outer layer of collagen to promote cell attachment and proliferation. This gradient polymeric substrate exhibited significantly less water absorption compared to a collagen matrix control. When implanted in a rabbit dural defect model, the trilayer substrate exhibited greater cell proliferation and similar biocompatibility as the autologous fascial tissue control.

Electrospun scaffolds have been utilized as drug delivery vehicles to promote recruitment of endogenous cells *via* chemoattractant gradients. A tri-component scaffold consisting of rapidly degrading poly(ethylene oxide) (PEO) with collagenase, slower-degrading hyaluronic acid (HA) with platelet-derived growth factor-AB (PDGF-AB), and PCL was designed to enable direct cell migration for connective tissue repair.^[91] Upon implantation into rat meniscus defects, tri-component scaffolds achieved significantly higher cellularity compared to scaffolds without collagenase or PDGF-AB. An electrospun PCL scaffold functionalized with hydroxyapatite *via* polydopamine particles (PCL-PDA-HA) was combined with substance P (SP) to promote endogenous stem cell mobilization toward bone defects.^[92] The combination of PCL-PDA-HA and SP enhanced *in situ* bone formation compared to control groups lacking either compound.

Electrospun fibers of varying composition can be collected independently and stacked to create scaffolds with gradients in composition. For example, agarose-gelatin based scaffolds were fabricated with mid-layers of functionalized PCL fibers.^[93] PCL fibers contained a dual gradient of chondroitin sulfate and bioactive glass to engineer GAG-enriched and mineralized cartilage. Gradients in both structure and material can be created by changing the material in the syringe and the distance between the syringe needle and collector. Composition and fiber alignment gradients were created by harvesting fibers of HAp and poly(lactic-co-glycolic) acid (PLGA) on a collector with reciprocating rotation within 30°.^[94] A fiber alignment gradient was also created by depositing fibers between two parallel aluminum disks. As the layer with aligned fibers became thicker, the electric field weakened, resulting in a more random alignment.^[95, 96] Furthermore, gradient scaffolds have been created by coating electrospun fibers after

fabrication. Scaffolds possessing a gradient in mineralization were formed by linearly exposing regions of a scaffold to simulated body fluid (SBF) for increasing durations.^[97] Mechanical testing of the scaffold revealed that the mechanical properties, namely the resulting gradient in stiffness, were adequate for tendon-to-bone models.^[97] When seeded with adipose stromal cells (ASCs), osteogenic markers were positively correlated with mineral content.^[98]

Bidirectional gradient electrospinning offers an alternative to simple stacking of materials to create gradient scaffolds. In this system, two solutions are simultaneously electrospun onto a collector at inversely proportional flow rates.^[99, 100] Syringe pumps can also be employed to mix together two solutions at inverse rates before being spun, resulting in the deposition of a single fiber that varies in composition over time.^[101] Electrospinning has also been combined with methods such as braiding and thermally induced phase separation (TIPS) to prepare scaffolds with widely varying properties. For example, a triple-layered vascular scaffold was created by first electrospinning an inner layer composed of thermoplastic polyurethane (PU), followed by braiding a layer of silk, and then freeze drying a layer of PU for a porous outer layer.^[102] The lumen diameter of the scaffold was 3.18 mm with an average thickness of 1.05 mm, and the burst pressure was ~23,000 mmHg, which is sufficient for vascular graft applications. Human umbilical vein endothelial cells formed a confluent layer on the inner surface of the scaffold with high cell viability. Therefore, electrospinning can produce FGMs in numerous ways and is highly compatible with other fabrication methods. It is inexpensive and scalable, enabling production of large quantities of scaffold with versatile gradients. However, the process is damaging to cells due to the use of cytotoxic solvents and possible shear-

forces upon extrusion. Furthermore, extensive optimization is required for consistent production.

2.2.5 Freeze-drying

Freeze-drying, in which materials are frozen and ice crystals subsequently removed by sublimation, can yield several kinds of gradient materials.^[103] Freeze-drying is an effective method to create a porous architecture in materials, in which the resulting pores are inverse images of the frozen solvent crystals.^[104] Freeze-drying offers the ability to tailor a material's physical properties based on the solvents and solutes used.^[104]

Iterative freeze-drying is an effective approach to bind multiple layers and create a gradient scaffold through interfacial adhesion, with scaffolds often used at the bone-cartilage or bone-tendon interface. For example, collagen-chitosan–polycaprolactone (CH–PCL) copolymer and chondroitin sulfate (CS) were mixed at various ratios to create a stratified scaffold for articular repair.^[105] After each layer was created, the scaffold was freeze-dried to generate both a porosity and composition gradient between layers. This technique has been used with multiple biomaterials for osteochondral defects including collagen,^[106-108] alginate-chitosan β -TCP,^[109] HAp/PVA,^[110] and glycosaminoglycan-porous titanium^[111]. Porosity gradients have been created in collagen *via* freeze-drying to test the effect of pore size on fibroblasts.^[112] By varying collagen concentration from 0.26% to 0.13% prior to freeze-drying, pores were created ranging from ~87 μm to ~166 μm , demonstrating the relationship between protein concentration and resultant pore size as a design tool for fabricating gradient scaffolds.

Freeze-casting is a related process wherein a material is frozen to induce anisotropic formation of ice crystals that are then sublimated to create a porosity gradient. This process is commonly applied to ceramics such as biomimetic titanium alloys for dental and orthopaedic implants.^[113] After freeze-casting, ceramics can be fired where they are exposed to high temperature and pressure, resulting in a material with a flexural strength in the hundreds of megapascals.^[114] The resulting structure is dense at one end to support loading and becomes increasingly porous to promote bone growth. For example, HAp particles were freeze-casted around a frozen copper rod, resulting in expulsion of the HA particles and assembly into a lamellar structure oriented parallel to the freezing direction.^[115] Due to the radial gradient of ice formation, the lamellar spacing becomes wider towards the outside and enables self-seeding of cells due to capillary action. Freeze-casting is amenable for combination with other techniques such as electrospinning^[116] or solvent-casting to generate FGMs. It is a low-cost method for generation of porosity gradients. However, it is not amenable for concurrent seeding of cells.

2.2.6 Solvent casting and particulate leaching

Solvent casting and particulate leaching is a coordinated process used primarily for forming macroporous scaffolds that include randomly oriented pores.^[117] This technique is also useful to form porosity or compositional gradients. Porogen particles (e.g., salt, sugar, gelatin, etc.) are dispersed in a solvent which is allowed to evaporate, and the composite material is then placed in a bath to leach out the porogen (**Figure 2.4A**).^[118] The simplest porosity gradient can be observed in bilayer scaffolds such as

those used for osteochondral defects. Macroporous PLGA scaffolds were formed *via* particulate leaching with pore sizes ranging from 50 to 450 μm .^[119] A mixture of PLGA and sodium chloride particulates was dissolved in dichloromethane and pressed into a mold, followed by porogen leaching in water. Multiple types of porogens can be used to create a gradient in pore size while preserving continuity between layers of a multilayered scaffold. A monolithic scaffold was created by first layering sucrose crystals and HA followed by mannitol crystals and PCL.^[120] The sucrose and mannitol were removed by rinsing with water, resulting in a monolithic graft with varying pore size and composition.

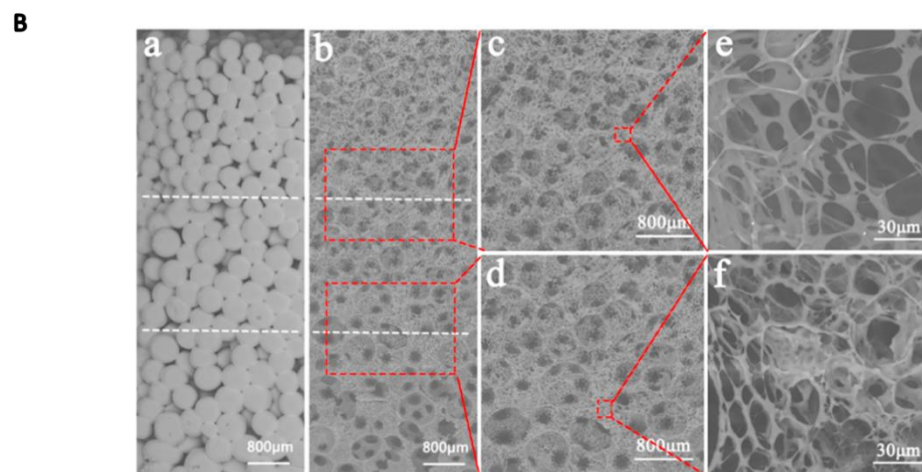
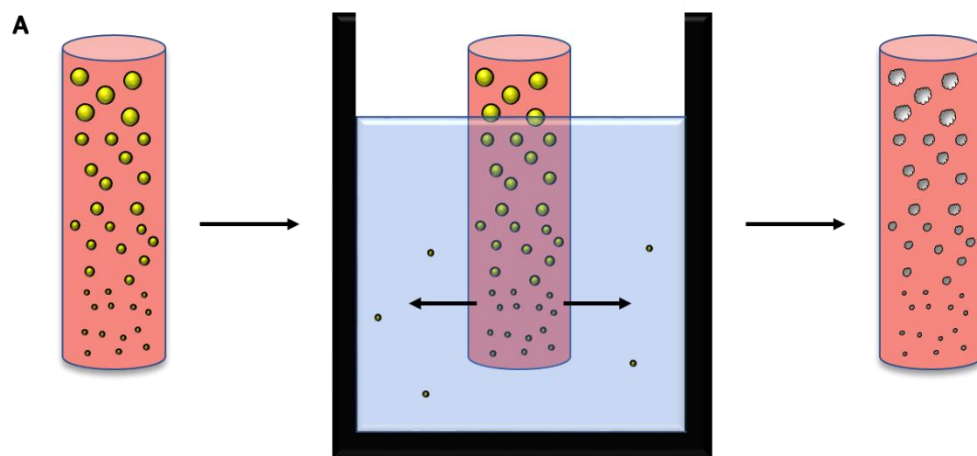


Figure 2.4 (A) Porogens such as salt or sugar can be distributed in a scaffold by size and subsequently leached out to create a porosity gradient. This construct can model the porosity gradient in bone. Porogen is denoted as yellow spheres, while resulting pores are white with imperfect boundaries. **(B)** Sugar particles leached out of a PLLA scaffold created a gradient in pore size from 300 to 600 μm . Sugar particle gradient can be seen in part a, with the resultant porosity after leaching in part b. Parts c-f are higher magnification. Reprinted from Reference 125 with permission from Elsevier.

Melt mixing and particulate leaching have been combined to make PCL,^[121] PLA,^[122] and PCL/PLA^[123] gradient scaffolds. PCL and PLA were mixed at known ratios with PEG and NaCl and compressed, and PEG and NaCl were removed by particulate leaching in water. The PLA layer had pores ranging from 90 to 110 μm , while the PCL layer had pores ranging from 5 μm to 40 μm based on the size of NaCl used as the porogen. Solvent leaching was combined with TIPS to create a graded composite membrane.^[124] PLGA solutions were mixed with non-stoichiometric nanosized HAp (nano-HAp) and lauric acid (LA) in DMSO. Tri-layer scaffolds were then created by layering solutions with a graded composition of nano-HAp and LA and freezing the scaffold before the application of each subsequent layer. The frozen scaffold was

submerged in water to remove the DMSO and create a composite graded scaffold. In another example, PLLA scaffolds possessing a porosity gradient were formed through TIPS by mixing sugar particles of decreasing diameter while applying heat. Scaffolds underwent phase separation overnight at -20°C with subsequent freeze-drying and particulate leaching.^[125] The resulting scaffolds had a gradient in pore size from 300 to

600 μm , demonstrating the promise of this method to create scaffolds useful for tissue engineering (**Figure 2.4B**). Solvent casting and particulate leaching is an inexpensive method to form complex pore size and density gradients. Compared to freeze-casting, gradient formation is more precisely controlled, however the use of additional reagents is required for pore formation.

2.3 Application of functionally graded materials in model systems and engineered tissues

Native graded tissues are anisotropic in multiple properties including stiffness, composition, structure, and chemical concentration. When developing model systems, it is necessary to consider these factors to accurately recreate the stimuli to which cells are exposed. In light of the failure of uniform substrates lacking the presence of gradients, it is essential to engineer graded materials for producing more accurate model systems. The following section describes recent examples of model systems based on FGMs.

2.3.1 Musculoskeletal and connective tissues

The musculoskeletal system is a key target for the development of FGMs due to the number of native heterogeneous tissue interfaces. Bone, articular cartilage, tendon-to-bone, tendon-to-muscle, and ligament-to-bone interfaces exhibit complex architectural and compositional organization. Furthermore, many of these tissues are susceptible to injury at the interface due to the biomechanical differences between hard and soft tissues.^[126] Therefore, the creation of FGMs to mimic these interfaces holds great potential for understanding and treating these injuries.

2.3.2 Enthesis models

The tendon- and ligament-to-bone interface (enthesis) is a common site of repair in patients of all ages with injuries such as tennis or golfer's elbow, jumper's knee, and Achilles insertional tendinopathies.^[127-129] Depending on the severity of the injury, current treatment methods range from rest and steroid injections to surgical interventions and tissue grafts.^[130] However, allogeneic grafts face several major shortcomings including host tissue reaction and risk of disease transmission, while autologous tissue grafting is limited by tissue availability and donor site morbidity.^[131, 132] Furthermore, grafts are associated with high injury recurrence rates due to formation of neofibrovascular tissue that compromises graft integrity.^[131, 133] The enthesis is divided into four distinct zones composed of varying cell types, matricellular proteins and proteoglycans, resulting in a tissue with a gradient in mechanical properties.^[134, 135] In light of the complexity of this tissue, there is a significant need to develop improved model systems to understand the biophysical requirements of the enthesis and realize the goal of generating replacement tissue for these injuries.

Multi-layered scaffolds have been created as FGMs to mimic the structural, mechanical, and topographical properties of the bone-soft tissue interface. Synthetic polymers are often used including PCL, a common polymer used for bone tissue engineering due to its slow degradation, and PLGA for its application in modeling soft tissues and its absorbable nature.^[136] Scaffolds for the bone-ligament interface possessing a gradient of physical and mechanical properties were fabricated by 3D printing a layer of PCL and then electrospinning PLGA on top. MSCs seeded on this

gradient scaffold exhibited increased alkaline phosphatase activity and glycosaminoglycan production compared to MSCs on the individual scaffold components.^[136] The instructive potential of fiber alignment within FGMs is under development to model and replace bone-patellar tendon-bone grafts, which are considered the gold standard for anterior cruciate ligament (ACL) ruptures.^[137] Tissue engineered enthesis models were formulated with randomly aligned PLGA fibers that transitioned to aligned PCL and then back to randomly aligned PLGA to mimic the structural properties of bone-patellar tendon-bone grafts. A random-to-aligned scaffold of PCL for hard-soft tissue interfaces was seeded with osteosarcoma cells in the random region and fibroblasts in the aligned region.^[138] Fibroblasts grew aligned along the fibers, while osteosarcoma cells maintained a random orientation. Both cell types migrated into the transition zone, providing a potential model for mimicking the transitional interface between bone and soft tissue. To complement the effect of gradients in fiber alignment, regions of PCL and PLGA scaffolds were soaked in SBF, resulting in a mineralized gradient that mimics the bone-ligament connection.^[98, 139] Hybrid scaffolds composed of ceramics and polymers such as β -TCP and poly(glycerol sebacate) (PGS) are also under investigation to model the bone-soft tissue interface.^[140] PGS served as a barrier membrane when seeded with fibroblasts to combat scar formation with inferior mechanical properties.

While some FGMs seek to model the entire enthesis structure using synthetic polymers, others aim to recreate the collagen gradient present at the enthesis. Four-layered scaffolds were formed with a tendon layer composed of collagen, an uncalcified fibrocartilage layer of collagen and chondroitin sulfate, a calcified cartilage layer of

collagen and low concentration apatite, and a bony layer composed of collagen and high concentration apatite.^[108] The scaffold supported the adhesion and proliferation of fibroblasts, chondrocytes, and osteoblasts toward each corresponding matrix. Salt leaching and freeze drying was used to create gradients in pore alignment from anisotropic to isotropic pore structure in order to mimic collagen alignment at the tendon/ligament-to-bone interface.^[141] MSCs exhibited gradients in gene expression of tendon/ligament and cartilaginous markers along the scaffold in the absence of soluble factors, confirming the instructive potential of the substrate on cell differentiation. Collagen-GAG scaffolds incorporated both structural and biochemical cues consisting of coincident gradients of mineralization and geometric anisotropy present in native bone-tendon junctions.^[142] The spatially graded contact and mineralization cues encouraged 3D alignment of tenocytes and selective pro-tenogenic and osteogenic MSC differentiation within a single scaffold. While these approaches expand our current understanding of enthesis function, the field currently lacks a standardized set of parameters for evaluation and use in the clinic. As a result, the results of mechanical and biochemical tests are challenging to compare across studies or to native tissue. Furthermore, there is a lack of large animal studies to propel these technologies along the developmental timeline.

2.3.3 Osteochondral models

The ECM of articular cartilage varies from predominantly collagen type II in the superficial zone to increasing amounts of collagen type X, proteoglycans, and sulfated glycosaminoglycans (sGAGs) in the deep zone with increasing mineralization.^[11, 126]

Collagen fiber alignment is similar to that found in the enthesis, where collagen alignment is parallel at the articular surface and becomes increasingly perpendicular towards the subchondral surface.^[143] Chondrocyte morphology also varies from thin and elliptical at the articular surface to more spherical chondrocytes oriented in stacks perpendicular to the articular surface.^[143] This graded structure provides a smooth, lubricated surface for articulation and facilitates the transmission of loads with low friction.^[144] In light of these gradients, FGMs are promising candidates to model the zonal structure found in articular cartilage.

The bone-cartilage interface is modeled with FGMs using similar approaches as used in models of the enthesis. Gradients in inductive cues (*i.e.*, growth factors) are under investigation to recapitulate osteochondral tissue. A chitosan-gelatin hydrogel/PLGA scaffold with dual-delivery of TGF- β 1 and BMP-2 was designed to promote the differentiation of MSCs to chondrocytes and osteoblasts.^[145] *In vitro* culture of MSCs confirmed that the hydrogel and PLGA phases promoted chondrogenic and osteogenic differentiation, respectively. This strategy also leverages the contributions of substrate stiffness to guide cell fate, with stiffer materials effectively inducing cells toward the osteogenic phenotype. When tested in rabbit osteochondral defects, the construct achieved successful integration of hyaline-like cartilage and mineralized tissue with native tissues at 2 months. Microfluidic platforms can be used to deliver gradients of osteogenic and chondrogenic inductive media to designated parts of a scaffold to create a similar gradient.^[146] Microfluidics were combined with a bioreactor system to deliver various inductive media to form osteochondral constructs for studying osteoarthritis.^[147] However,

this method is ultimately limited to smaller constructs and lacks the native complexities associated with the development of osteoarthritis *in vivo*.

Osteochondral tissues can be modeled by the presentation of mineral gradients. Improved osteochondral tissue regeneration was observed with a bilayer scaffold of chitosan and HA as the cartilage layer and chitosan-alginate and HAp as the bone layer.^[148] The cartilage region was defined by lower stiffness and the presence of HA, as found in native cartilage, while the bone layer was optimized for higher stiffness and osteoconductive HAp. Osteochondral tissue was modeled with an injectable, semi-interpenetrating network hydrogel construct containing chondroitin sulfate nanoparticles and nano-HAp in chondral and subchondral hydrogel zones, respectively.^[149] The composite scaffold demonstrated accelerated osteochondral tissue generation in a rabbit osteochondral defect compared to monophasic and untreated controls (**Figure 2.3C**). Bilayer scaffolds consisting of a silk fibroin layer and a silk-CaP layer were implanted in a rabbit critically-sized osteochondral defect.^[150] Developing tissues were positive for collagen type II and GAG within the silk layer, while *de novo* bone growth and capillary invasion were observed in the silk-CaP layer. Other ceramics such as β -TCP are effective to introduce mineralization to osteochondral scaffolds and increase mechanical strength.^[151]

Spatial gradients are also under examination to address damage to cartilage with healthy underlying bone. Anisotropic pore geometries were formed by unidirectional freeze-drying of alginate scaffolds that were further functionalized with collagen type I and II.^[152] This strategy resulted in improved scaffold mechanical properties and promoted greater sGAG and collagen deposition compared to an isotropic pore geometry when

seeded with human infrapatellar fat pad (IFP)-derived stromal cells. Freeze-drying was combined with centrifugation to create a porosity gradient in silk fibroin-chitosan-nano-HAp scaffolds.^[153] Scaffolds with porosities ranging from 82-91% supported proliferation of MSCs. These studies suggest the promise of using porosity gradients to match the progressive osteochondral porosity structure observed *in vivo*. As discussed previously, stiffness is another key parameter that can be manipulated in model gradient systems. For example, gradients in stiffness ranging from 5-60 kPa were achieved by varying the concentration of PEG from 2-20% (w/v).^[34] Both chondrocytes and MSCs encapsulated in these gels with gradients in stiffness exhibited zonal specific responses and extracellular deposition that was abolished by blebbistatin, confirming the importance of mechanotransduction in the cell response to the stiffness gradient. FGMs are a promising advancement for the repair of osteochondral tissue due to its heterogeneous nature. Gradient scaffolds consistently outperform monophasic scaffolds in osteochondral defect models, illustrating the importance of recapitulating *in vivo* gradients for successful osteochondral repair.

2.3.4 Models of cancer

FGMs are widely applicable to cancer models given the array of signaling that occurs in the tumor microenvironment. Tumor cells are constantly remodeling surrounding tissues and changing the native physiological environment, resulting in gradients in soluble cues and stiffness that signal surrounding cells. *In vitro* models can improve the collective understanding of how biological gradients drive tumorigenesis and metastasis to assist in the development of improved treatments.

Haptotaxis, the migration of cells in response to a gradient of surface-bound molecules, is a predominant mechanism of signaling in cancer in which fibronectin (FN) concentration varies substantially throughout tumors.^[154] Gradients of FN were formed in a microfluidic device to study the role of matricellular proteins on the migration of MDA-MB-231 breast adenocarcinoma cells. The results of this study identified a new haptotaxis mechanism, which is driven by the actin regulatory protein Mena that promotes ECM remodeling along FN gradients. Cells can also migrate in response to the alignment of ECM fibers. Specifically, MDA-MB-231 cells migrated faster on aligned collagen fibers compared to random, unaligned fibers.^[155] The spacing of ECM fibers is yet another important consideration for cancer cell migration. FN-coated nanoscale posts were fabricated with a gradient in spacing from 0.3 to 4.2 μm .^[156] When posts were coated with 10 $\mu\text{g mL}^{-1}$ of FN, invasive 1205Lu melanoma cells accumulated in areas of sparser spacing, while cells accumulated in denser arrays at 50 $\mu\text{g mL}^{-1}$ FN due to the balance of ECM-triggered signaling pathways PI(3)K–Akt and ROCK–MLCK. Breast cancer (MDA-MB-231), fibrosarcoma (HT1080), and glioblastoma (T98G) cells on a PA gel with a gradient in stiffness from 2 to 20 kPa underwent durotaxis, exhibiting biased migration towards the stiffer regions.^[157] Human cancer cells of varying tissue origins also exhibit durotaxis from soft to stiff regions of a substrate.^[157]

Some cancer models include an oxygen gradient to mimic hypoxia, which is a critical factor in the progression and metastasis of many cancers. Primary mouse sarcoma cells were encapsulated in oxygen (O_2)-controllable hydrogels which recreated pathophysiological O_2 levels *in vitro*.^[158] Compared to control gels, cell invasion was faster and extended over longer distances in the direction of increasing O_2 tension in gels with

oxygen gradients. Overall, FGMs can further elucidate mechanisms behind cancer cell migration and metastasis. The precise control of microfluidics makes them a common choice for modeling the cancer cell environment and examining cell response to individual parameters such as protein concentration or oxygen tension.

2.3.5 Drug screening platforms

FGMs are useful in diagnostic devices due to their ability to subject cells to a wide range of conditions, identify effective and cytotoxic concentrations of drugs, or determine how cells interact with ECM conditions. A high throughput drug system was developed using combinatorial concentrations of drugs generated by two microfluidic mixers, resulting in 64 unique combinations.^[159] The efficacy of chemotherapeutics on prostate cancer was then investigated by applying these combinations to human PC3 prostate cells while minimizing the volume of required reagents. Microfluidic devices can also be constructed to replicate *in vivo* environments of tumor cells to more accurately assess the dose-response effect of cells exposed to drugs. The chemotherapeutic effect of various drugs was studied in a colorectal tumor-on-a-chip system consisting of a central chamber surrounded by a pair of perfusable channels. By generating a gradient of chemotherapeutic drug, the platform established a dose-dependent response of exposed cells and enabled analysis of gene expression to identify new druggable targets. The hypoxia-dependent cytotoxicity of anticancer drugs has been investigated using microfluidic systems that enable the generation of reproducible oxygen gradients.^[160] Adenocarcinoma (A549) cells cultured in this device were treated with tirapazamine (TPZ) under various oxygen tensions. These studies revealed the improved potency of TPZ

under hypoxia compared to established chemotherapeutic agents such as cisplatin.^[161] Gradients of ECM can be utilized to examine cell response *in vitro*. A three-dimensional array of ECM gradients was bioprinted by controlling the ratio of a GelMA hydrogel, which contains native adhesion ligands, to a PEGDA hydrogel, which is bioinert and lacks endogenous adhesion motifs.^[162] The resulting array was used to screen the response of human periodontal ligament stem cells to the varying ECM content, with cell viability and spreading decreasing with increasing ratios of PEG. These platforms have the potential to advance personalized medicine, identify new potent drugs, and reduce healthcare expenses.

2.4 Conclusion and Future Outlook

FGMs are designed to replicate the heterogeneity of native tissues. If properly fabricated, FGMs could mimic the function of biological gradients such as mechanical support, presentation of instructive stimuli, application of physiologically relevant forces, and cell signaling. FGMs are created using a variety of techniques including light-based methods, 3D printing, microfluidics, and electrospinning. As discussed in this review, functional gradients have been utilized to create model systems such as bone-soft tissue interfaces that advance our understanding of physiology and pathology occurring at these interfacial tissues. Continued development of FGMs will expand their use to additional tissues such as nervous, cardiac, and dermal tissue that exhibit gradients in cell type, electroconductivity, and structure. Currently, many FGMs are engineered with linear gradients, yet gradients *in vivo* are often discontinuous or nonlinear. Cell differentiation, migration, and growth depend on nonlinear gradients that should be implemented in

scaffolds to better mimic native conditions.^[68] Upon implantation *in vivo*, FGMs may be subjected to external stimuli such as gradients in load. Many models of interfacial tissue do not presently consider the role of gradients in mechanical loading despite studies confirming cellular mechanosensitivity to loading.^[163] The inclusion of nonlinear gradients will increase the efficacy of FGMs.

At this time, the majority of studies using functional gradients focus on spatial distribution of some characteristic including composition, stiffness, inductive factor, among others. These parameters are often established *a priori*, providing limited opportunities for the gradients to evolve in response to cells. It is imperative to incorporate more dynamic, temporally dependent aspects into FGMs to mimic native processes such as gene expression and evolving biochemical signals during cell differentiation. Technologies such as slow-releasing nanoparticle delivery systems and cell-responsive hydrogels could regulate the evolution of gradients in a more natural, temporal manner.^[164, 165]

The efficacy of FGMs as model systems is dependent upon ease of fabrication, simplicity of use, and reproducibility in resulting data. For these FGMs to be widely available, the methods employed must be simple and should be high throughput in nature to ensure translation to the clinic. Microfluidic platforms meet these requirements due to their consistent fabrication methods and minimal required reagent volume. However, in order to maintain their ease-of-use, microfluidics sacrifice the complexity present in many native tissues. While they are appropriate for studying basic cell interactions such as durotaxis or haptotaxis, more complex models are needed to accurately model native gradients *in vitro*.

The successful translation of FGMs to the clinic must overcome several challenges. Standardized manufacturing approaches are required to improve reproducibility and enable broad adoption. In accordance with standardization techniques, improved strategies for quality assurance will ensure consistent gradient formation. Compared to homogeneous materials that exhibit predictable changes in biophysical properties, heterogeneous constructs have a range of values that must be verified, necessitating the development of improved technologies to characterize FGMs directly. The scale-up of constructs for large injuries that occur in the body represents another major challenge in the translation of FGMs to human patients. Large constructs require sufficient nutrient transport to enable survival of transplanted or invading cells. The combination of technologies such as 3D printing and electrospinning may facilitate the scaling up of constructs with graded components such as porosity and peptide concentration to promote vascularization. Tissue substitutes must also be customized to fit the defect sites of patients. The advancement of 3D printing combined with imaging modalities such as computed tomography (CT) may enable rapid prototyping of customized FGMs and increase their use in the clinic. By addressing these challenges, FGMs will provide a valuable tool for understanding and repairing heterogeneous tissues found in the body.

2.5 References

- [1] Y. Miyamoto, W.A. Kaysser, B.H. Rabin, A. Kawasaki, R.G. Ford, *Functionally Graded Materials: Design, Processing and Applications*, Springer US1999.
- [2] M. Koizumi, M. Niino, Overview of FGM Research in Japan, *MRS Bulletin* 20(1) (2013) 19-21.
- [3] T. Gong, J. Xie, J. Liao, T. Zhang, S. Lin, Y. Lin, Nanomaterials and bone regeneration, *Bone Res.* 3 (2015) 15029.
- [4] W. Pompe, H. Worch, M. Epple, W. Friess, M. Gelinsky, P. Greil, U. Hempel, D. Scharnweber, K. Schulte, Functionally graded materials for biomedical applications, *Mat Sci Eng a-Struct* 362(1-2) (2003) 40-60.
- [5] G.M. Genin, A. Kent, V. Birman, B. Wopenka, J.D. Pasteris, P.J. Marquez, S. Thomopoulos, Functional grading of mineral and collagen in the attachment of tendon to bone, *Biophys. J.* 97(4) (2009) 976-85.
- [6] J. Qu, A.R. Thoreson, Q. Chen, K.N. An, P.C. Amadio, C. Zhao, Tendon gradient mineralization for tendon to bone interface integration, *J. Orthop. Res.* 31(11) (2013) 1713-9.
- [7] H. Kwon, W.E. Brown, C.A. Lee, D. Wang, N. Paschos, J.C. Hu, K.A. Athanasiou, Surgical and tissue engineering strategies for articular cartilage and meniscus repair, *Nat. Rev. Rheumatol.* 15(9) (2019) 550-570.
- [8] J. Wu, Z. Mao, H. Tan, L. Han, T. Ren, C. Gao, Gradient biomaterials and their influences on cell migration, *Interface Focus* 2(3) (2012) 337-55.
- [9] J. Li, D.J. Mooney, Designing hydrogels for controlled drug delivery, *Nat. Rev. Mater.* 1(12) (2016) 16071.

- [10] Q. Chai, Y. Jiao, X. Yu, Hydrogels for Biomedical Applications: Their Characteristics and the Mechanisms behind Them, *Gels* 3(1) (2017).
- [11] I. Gadjanski, Recent advances on gradient hydrogels in biomimetic cartilage tissue engineering, *F1000Res.* 6 (2017).
- [12] L. Yahia, History and Applications of Hydrogels, *J. Biomed. Sci.* 04(02) (2015).
- [13] M.J. Madou, *Fundamentals of Microfabrication: The Science of Miniaturization*, Second Edition, Taylor & Francis 2002.
- [14] G. Jain, A.J. Ford, P. Rajagopalan, Opposing Rigidity-Protein Gradients Reverse Fibroblast Durotaxis, *ACS Biomater. Sci. Eng.* 1(8) (2015) 621-631.
- [15] J.R. Tse, A.J. Engler, Stiffness gradients mimicking in vivo tissue variation regulate mesenchymal stem cell fate, *PLoS One* 6(1) (2011) e15978.
- [16] L.G. Major, A.W. Holle, J.L. Young, M.S. Hepburn, K. Jeong, I.L. Chin, R.W. Sanderson, J.H. Jeong, Z.M. Aman, B.F. Kennedy, Y. Hwang, D.W. Han, H.W. Park, K.L. Guan, J.P. Spatz, Y.S. Choi, Volume Adaptation Controls Stem Cell Mechanotransduction, *ACS Appl. Mater. Interfaces* 11(49) (2019) 45520-45530.
- [17] W.J. Hadden, J.L. Young, A.W. Holle, M.L. McFetridge, D.Y. Kim, P. Wijesinghe, H. Taylor-Weiner, J.H. Wen, A.R. Lee, K. Bieback, B.N. Vo, D.D. Sampson, B.F. Kennedy, J.P. Spatz, A.J. Engler, Y.S. Choi, Stem cell migration and mechanotransduction on linear stiffness gradient hydrogels, *Proc. Natl. Acad. Sci. U. S. A.* 114(22) (2017) 5647-5652.
- [18] A.M. Kloxin, J.A. Benton, K.S. Anseth, In situ elasticity modulation with dynamic substrates to direct cell phenotype, *Biomaterials* 31(1) (2010) 1-8.

- [19] R.A. Marklein, J.A. Burdick, Spatially controlled hydrogel mechanics to modulate stem cell interactions, *Soft Matter* 6(1) (2010) 136-143.
- [20] R. Sunyer, A.J. Jin, R. Nossal, D.L. Sackett, Fabrication of hydrogels with steep stiffness gradients for studying cell mechanical response, *PLoS One* 7(10) (2012) e46107.
- [21] A.M. Kloxin, A.M. Kasko, C.N. Salinas, K.S. Anseth, Photodegradable hydrogels for dynamic tuning of physical and chemical properties, *Science* 324(5923) (2009) 59-63.
- [22] L.E. Corum, V. Hlady, Screening platelet-surface interactions using negative surface charge gradients, *Biomaterials* 31(12) (2010) 3148-55.
- [23] Y.X. Ding, S. Streitmatter, B.E. Wright, V. Hlady, Spatial variation of the charge and sulfur oxidation state in a surface gradient affects plasma protein adsorption, *Langmuir* 26(14) (2010) 12140-6.
- [24] S.C.P. Norris, P. Tseng, A.M. Kasko, Direct Gradient Photolithography of Photodegradable Hydrogels with Patterned Stiffness Control with Submicrometer Resolution, *ACS Biomater. Sci. Eng.* 2(8) (2016) 1309-1318.
- [25] E.L. Horn-Ranney, J.L. Curley, G.C. Catig, R.M. Huval, M.J. Moore, Structural and molecular micropatterning of dual hydrogel constructs for neural growth models using photochemical strategies, *Biomed. Microdevices* 15(1) (2013) 49-61.
- [26] W. Denk, J.H. Strickler, W.W. Webb, Two-photon laser scanning fluorescence microscopy, *Science* 248(4951) (1990) 73-6.

- [27] R.Y. Tam, L.J. Smith, M.S. Shoichet, Engineering Cellular Microenvironments with Photo- and Enzymatically Responsive Hydrogels: Toward Biomimetic 3D Cell Culture Models, *Acc. Chem. Res.* 50(4) (2017) 703-713.
- [28] Y. Aizawa, M.S. Shoichet, The role of endothelial cells in the retinal stem and progenitor cell niche within a 3D engineered hydrogel matrix, *Biomaterials* 33(21) (2012) 5198-205.
- [29] S.A. DeLong, A.S. Gobin, J.L. West, Covalent immobilization of RGDS on hydrogel surfaces to direct cell alignment and migration, *J. Control. Release* 109(1-3) (2005) 139-48.
- [30] Y.H. Yang, Z. Khan, C. Ma, H.J. Lim, L.A. Smith Callahan, Optimization of adhesive conditions for neural differentiation of murine embryonic stem cells using hydrogels functionalized with continuous Ile-Lys-Val-Ala-Val concentration gradients, *Acta Biomater.* 21 (2015) 55-62.
- [31] M.C. Hill, M.K. Nguyen, O. Jeon, E. Alsberg, Spatial control of cell gene expression by siRNA gradients in biodegradable hydrogels, *Adv. Healthc. Mater.* 4(5) (2015) 714-22.
- [32] O. Jeon, D.S. Alt, S.W. Linderman, E. Alsberg, Biochemical and physical signal gradients in hydrogels to control stem cell behavior, *Adv. Mater.* 25(44) (2013) 6366-72.
- [33] H.J. Lim, Z. Khan, T.S. Wilems, X. Lu, T.H. Perera, Y.E. Kurosu, K.T. Ravivarapu, M.C. Mosley, L.A.S. Callahan, Human Induced Pluripotent Stem Cell Derived Neural Stem Cell Survival and Neural Differentiation on Polyethylene Glycol Dimethacrylate Hydrogels Containing a Continuous Concentration

- Gradient of N-Cadherin Derived Peptide His-Ala-Val-Asp-Ile, ACS Biomater. Sci. Eng. 3(5) (2017) 776-781.
- [34] D. Zhu, X. Tong, P. Trinh, F. Yang, Mimicking Cartilage Tissue Zonal Organization by Engineering Tissue-Scale Gradient Hydrogels as 3D Cell Niche, Tissue Eng., Part A 24(1-2) (2018) 1-10.
- [35] E.K.U. Larsen, N.B. Larsen, K. Almdal, E.K.U. Larsen, N.B. Larsen, K. Almdal, Multimaterial Hydrogel with Widely Tunable Elasticity by Selective Photopolymerization of PEG Diacrylate and Epoxy Monomers, J Polym Sci Pol Phys 54(13) (2016) 1195-1201.
- [36] B.M. Bailey, L.N. Nail, M.A. Grunlan, Continuous gradient scaffolds for rapid screening of cell-material interactions and interfacial tissue regeneration, Acta Biomater. 9(9) (2013) 8254-61.
- [37] H. Ko, K. Suthiwanich, H. Mary, S. Zanganeh, S.K. Hu, S. Ahadian, Y. Yang, G. Choi, K. Fetah, Y. Niu, J.J. Mao, A. Khademhosseini, A simple layer-stacking technique to generate biomolecular and mechanical gradients in photocrosslinkable hydrogels, Biofabrication 11(2) (2019) 025014.
- [38] P. Zorlutuna, N. Annabi, G. Camci-Unal, M. Nikkhah, J.M. Cha, J.W. Nichol, A. Manbachi, H. Bae, S. Chen, A. Khademhosseini, Microfabricated biomaterials for engineering 3D tissues, Adv. Mater. 24(14) (2012) 1782-804.
- [39] T.U. Nguyen, K.E. Watkins, V. Kishore, Photochemically crosslinked cell-laden methacrylated collagen hydrogels with high cell viability and functionality, J. Biomed. Mater. Res., Part A 107(7) (2019) 1541-1550.

- [40] S. Khorshidi, A. Karkhaneh, A review on gradient hydrogel/fiber scaffolds for osteochondral regeneration, *J. Tissue Eng. Regen. Med.* 12(4) (2018) e1974-e1990.
- [41] S. Knowlton, S. Anand, T. Shah, S. Tasoglu, Bioprinting for Neural Tissue Engineering, *Trends Neurosci.* 41(1) (2018) 31-46.
- [42] J.L. Bouthillier, Carbon3D – Terminator Inspired 3D Printing Technology, 2015. <http://bootsindustries.com/carbon3d-terminator-inspired-3d-printing-technology/>. (Accessed 18.10.2019).
- [43] T.J. Hinton, Q. Jallerat, R.N. Palchesko, J.H. Park, M.S. Grodzicki, H.J. Shue, M.H. Ramadan, A.R. Hudson, A.W. Feinberg, Three-dimensional printing of complex biological structures by freeform reversible embedding of suspended hydrogels, *Sci. Adv.* 1(9) (2015) e1500758.
- [44] R. Scaffaro, F. Lopresti, A. Maio, F. Sutera, L. Botta, Development of polymeric functionally graded scaffolds: a brief review, *J. Appl. Biomater. Funct. Mater.* 15(2) (2017) e107-e121.
- [45] S.E. Kim, E.C. Harker, A.C. De Leon, R.C. Advincula, J.K. Pokorski, Coextruded, aligned, and gradient-modified poly(epsilon-caprolactone) fibers as platforms for neural growth, *Biomacromolecules* 16(3) (2015) 860-7.
- [46] A. Di Luca, A. Longoni, G. Criscenti, I. Lorenzo-Moldero, M. Klein-Gunnewiek, J. Vancso, C. van Blitterswijk, C. Mota, L. Moroni, Surface energy and stiffness discrete gradients in additive manufactured scaffolds for osteochondral regeneration, *Biofabrication* 8(1) (2016) 015014.

- [47] C.H. Lee, S.A. Rodeo, L.A. Fortier, C. Lu, C. Erisken, J.J. Mao, Protein-releasing polymeric scaffolds induce fibrochondrocytic differentiation of endogenous cells for knee meniscus regeneration in sheep, *Sci. Transl. Med.* 6(266) (2014) 266ra171.
- [48] U. D'Amora, M. D'Este, D. Eglin, F. Safari, C.M. Sprecher, A. Gloria, R. De Santis, M. Alini, L. Ambrosio, Collagen density gradient on three-dimensional printed poly(epsilon-caprolactone) scaffolds for interface tissue engineering, *J. Tissue Eng. Regen. Med.* 12(2) (2018) 321-329.
- [49] S. Rhee, J.L. Puetzer, B.N. Mason, C.A. Reinhart-King, L.J. Bonassar, 3D Bioprinting of Spatially Heterogeneous Collagen Constructs for Cartilage Tissue Engineering, *ACS Biomater. Sci. Eng.* 2(10) (2016) 1800-1805.
- [50] X. Ren, F. Wang, C. Chen, X. Gong, L. Yin, L. Yang, Engineering zonal cartilage through bioprinting collagen type II hydrogel constructs with biomimetic chondrocyte density gradient, *BMC Musculoskelet. Disord.* 17 (2016) 301.
- [51] K.Y. Lee, D.J. Mooney, Alginate: properties and biomedical applications, *Prog. Polym. Sci.* 37(1) (2012) 106-126.
- [52] T. Gonzalez-Fernandez, S. Rathan, C. Hobbs, P. Pitacco, F.E. Freeman, G.M. Cunniffe, N.J. Dunne, H.O. McCarthy, V. Nicolosi, F.J. O'Brien, D.J. Kelly, Pore-forming bioinks to enable spatio-temporally defined gene delivery in bioprinted tissues, *J. Control. Release* 301 (2019) 13-27.
- [53] S. Sultan, A.P. Mathew, 3D printed scaffolds with gradient porosity based on a cellulose nanocrystal hydrogel, *Nanoscale* 10(9) (2018) 4421-4431.

- [54] C. Petit, L. Montanaro, P. Palmero, Functionally graded ceramics for biomedical application: Concept, manufacturing, and properties, *Int. J. Appl. Ceram.* 15(4) (2018) 820-840.
- [55] F. Gao, Z.Y. Xu, Q.F. Liang, B. Liu, H.F. Li, Y.H. Wu, Y.Y. Zhang, Z.F. Lin, M.M. Wu, C.S. Ruan, W.G. Liu, Direct 3D Printing of High Strength Biohybrid Gradient Hydrogel Scaffolds for Efficient Repair of Osteochondral Defect, *Adv. Funct. Mater.* 28(13) (2018).
- [56] S.M. Bittner, B.T. Smith, L. Diaz-Gomez, C.D. Hudgins, A.J. Melchiorri, D.W. Scott, J.P. Fisher, A.G. Mikos, Fabrication and mechanical characterization of 3D printed vertical uniform and gradient scaffolds for bone and osteochondral tissue engineering, *Acta Biomater.* 90 (2019) 37-48.
- [57] J. Liu, L. Li, H. Suo, M. Yan, J. Yin, J. Fu, 3D printing of biomimetic multi-layered GelMA/nHA scaffold for osteochondral defect repair, *Mater. Des.* 171 (2019).
- [58] J.R. Jones, Review of bioactive glass: from Hench to hybrids, *Acta Biomater.* 9(1) (2013) 4457-86.
- [59] F. Gao, Z. Xu, Q. Liang, H. Li, L. Peng, M. Wu, X. Zhao, X. Cui, C. Ruan, W. Liu, Osteochondral Regeneration with 3D-Printed Biodegradable High-Strength Supramolecular Polymer Reinforced-Gelatin Hydrogel Scaffolds, *Adv. Sci.* 6(15) (2019) 1900867.
- [60] P. Gingter, A.M. Watjen, M. Kramer, R. Telle, Functionally Graded Ceramic Structures by Direct Thermal Inkjet Printing, *J. Ceram. Sci. Technol.* 6(2) (2015) 119-124.

- [61] J.A. Phillippi, E. Miller, L. Weiss, J. Huard, A. Waggoner, P. Campbell, Microenvironments engineered by inkjet bioprinting spatially direct adult stem cells toward muscle- and bone-like subpopulations, *Stem Cells* 26(1) (2008) 127-34.
- [62] E.D. Miller, J.A. Phillippi, G.W. Fisher, P.G. Campbell, L.M. Walker, L.E. Weiss, Inkjet printing of growth factor concentration gradients and combinatorial arrays immobilized on biologically-relevant substrates, *Comb. Chem. High Throughput Screening* 12(6) (2009) 604-18.
- [63] K.M. Hubka, D.D. Carson, D.A. Harrington, M.C. Farach-Carson, Perlecan domain I gradients establish stable biomimetic heparin binding growth factor gradients for cell migration in hydrogels, *Acta Biomater.* 97 (2019) 385-398.
- [64] C. Mandrycky, Z. Wang, K. Kim, D.H. Kim, 3D bioprinting for engineering complex tissues, *Biotechnol. Adv.* 34(4) (2016) 422-434.
- [65] X. Wang, Z.M. Liu, Y. Pang, Concentration gradient generation methods based on microfluidic systems, *Rsc Adv* 7(48) (2017) 29966-29984.
- [66] C. Chen, B.T. Mehl, A.S. Munshi, A.D. Townsend, D.M. Spence, R.S. Martin, 3D-printed Microfluidic Devices: Fabrication, Advantages and Limitations-a Mini Review, *Anal. Methods* 8(31) (2016) 6005-6012.
- [67] S.G. Uzel, O.C. Amadi, T.M. Pearl, R.T. Lee, P.T. So, R.D. Kamm, Simultaneous or Sequential Orthogonal Gradient Formation in a 3D Cell Culture Microfluidic Platform, *Small* 12(5) (2016) 612-22.
- [68] S. Selimovic, W.Y. Sim, S.B. Kim, Y.H. Jang, W.G. Lee, M. Khabiry, H. Bae, S. Jambovane, J.W. Hong, A. Khademhosseini, Generating nonlinear concentration

- gradients in microfluidic devices for cell studies, *Anal. Chem.* 83(6) (2011) 2020-8.
- [69] X. Shi, J. Zhou, Y. Zhao, L. Li, H. Wu, Gradient-regulated hydrogel for interface tissue engineering: steering simultaneous osteo/chondrogenesis of stem cells on a chip, *Adv. Healthc. Mater.* 2(6) (2013) 846-53.
- [70] L. Wertheim, A. Shapira, R.J. Amir, T. Dvir, A microfluidic chip containing multiple 3D nanofibrous scaffolds for culturing human pluripotent stem cells, *Nanotechnology* 29(13) (2018) 13LT01.
- [71] C.M. Morrow, A. Mukherjee, M.A. Traore, E.J. Leaman, A. Kim, E.M. Smith, A.S. Nain, B. Behkam, Integrating nanofibers with biochemical gradients to investigate physiologically-relevant fibroblast chemotaxis, *Lab Chip* 19(21) (2019) 3641-3651.
- [72] S. Garcia, R. Sunyer, A. Olivares, J. Noailly, J. Atencia, X. Trepate, Generation of stable orthogonal gradients of chemical concentration and substrate stiffness in a microfluidic device, *Lab Chip* 15(12) (2015) 2606-14.
- [73] H.Y. Hsieh, G. Camci-Unal, T.W. Huang, R. Liao, T.J. Chen, A. Paul, F.G. Tseng, A. Khademhosseini, Gradient static-strain stimulation in a microfluidic chip for 3D cellular alignment, *Lab Chip* 14(3) (2014) 482-93.
- [74] S. Bazban-Shotorbani, E. Dashtimoghadam, A. Karkhaneh, M.M. Hasani-Sadrabadi, K.I. Jacob, Microfluidic Directed Synthesis of Alginate Nanogels with Tunable Pore Size for Efficient Protein Delivery, *Langmuir* 32(19) (2016) 4996-5003.

- [75] S. Xin, J. Dai, C.A. Gregory, A. Han, D.L. Alge, Creating Physicochemical Gradients in Modular Microporous Annealed Particle Hydrogels via a Microfluidic Method, *Advanced Functional Materials* 30(6) (2019).
- [76] F. Tonon, G.G. Giobbe, A. Zambon, C. Luni, O. Gagliano, A. Floreani, G. Grassi, N. Elvassore, In vitro metabolic zonation through oxygen gradient on a chip, *Sci. Rep.* 9(1) (2019) 13557.
- [77] S.F. Lam, V.S. Shirure, Y.E. Chu, A.G. Soetikno, S.C. George, Microfluidic device to attain high spatial and temporal control of oxygen, *PLoS One* 13(12) (2018) e0209574.
- [78] Z.Z. Liu, H. Sun, K.N. Ren, A Multiplexed, Gradient-Based, Full-Hydrogel Microfluidic Platform for Rapid, High-Throughput Antimicrobial Susceptibility Testing, *Chempluschem* 82(5) (2017) 792-801.
- [79] M.R. Carvalho, D. Barata, L.M. Teixeira, S. Giselbrecht, R.L. Reis, J.M. Oliveira, R. Truckenmuller, P. Habibovic, Colorectal tumor-on-a-chip system: A 3D tool for precision onco-nanomedicine, *Sci. Adv.* 5(5) (2019) eaaw1317.
- [80] F. Zhang, C. Tian, W. Liu, K. Wang, Y. Wei, H. Wang, J. Wang, S. Liu, Determination of Benzopyrene-Induced Lung Inflammatory and Cytotoxic Injury in a Chemical Gradient-Integrated Microfluidic Bronchial Epithelium System, *ACS Sens.* 3(12) (2018) 2716-2725.
- [81] H.G. Sundararaghavan, S.N. Masand, D.I. Shreiber, Microfluidic generation of haptotactic gradients through 3D collagen gels for enhanced neurite growth, *J. Neurotrauma* 28(11) (2011) 2377-87.

- [82] N. Movilla, C. Borau, C. Valero, J.M. Garcia-Aznar, Degradation of extracellular matrix regulates osteoblast migration: A microfluidic-based study, *Bone* 107 (2018) 10-17.
- [83] F.Y. Lin, J.Y. Lin, K.Y. Lo, Y.S. Sun, Use Microfluidic Chips to Study the Phototaxis of Lung Cancer Cells, *Int. J. Mol. Sci.* 20(18) (2019).
- [84] M. Costantini, J. Jaroszewicz, L. Kozon, K. Szlajak, W. Swieszkowski, P. Garstecki, C. Stubenrauch, A. Barbetta, J. Guzowski, 3D-Printing of Functionally Graded Porous Materials Using On-Demand Reconfigurable Microfluidics, *Angew. Chem. Int. Ed. Engl.* 58(23) (2019) 7620-7625.
- [85] X. Zhang, X. Gao, L. Jiang, J. Qin, Flexible generation of gradient electrospinning nanofibers using a microfluidic assisted approach, *Langmuir* 28(26) (2012) 10026-32.
- [86] J. Xue, J. Xie, W. Liu, Y. Xia, Electrospun Nanofibers: New Concepts, Materials, and Applications, *Acc. Chem. Res.* 50(8) (2017) 1976-1987.
- [87] G.C. Ingavle, J.K. Leach, Advancements in electrospinning of polymeric nanofibrous scaffolds for tissue engineering, *Tissue Eng., Part B* 20(4) (2014) 277-93.
- [88] D.I. Braghirolli, D. Steffens, P. Pranke, Electrospinning for regenerative medicine: a review of the main topics, *Drug Discov. Today* 19(6) (2014) 743-53.
- [89] F.J. Bye, J. Bissoli, L. Black, A.J. Bullock, S. Puwanun, K. Moharamzadeh, G.C. Reilly, A.J. Ryan, S. MacNeil, Development of bilayer and trilayer nanofibrous/microfibrous scaffolds for regenerative medicine, *Biomater Sci-Uk* 1(9) (2013) 942-951.

- [90] Y.F. Wang, H.F. Guo, D.J. Ying, Multilayer scaffold of electrospun PLA-PCL-collagen nanofibers as a dural substitute, *J. Biomed. Mater. Res., Part B* 101(8) (2013) 1359-66.
- [91] F. Qu, J.L. Holloway, J.L. Esterhai, J.A. Burdick, R.L. Mauck, Programmed biomolecule delivery to enable and direct cell migration for connective tissue repair, *Nat. Commun.* 8(1) (2017) 1780.
- [92] J.S. Lee, Y. Jin, H.J. Park, K. Yang, M.S. Lee, H.S. Yang, S.W. Cho, In Situ Bone Tissue Engineering With an Endogenous Stem Cell Mobilizer and Osteoinductive Nanofibrous Polymeric Scaffolds, *Biotechnol. J.* 12(12) (2017).
- [93] N. Mohan, J. Wilson, D. Joseph, D. Vaikkath, P.D. Nair, Biomimetic fiber assembled gradient hydrogel to engineer glycosaminoglycan enriched and mineralized cartilage: An in vitro study, *J. Biomed. Mater. Res., Part A* 103(12) (2015) 3896-906.
- [94] J.K. He, T. Qin, Y.X. Liu, X. Li, D.C. Li, Z.M. Jin, Electrospinning of nanofibrous scaffolds with continuous structure and material gradients, *Mater Lett* 137 (2014) 393-397.
- [95] J. Pu, K. Komvopoulos, Mechanical properties of electrospun bilayer fibrous membranes as potential scaffolds for tissue engineering, *Acta Biomater.* 10(6) (2014) 2718-26.
- [96] J. Pu, F. Yuan, S. Li, K. Komvopoulos, Electrospun bilayer fibrous scaffolds for enhanced cell infiltration and vascularization in vivo, *Acta Biomater.* 13 (2015) 131-41.

- [97] J. Lipner, W. Liu, Y. Liu, J. Boyle, G.M. Genin, Y. Xia, S. Thomopoulos, The mechanics of PLGA nanofiber scaffolds with biomimetic gradients in mineral for tendon-to-bone repair, *J. Mech. Behav. Biomed. Mater.* 40 (2014) 59-68.
- [98] W. Liu, J. Lipner, J. Xie, C.N. Manning, S. Thomopoulos, Y. Xia, Nanofiber scaffolds with gradients in mineral content for spatial control of osteogenesis, *ACS Appl. Mater. Interfaces* 6(4) (2014) 2842-9.
- [99] T. Wu, C. Huang, D. Li, A. Yin, W. Liu, J. Wang, J. Chen, H. Ei-Hamshary, S.S. Al-Deyab, X. Mo, A multi-layered vascular scaffold with symmetrical structure by bi-directional gradient electrospinning, *Colloids Surf. B Biointerfaces* 133 (2015) 179-88.
- [100] G. Yang, H. Lin, B.B. Rothrauff, S. Yu, R.S. Tuan, Multilayered polycaprolactone/gelatin fiber-hydrogel composite for tendon tissue engineering, *Acta Biomater.* 35 (2016) 68-76.
- [101] A.P. Kishan, A.B. Robbins, S.F. Mohiuddin, M. Jiang, M.R. Moreno, E.M. Cosgriff-Hernandez, Fabrication of macromolecular gradients in aligned fiber scaffolds using a combination of in-line blending and air-gap electrospinning, *Acta Biomater.* 56 (2017) 118-128.
- [102] H.-Y. Mi, X. Jing, E. Yu, J. McNulty, X.-F. Peng, L.-S. Turng, Fabrication of triple-layered vascular scaffolds by combining electrospinning, braiding, and thermally induced phase separation, *Mater Lett* 161 (2015) 305-308.
- [103] A.R. Morais, N. Alencar Edo, F.H. Xavier Junior, C.M. de Oliveira, H.R. Marcelino, G. Barratt, H. Fessi, E.S. do Egito, A. Elaissari, Freeze-drying of emulsified systems: A review, *Int. J. Pharm.* 503(1-2) (2016) 102-14.

- [104] S. Deville, Freeze-Casting of Porous Biomaterials: Structure, Properties and Opportunities, *Materials* 3(3) (2010) 1913-1927.
- [105] Y. Zhu, H. Wu, S. Sun, T. Zhou, J. Wu, Y. Wan, Designed composites for mimicking compressive mechanical properties of articular cartilage matrix, *J. Mech. Behav. Biomed. Mater.* 36 (2014) 32-46.
- [106] T.J. Levingstone, A. Matsiko, G.R. Dickson, F.J. O'Brien, J.P. Gleeson, A biomimetic multi-layered collagen-based scaffold for osteochondral repair, *Acta Biomater.* 10(5) (2014) 1996-2004.
- [107] T.J. Levingstone, A. Ramesh, R.T. Brady, P.A.J. Brama, C. Kearney, J.P. Gleeson, F.J. O'Brien, Cell-free multi-layered collagen-based scaffolds demonstrate layer specific regeneration of functional osteochondral tissue in caprine joints, *Biomaterials* 87 (2016) 69-81.
- [108] B.S. Kim, E.J. Kim, J.S. Choi, J.H. Jeong, C.H. Jo, Y.W. Cho, Human collagen-based multilayer scaffolds for tendon-to-bone interface tissue engineering, *J. Biomed. Mater. Res., Part A* 102(11) (2014) 4044-54.
- [109] D. Algul, H. Sipahi, A. Aydin, F. Kelleci, S. Ozdatli, F.G. Yener, Biocompatibility of biomimetic multilayered alginate-chitosan/beta-TCP scaffold for osteochondral tissue, *Int. J. Biol. Macromol.* 79 (2015) 363-9.
- [110] P. Yusong, S. Qianqian, P. Chengling, W. Jing, Prediction of mechanical properties of multilayer gradient hydroxyapatite reinforced poly(vinyl alcohol) gel biomaterial, *J. Biomed. Mater. Res., Part B* 101(5) (2013) 729-35.
- [111] X. Duan, X. Zhu, X. Dong, J. Yang, F. Huang, S. Cen, F. Leung, H. Fan, Z. Xiang, Repair of large osteochondral defects in a beagle model with a novel type

- I collagen/glycosaminoglycan-porous titanium biphasic scaffold, *Mater. Sci. Eng., C* 33(7) (2013) 3951-7.
- [112] Y. Wang, R. Xu, G. Luo, Q. Lei, Q. Shu, Z. Yao, H. Li, J. Zhou, J. Tan, S. Yang, R. Zhan, W. He, J. Wu, Biomimetic fibroblast-loaded artificial dermis with "sandwich" structure and designed gradient pore sizes promotes wound healing by favoring granulation tissue formation and wound re-epithelialization, *Acta Biomater.* 30 (2016) 246-257.
- [113] L. Zhang, R. Le Coz-Botrel, C. Beddoes, T. Sjostrom, B. Su, Gelatin freeze casting of biomimetic titanium alloy with anisotropic and gradient pore structure, *Biomed. Mater.* 12(1) (2017) 015014.
- [114] Z. Hou, F. Ye, Q. Liu, L. Liu, H. Jiang, S. Zhang, Pore Architectures and Mechanical Properties of Porous alpha-SiAlON Ceramics Fabricated via Unidirectional Freeze Casting Based on Camphene-Templating, *Materials* 12(5) (2019).
- [115] H. Bai, D. Wang, B. Delattre, W. Gao, J. De Coninck, S. Li, A.P. Tomsia, Biomimetic gradient scaffold from ice-templating for self-seeding of cells with capillary effect, *Acta Biomater.* 20 (2015) 113-119.
- [116] S. Zhang, L. Chen, Y. Jiang, Y. Cai, G. Xu, T. Tong, W. Zhang, L. Wang, J. Ji, P. Shi, H.W. Ouyang, Bi-layer collagen/microporous electrospun nanofiber scaffold improves the osteochondral regeneration, *Acta Biomater.* 9(7) (2013) 7236-47.
- [117] L.D. Harris, B.S. Kim, D.J. Mooney, Open pore biodegradable matrices formed with gas foaming, *J. Biomed. Mater. Res.* 42(3) (1998) 396-402.

- [118] A. Prasad, M.R. Sankar, V. Katiyar, State of Art on Solvent Casting Particulate Leaching Method for Orthopedic Scaffolds Fabrication, *Mater Today-Proc* 4(2) (2017) 898-907.
- [119] P. Duan, Z. Pan, L. Cao, Y. He, H. Wang, Z. Qu, J. Dong, J. Ding, The effects of pore size in bilayered poly(lactide-co-glycolide) scaffolds on restoring osteochondral defects in rabbits, *J. Biomed. Mater. Res., Part A* 102(1) (2014) 180-92.
- [120] P. Giannoni, E. Lazzarini, L. Ceseracciu, A.C. Barone, R. Quarto, S. Scaglione, Design and characterization of a tissue-engineered bilayer scaffold for osteochondral tissue repair, *J. Tissue Eng. Regen. Med.* 9(10) (2015) 1182-92.
- [121] R. Scaffaro, F. Lopresti, L. Botta, S. Rigogliuso, G. Gherzi, Melt Processed PCL/PEG Scaffold With Discrete Pore Size Gradient for Selective Cellular Infiltration, *Macromol Mater Eng* 301(2) (2016) 182-190.
- [122] R. Scaffaro, F. Lopresti, L. Botta, S. Rigogliuso, G. Gherzi, Preparation of three-layered porous PLA/PEG scaffold: relationship between morphology, mechanical behavior and cell permeability, *J. Mech. Behav. Biomed. Mater.* 54 (2016) 8-20.
- [123] R. Scaffaro, F. Lopresti, L. Botta, S. Rigogliuso, G. Gherzi, Integration of PCL and PLA in a monolithic porous scaffold for interface tissue engineering, *J. Mech. Behav. Biomed. Mater.* 63 (2016) 303-313.
- [124] K. Jamuna-Thevi, N.N. Saarani, M.R. Abdul Kadir, H. Hermawan, Triple-layered PLGA/nanoapatite/lauric acid graded composite membrane for periodontal guided bone regeneration, *Mater. Sci. Eng., C* 43 (2014) 253-63.

- [125] T.T. Nie, L. Xue, M. Ge, H.Y. Ma, J.C. Zhang, Fabrication of poly(L-lactic acid) tissue engineering scaffolds with precisely controlled gradient structure, *Mater. Lett.* 176 (2016) 25-28.
- [126] E. Bayrak, P. Yilgor Huri, Engineering Musculoskeletal Tissue Interfaces, *Frontiers in Materials* 5 (2018).
- [127] M. Benjamin, H. Toumi, J.R. Ralphs, G. Bydder, T.M. Best, S. Milz, Where tendons and ligaments meet bone: attachment sites ('entheses') in relation to exercise and/or mechanical load, *J. Anat.* 208(4) (2006) 471-90.
- [128] M. Benjamin, T. Kumai, S. Milz, B.M. Boszczyk, A.A. Boszczyk, J.R. Ralphs, The skeletal attachment of tendons - tendon 'entheses', *Comp. Biochem. Physiol., Part A: Mol. Integr. Physiol.* 133(4) (2002) 931-945.
- [129] A. Yamamoto, K. Takagishi, T. Osawa, T. Yanagawa, D. Nakajima, H. Shitara, T. Kobayashi, Prevalence and risk factors of a rotator cuff tear in the general population, *J. Shoulder Elbow Surg.* 19(1) (2010) 116-20.
- [130] I. Calejo, R. Costa-Almeida, R.L. Reis, M.E. Gomes, Enthesis Tissue Engineering: Biological Requirements Meet at the Interface, *Tissue Eng.. Part B* 25(4) (2019) 330-356.
- [131] C.C. Kaeding, B. Aros, A. Pedroza, E. Pifel, A. Amendola, J.T. Andrish, W.R. Dunn, R.G. Marx, E.C. McCarty, R.D. Parker, R.W. Wright, K.P. Spindler, Allograft Versus Autograft Anterior Cruciate Ligament Reconstruction: Predictors of Failure From a MOON Prospective Longitudinal Cohort, *Sports Health* 3(1) (2011) 73-81.

- [132] A. Robertson, R.W. Nutton, J.F. Keating, Current trends in the use of tendon allografts in orthopaedic surgery, *J. Bone Joint Surg. Br.* 88(8) (2006) 988-92.
- [133] P. Lui, P. Zhang, K. Chan, L. Qin, Biology and augmentation of tendon-bone insertion repair, *J. Orthop. Surg. Res.* 5 (2010) 59.
- [134] J. Apostolakos, T.J. Durant, C.R. Dwyer, R.P. Russell, J.H. Weinreb, F. Alaei, K. Beitzel, M.B. McCarthy, M.P. Cote, A.D. Mazzocca, The enthesis: a review of the tendon-to-bone insertion, *Muscles Ligaments Tendons J.* 4(3) (2014) 333-42.
- [135] S. Font Tellado, E.R. Balmayor, M. Van Griensven, Strategies to engineer tendon/ligament-to-bone interface: Biomaterials, cells and growth factors, *Adv. Drug Deliv. Rev.* 94 (2015) 126-40.
- [136] G. Criscenti, A. Longoni, A. Di Luca, C. De Maria, C.A. van Blitterswijk, G. Vozzi, L. Moroni, Triphasic scaffolds for the regeneration of the bone-ligament interface, *Biofabrication* 8(1) (2016) 015009.
- [137] S. Samavedi, P. Vaidya, P. Gaddam, A.R. Whittington, A.S. Goldstein, Electrospun meshes possessing region-wise differences in fiber orientation, diameter, chemistry and mechanical properties for engineering bone-ligament-bone tissues, *Biotechnol. Bioeng.* 111(12) (2014) 2549-59.
- [138] J. Nowlin, M.A. Bismi, B. Delpech, P. Dumas, Y. Zhou, G.Z. Tan, Engineering the hard-soft tissue interface with random-to-aligned nanofiber scaffolds, *Nanobiomedicine* 5 (2018) 1849543518803538.
- [139] Z.F. Lin, X.J. Zhao, S. Chen, C. Du, Osteogenic and tenogenic induction of hBMSCs by an integrated nanofibrous scaffold with chemical and structural

- mimicry of the bone-ligament connection, *J Mater Chem B* 5(5) (2017) 1015-1027.
- [140] A. Tevlek, P. Hosseinian, C. Ogutcu, M. Turk, H.M. Aydin, Bi-layered constructs of poly(glycerol-sebacate)-beta-tricalcium phosphate for bone-soft tissue interface applications, *Mater. Sci. Eng., C* 72 (2017) 316-324.
- [141] S. Font Tellado, W. Bonani, E.R. Balmayor, P. Foehr, A. Motta, C. Migliaresi, M. van Griensven, (*) Fabrication and Characterization of Biphasic Silk Fibroin Scaffolds for Tendon/Ligament-to-Bone Tissue Engineering, *Tissue Eng., Part A* 23(15-16) (2017) 859-872.
- [142] S.R. Caliarì, D.W. Weisgerber, W.K. Grier, Z. Mahmassani, M.D. Boppart, B.A. Harley, Collagen Scaffolds Incorporating Coincident Gradations of Instructive Structural and Biochemical Cues for Osteotendinous Junction Engineering, *Adv. Healthc. Mater.* 4(6) (2015) 831-7.
- [143] M.K. Boushell, C.T. Hung, E.B. Hunziker, E.J. Strauss, H.H. Lu, Current strategies for integrative cartilage repair, *Connect. Tissue. Res.* 58(5) (2017) 393-406.
- [144] A.J. Sophia Fox, A. Bedi, S.A. Rodeo, The basic science of articular cartilage: structure, composition, and function, *Sports Health* 1(6) (2009) 461-8.
- [145] F. Han, F. Zhou, X. Yang, J. Zhao, Y. Zhao, X. Yuan, A pilot study of conically graded chitosan-gelatin hydrogel/PLGA scaffold with dual-delivery of TGF-beta1 and BMP-2 for regeneration of cartilage-bone interface, *J. Biomed. Mater. Res., Part B* 103(7) (2015) 1344-53.

- [146] S.M. Goldman, G.A. Barabino, Spatial Engineering of Osteochondral Tissue Constructs Through Microfluidically Directed Differentiation of Mesenchymal Stem Cells, *Biores. Open. Access.* 5(1) (2016) 109-17.
- [147] H. Lin, T.P. Lozito, P.G. Alexander, R. Gottardi, R.S. Tuan, Stem cell-based microphysiological osteochondral system to model tissue response to interleukin-1beta, *Mol. Pharm.* 11(7) (2014) 2203-12.
- [148] A.E. Erickson, J. Sun, S.K. Lan Levengood, S. Swanson, F.C. Chang, C.T. Tsao, M. Zhang, Chitosan-based composite bilayer scaffold as an in vitro osteochondral defect regeneration model, *Biomed. Microdevices* 21(2) (2019) 34.
- [149] J. Radhakrishnan, A. Manigandan, P. Chinnaswamy, A. Subramanian, S. Sethuraman, Gradient nano-engineered in situ forming composite hydrogel for osteochondral regeneration, *Biomaterials* 162 (2018) 82-98.
- [150] L.P. Yan, J. Silva-Correia, M.B. Oliveira, C. Vilela, H. Pereira, R.A. Sousa, J.F. Mano, A.L. Oliveira, J.M. Oliveira, R.L. Reis, Bilayered silk/silk-nanoCaP scaffolds for osteochondral tissue engineering: In vitro and in vivo assessment of biological performance, *Acta Biomater.* 12 (2015) 227-241.
- [151] Z. Li, S. Jia, Z. Xiong, Q. Long, S. Yan, F. Hao, J. Liu, Z. Yuan, 3D-printed scaffolds with calcified layer for osteochondral tissue engineering, *J. Biosci. Bioeng.* 126(3) (2018) 389-396.
- [152] H.V. Almeida, B.N. Sathy, I. Dudurych, C.T. Buckley, F.J. O'Brien, D.J. Kelly, Anisotropic Shape-Memory Alginate Scaffolds Functionalized with Either Type I or Type II Collagen for Cartilage Tissue Engineering, *Tissue Eng., Part A* 23(1-2) (2017) 55-68.

- [153] H. Xiao, W. Huang, K. Xiong, S. Ruan, C. Yuan, G. Mo, R. Tian, S. Zhou, R. She, P. Ye, B. Liu, J. Deng, Osteochondral repair using scaffolds with gradient pore sizes constructed with silk fibroin, chitosan, and nano-hydroxyapatite, *Int. J. Nanomed.* 14 (2019) 2011-2027.
- [154] M.J. Oudin, O. Jonas, T. Kosciuk, L.C. Broye, B.C. Guido, J. Wyckoff, D. Riquelme, J.M. Lamar, S.B. Asokan, C. Whittaker, D. Ma, R. Langer, M.J. Cima, K.B. Wisinski, R.O. Hynes, D.A. Lauffenburger, P.J. Keely, J.E. Bear, F.B. Gertler, Tumor Cell-Driven Extracellular Matrix Remodeling Drives Haptotaxis during Metastatic Progression, *Cancer Discov.* 6(5) (2016) 516-31.
- [155] S.P. Carey, Z.E. Goldblatt, K.E. Martin, B. Romero, R.M. Williams, C.A. Reinhart-King, Local extracellular matrix alignment directs cellular protrusion dynamics and migration through Rac1 and FAK, *Integr. Biol.* 8(8) (2016) 821-35.
- [156] J. Park, D.H. Kim, H.N. Kim, C.J. Wang, M.K. Kwak, E. Hur, K.Y. Suh, S.S. An, A. Levchenko, Directed migration of cancer cells guided by the graded texture of the underlying matrix, *Nat. Mater.* 15(7) (2016) 792-801.
- [157] B.J. DuChes, A.D. Doyle, E.K. Dimitriadis, K.M. Yamada, Durotaxis by Human Cancer Cells, *Biophys. J.* 116(4) (2019) 670-683.
- [158] D.M. Lewis, K.M. Park, V. Tang, Y. Xu, K. Pak, T.S. Eisinger-Mathason, M.C. Simon, S. Gerecht, Intratumoral oxygen gradients mediate sarcoma cell invasion, *Proc. Natl. Acad. Sci. U. S. A.* 113(33) (2016) 9292-7.
- [159] D. An, K. Kim, J. Kim, Microfluidic System Based High Throughput Drug Screening System for Curcumin/TRAIL Combinational Chemotherapy in Human Prostate Cancer PC3 Cells, *Biomol. Ther.* 22(4) (2014) 355-62.

- [160] Z.H. Wang, Z.X. Liu, L.L. Li, Q.L. Liang, Investigation into the hypoxia-dependent cytotoxicity of anticancer drugs under oxygen gradient in a microfluidic device, *Microfluid Nanofluid* 19(6) (2015) 1271-1279.
- [161] T. Mulholland, M. McAllister, S. Patek, D. Flint, M. Underwood, A. Sim, J. Edwards, M. Zagnoni, Drug screening of biopsy-derived spheroids using a self-generated microfluidic concentration gradient, *Sci. Rep.* 8(1) (2018) 14672.
- [162] Y. Ma, Y. Ji, G. Huang, K. Ling, X. Zhang, F. Xu, Bioprinting 3D cell-laden hydrogel microarray for screening human periodontal ligament stem cell response to extracellular matrix, *Biofabrication* 7(4) (2015) 044105.
- [163] R.M. Delaine-Smith, G.C. Reilly, The effects of mechanical loading on mesenchymal stem cell differentiation and matrix production, *Vitam. Horm.* 87 (2011) 417-80.
- [164] V.L. Kolachala, O.A. Henriquez, S. Shams, J.S. Golub, Y.T. Kim, H. Laroui, E. Torres-Gonzalez, K.L. Brigham, M. Rojas, R.V. Bellamkonda, M.M. Johns, Slow-release nanoparticle-encapsulated delivery system for laryngeal injection, *Laryngoscope* 120(5) (2010) 988-94.
- [165] N. Kamaly, B. Yameen, J. Wu, O.C. Farokhzad, Degradable Controlled-Release Polymers and Polymeric Nanoparticles: Mechanisms of Controlling Drug Release, *Chem. Rev.* 116(4) (2016) 2602-63.

Chapter 3: Multisized Photoannealable Microgels Regulate Cell Spreading, Aggregation, and Macrophage Phenotype through Microporous Void Space

3.1 Introduction

Tunable scaffolds that direct cell fate are desirable in many tissue engineering applications such as wound healing, organoid systems, and drug delivery.^[1,2] As our understanding of tissue complexity increases, so does the demand for heterogeneous biomaterials.^[3] Microgels are an emerging tool that fulfill this role given their modularity, injectability, and range of fabrication techniques.^[4-6] Microgels have been harnessed to study cell behavior in response to stiffness, degradability, and biochemical cues.^[4,7-9] These granular hydrogels can be synthesized with a variety of polymers including alginate, poly(ethylene) glycol (PEG), and hyaluronic acid.^[4,10] Given the array of materials and tunability, microgels can be synthesized to meet a variety of scaffold specifications.

Polymeric scaffolds are frequently bulk hydrogels possessing a nanoporous mesh size that impedes cell infiltration, migration, and hinders biological activity.^[11] As a result, the inclusion of a hydrolytic or matrix metalloproteinase (MMP)-sensitive crosslinker is often used to enable cells to degrade and remodel their surrounding

Published as: J.M. Lowen, G.C. Bond, K.H. Griffin, N.K. Shimamoto., V.L. Thai, and J.K. Leach, Multisized Photoannealable Microgels Regulate Cell Spreading, Aggregation, and Macrophage Phenotype through Microporous Void Space, *Adv. Healthcare Mater.* 2023, 2202239.

environment.^[12] Cells will secrete MMPs in response to environmental stimuli, such as macrophages that secrete MMP-9 in response to infection.^[13]

Unlike bulk hydrogels, microparticle-based scaffolds possess tunable void space which inherently exists between the particles. Such void space permits cells to migrate and proliferate readily without first remodeling their surrounding environment. For example, human dermal fibroblasts proliferated two-fold more in a microgel scaffold compared to a bulk hydrogel scaffold.^[14] However, many techniques of microgel assembly have several primary drawbacks. The use of enzymatic catalysis to anneal microgels can take up to 90 minutes.^[10] Enzymatic catalysis may also require the use of costly reagents such as Factor XIII.^[7,14] Furthermore, there is a limited understanding for how microgel diameter affects void space and cell behavior. While the effects of pore size on cell penetration and proliferation have been well studied in bulk hydrogels, it has yet to be thoroughly investigated in a microgel platform.^[15,16]

Many microgel platforms rely on chemical assembly methods such as enzymatic catalysis^[7,14,17] or click chemistry^[18,19]. While UV photoannealing has been utilized previously for microgels,^[20] previous studies with PEG-vinyl sulfone microgels show a storage modulus reaching a peak of 578 Pa.^[6] Herein, we demonstrate an ultraviolet (UV) method of annealing microgels that enables broad control over substrate mechanical properties. This method is effective to anneal microgels with a range of diameters and requires as little as one minute for annealing. The combination of annealing solution, photoinitiator, and stoichiometric control permit our scaffolds to reach a storage modulus of over 2 kPa. Our annealing method adds to the list of tools available in the rapidly

growing microgel field, and our cell studies offer insight to how different cell types interact with our unique microgel sizes and chemistry.

We employ the ability to readily alter porosity in photoanneable microgel scaffolds to influence macrophage polarization, alter cell spreading and aggregation, and influence cell function. We generate microgels with compressive moduli ranging from ~ 10-80 kPa, which demonstrates their ability to match a range of tissue stiffnesses.^[21] We further show the compressive modulus and bioactivity of the microgels remain constant after cryopreservation at -20°C, which facilitates high-throughput production, storage, off-the-shelf availability, and expands their potential for clinical translation. Finally, we interrogate how microgel diameter influences cell invasion upon implantation. The ease of loading cells, cryopreservability, and short annealing time make this a promising platform for translation to the clinic.

3.2 Materials and Methods

3.2.1 Device Fabrication

Microfluidic master molds were created on silicon wafers (University Wafer) for devices first described in Rutte et al.^[14] We used a two-layer photolithography process with SU-8 10 and SU-8 100 (Kayaku Advanced Materials) to create channels heights to produce microgels of different diameters. The layers were aligned utilizing a EVG 620-mask aligner, and we used a Bruker Dektak XT to verify the heights of our device channels. A nozzle channel height of 12 μm and 38 μm created droplets of ~48 μm and 146 μm , respectively. We then poured polydimethylsiloxane (PDMS) (Ellsworth Adhesives, Sylgard 184) over our silicon master molds with the base and crosslinker

mixed at a 10:1 mass ratio. The PDMS mixture was desiccated and cured at 65°C for at least 1 hr and cut out. PDMS devices and glass slides were plasma cleaned and bonded together followed by a bake of 125°C on a hotplate for 1 hr. The microgel devices were then treated with Aquapel and Novec 7500 Oil (3M) to render the devices hydrophobic and fluorophilic, respectively.

3.2.2 Microgel fabrication

The microgel device contains a continuous oil phase and a dispersed aqueous phase. For large microgels, the oil phase consisted of Novec 7500 Oil and 0.75 wt% Picosurf (Sphere Fluidics). Picosurf concentration was increased to 2 wt% for the small microgels. The aqueous phase consisted of 8-arm PEG-VS (JenKem) in 0.15 M triethanolamine (TEOA, pH 5.1, Sigma) buffer and 3.5 kDa PEG-DT (JenKem). The solutions were injected into the microfluidic device using syringe pumps (NE-1000 and KD Scientific), with the continuous phase set at twice the flow rate of the dispersed phase. We utilized flow rates of 60/30 $\mu\text{L min}^{-1}$ for the large microgels and 30/15 $\mu\text{L min}^{-1}$ for the small microgels. After exiting the device, microgels were combined with a solution of 1% v/v triethylamine (TEA, Sigma) in Novec 7500 Oil using a Y-junction (IDEX Health and Science) and left at room temperature overnight to ensure complete crosslinking.

3.2.3 Microgel cleaning

Excess oil was first removed by pipetting. The emulsion was broken by adding a solution of 20 wt% 1H,1H,2H,2H-Perfluoro-1-octanol (Sigma) in Novec 7500 Oil approximately equal to the volume of remaining microgels. Microgels were swelled and

dispersed by adding HEPES buffer (25 mM, pH 7.4). The remaining oil was removed by washing in hexane 3x. For cell experiments, the microgels were then sterilized by washing 3x with 70% isopropyl alcohol. Finally, the microgels were washed with sterile HEPES buffer 3x where they were kept until use.

3.2.4 Microgel annealing

Microgels were first pelleted and then resuspended in 5mM PEG-DT in HEPES containing 0.4% VA-086 photoinitiator (FUJIFILM) equal to the volume of microgels. After incubating for 1 min, the microgels were spun down for 3 min at 3000xg for the small microgels and 15,000xg for the large microgels. The supernatant was then removed and microgels plated in the desired mold utilizing a positive displacement pipette (Gilson). The microgel slurry was then exposed to UV light (20 mW cm⁻², 320-500 nm, Omnicure S2000) for 2 min to form annealed scaffolds.

3.2.5 Annealing optimization studies

Microgels of 6% PEG-VS were created such that 50, 60, and 70% of the PEG-VS arms were crosslinked with PEG-DT. Microgels with fewer crosslinked arms did not maintain their shape, while microgels with more crosslinked arms did not anneal sufficiently. Microgels were then soaked in a solution containing 0.4% photoinitiator in HEPES, HEPES + 10 mM PEG-DT, HEPES + 0.1 v/v% NVP (Sigma), or HEPES + 10 mM PEG-DT + 0.1 v/v% NVP. Microgel scaffolds were formed as detailed previously and mechanical testing was performed as described below.

3.2.6 Formation of large microgel constructs

We first poured PDMS into a petri dish until it was 1 cm tall. After curing, we created an 8 mm x 1 cm cylindrical mold in the PDMS using an 8 mm biopsy punch. Microgels were then pipetted and annealed as described above.

3.2.7 Bulk hydrogel fabrication

Separate solutions of PEG-VS dissolved in diH₂O (pH = 5.5) and PEG-DT dissolved in diH₂O (pH = 8.5) were prepared at twice the concentration of their microgel counterparts. 50 μ L of each solution was pipetted into 8 mm x 1.5 mm cylindrical molds and mixed by pipetting up and down. After 10 minutes the gels were removed, put into a solution of HEPES (25 mM, pH = 7.4), and allowed to swell overnight.

3.2.8 Mechanical characterization

Bulk hydrogel scaffolds were measured using an Instron 3345 Compressive Testing System (Norwood, MA). Hydrogels were loaded between two flat platens and compressed at a rate of 0.05 mm/s. Moduli were calculated from the slope of stress versus strain plots limited to the linear first 10% of strain.^[22] Microgels were examined using a MicroTester (CellScale, Waterloo, ON). Individual microgels were loaded onto an anvil in a water bath filled with PBS. The microgels were then compressed half their diameter by a stainless-steel platen attached to a tungsten rod over 30 s. Displacement and force was tracked *via* MicroTester software. The linear region of the compressive modulus vs nominal strain graph was recorded as the calculated modulus.^[23] Storage modulus of microgel scaffolds over time was measured using a Discovery HR2

Rheometer (TA Instruments, New Castle, DE) with a stainless steel, cross hatched, 8 mm plate geometry. For our experimental group, the scaffolds were exposed to UV light after 30 s, while it remained off the entire time for our control group. A custom oscillatory time sweep (1% strain, 1 rad/s angular frequency) was performed using an initial 0.03N normal force.

3.2.9 Verification of peptide conjugation

We added 2 mM fluorescently tagged HAVDI (FITC-HAVDIGGGC, WatsonBio) to our microgels which crosslinked to some of the PEG-VS arms during synthesis *via* Michael Addition. Microgels were immediately imaged upon synthesis as well as 3 days post-synthesis and washing.

3.2.10 Cell culture

Human endothelial colony forming cells (ECFCs) were isolated and derived from human cord blood obtained through the UC Davis Cord Blood Collection Program (UCBCP). ECFCs were expanded in EGM-2 supplemented media (PromoCell, Heidelberg, Germany) with gentamicin (50 $\mu\text{g mL}^{-1}$; ThermoFisher, Waltham, MA) and amphotericin B (50 ng mL^{-1} ; ThermoFisher) under standard culture conditions (37°C, 5% CO_2 , 21% O_2) until use at passages 7-8. Media changes were performed every 2 days. Human bone marrow-derived MSCs (RoosterBio) from a single donor (21-year-old male) were expanded in growth medium (GM) consisting of minimum essential alpha medium (α -MEM; Invitrogen) supplemented with 10% fetal bovine serum (FBS; Genesee) and 1% penicillin/streptomycin (Gemini Bio-Products, Sacramento, CA). MSCs were cultured

under standard conditions until use at passage 4. Media changes were performed every 2–3 days.

3.2.11 Influence of cryostorage on microgels

We fabricated 6% PEG-VS large diameter microgels with 1 mM RGD (Ac-RGDSPGERCG-NH₂, Genscript). Microgels were frozen for up to one month at -20°C, with batches being removed, thawed, and analyzed at designated time points. Mechanical testing was performed on the MicroTester as described above. After 1 week in storage, microgels were seeded with human MSCs (RoosterBio) at 5 million cells mL⁻¹ and compared to fresh microgels when maintained in complete medium for 48 hr. Metabolic activity of seeded MSCs was determined by alamarBlue assay (Thermo Fisher). The cell actin cytoskeleton was stained with Alexa Fluor 488 Phalloidin solution (Thermo Fisher; 1:400 in PBS), and cell nuclei were stained with DAPI (Thermo Fisher; 1:500 in PBS). Z-stacks were taken on a confocal microscope (Leica Stellaris 5), and max projections used to illustrate cell morphology through the scaffolds.

3.2.12 Modeling of void space

A custom MATLAB code was created to measure microgel diameters and model annealing. Annealed scaffolds were imaged *via* microscopy and ImageJ was used to measure the void space area between microgels.

3.2.13 Formation of cell aggregates within scaffolds

Small and large microgel scaffolds composed of 6% PEG-VS were seeded with MSCs at 5 million cells mL⁻¹. Images were acquired at 12, 24, and 48 hr with brightfield

microscopy (Nikon Eclipse TE2000U). Aggregates from large microgels were collected by pipetting the scaffolds up and down, followed by pipetting the solution through a 100 μm sieve. Aggregates were washed with PBS, stained with a live/dead assay per the manufacturer's protocol (Thermo Fisher), and fluorescent images taken using the Nikon Eclipse TE2000U. For confocal microscopy images, cells were stained and imaged with DAPI and phalloidin as described above. Aggregate size was measured in ImageJ using the line and measurement tools.

3.2.14 Assessment of spreading in scaffolds from co-culture spheroids

Heterotypic co-culture spheroids were formed with ECFCs and MSCs at a ratio of 1-to-2 using a forced aggregation method.^[24,25] Briefly, desired concentrations of ECFCs and MSCs were pipetted into 1.5% agarose molds in well plates, and the plates were centrifuged at 500xg for 8 min. Plates were maintained in static standard culture conditions (37°C, 5% CO₂, 21% O₂) for 48 hr to enable spheroid formation in 3:1 EGM-2: α -MEM. Each microwell in the agarose molds contained 15,000 cells. 4.5% PEG-VS microgels with 1 mM RGD were used for the large and small microgel scaffolds. Microgels were annealed as described above, with the microgel slurry being mixed with heterotypic spheroids before being plated in a 6 mm x 1.5 mm cylindrical silicon mold and exposed to UV light. Scaffolds were collected for analysis on Day 1 and Day 3, with media changed every other day using the 3:1 mixture of EGM-2: α -MEM. For confocal microscopy images, cells were stained and imaged with DAPI and phalloidin as described above. Metabolic activity of spheroids was determined by alamarBlue assay (Thermo Fisher). DNA content

was quantified using the PicoGreen Quant-iT Assay Kit (Invitrogen). Migration distance and cell density were quantified in ImageJ using the Li threshold.

3.2.15 Assessment of macrophage polarization as a function of microgel diameter

IC-21 murine macrophages (ATCC) were seeded at 4 million cells mL⁻¹ in small or large microgel scaffolds. To polarize macrophages toward an M1 phenotype, lipopolysaccharide (LPS, 0.3 ng mL⁻¹, Thermo Fisher) was added 48 hr before seeding and refreshed with basal media after 24 hr. Microgels were formed from 4.5% PEG-VS with 1 mM RGD prepolymer solution. Microgel and macrophage slurries were pipetted into 8 mm x 5 mm cylindrical molds before exposure to UV light. The gels were maintained in RPMI 1640 (ATCC) supplemented with 10% FBS. After 24 hr, gels were moved to a new plate with fresh media and maintained in culture for 6 days with media changes every day. For confocal microscopy, 8 mm x 1.5 mm scaffolds were prepared and imaged on the Leica Stellaris 5. Cells were recovered from annealed patties *via* digestion at 37°C with trypsin for 5 min and gentle mixing, followed by dilution with basal media. Solutions were filtered through a 30 µm sieve to create a single cell suspension, and macrophage polarization was characterized using flow cytometry (Attune NxT, Life Tech).

3.2.16 Flow cytometry

Following Fc γ receptor blocking (1:40, TruStain FcX, BioLegend), cells were stained with antibodies against F4/80 (1:50, eBioscience #MF48021), CD86 (1:160, eBioscience #47-0862-82) and CD206 (1:40, eBioscience #48-2061-82). Cellular viability was evaluated with fixable Zombie Aqua (1:250, Life Tech). Cells were then fixed with 2%

PFA, permeabilized with 0.1% Triton-X, and stained for intracellular markers, iNOS (1:500, eBioscience #12-5920-82) and Arginase-1 (1:500, eBioscience #53-3697-82), overnight at 4°C with gentle agitation. Macrophages with an M1 phenotype were characterized by F4/80+CD86+iNOS+ populations and M2 phenotypes by F4/80+CD206+ARG1+ populations. The frequency of each type of macrophage was quantified per microgel size. Polarization controls (data not shown) consisted of IC-21s seeded on TC wells in monolayer treated with basal media (M0), 200 ng/mL LPS (M1), and 20 ng/mL IL-4 (M2) for 24 hr. Cells were lifted with trypsin and gentle agitation. Cells were filtered and stained as described.

3.2.17 Subfascial Implants

Before implantation, 4.5% PEG-VS microgels with 1 mM RGD were loaded and annealed in PDMS molds. Treatment of experimental animals was in accordance with UC Davis animal care guidelines (IACUC protocol #22577; Animal Welfare Assurance #D16-00272) and all National Institutes of Health animal handling procedures. Male twelve-week-old C57BL/6 mice (Jackson Laboratories, West Sacramento, CA) were anesthetized and maintained under a 2% isoflurane/O₂ mixture delivered through a nose cone. Each animal received four subfascial implants: small microgels (upper and lower left) and large microgels (upper and lower right). Following a dorsal midline incision, fascia was incised, and blunt dissection was performed between the fascia and muscle belly. Annealed microgels in PDMS molds were placed face-down on the muscle and sutured in place with 4-0 Monocryl sutures (Ethicon, Cornelia, GA). Animals were euthanized after 2 weeks, and gels were collected, removed from PDMS, and fixed in 4% PFA overnight

at 4°C. Samples were then washed twice in PBS, paraffin-embedded, and sectioned at 7 µm. Sections were stained with hematoxylin (Thermo) and eosin (Ricca) (H&E) or Masson's trichrome (Sigma) and imaged using an EVOS XL Core (Invitrogen). For immunohistochemistry staining, slides were rehydrated and exposed to heat mediated antigen retrieval with a sodium citrate buffer. iNOS-stained slides were permeabilized with 0.1% Triton-X100 (Sigma) for 10 min at room temperature. Samples were then incubated in blocking buffer consisting of 10% goat serum and 10 mg mL⁻¹ Bovine Serum Albumin (BSA) for 1 hr at room temperature. Slides were incubated with anti-iNOS antibody (Abcam, ab3523) at a concentration of 1:150 overnight at 4°C. CD206-stained slides were incubated with anti-CD206 antibody (Abcam, ab64693) at a concentration of 1:150 overnight at 4°C. Slides were then treated with a secondary goat anti-rabbit antibody conjugated to Alexa fluor 647 (Abcam, ab150083) at a concentration of 1:200 for 1 hr at room temperature. Slides were counterstained with DAPI (Thermo). Large tile scans were taken at 40x using confocal microscopy (Leica Stellaris 5). Positive signal was quantified in ImageJ after thresholding with RenyiEntropy. The area positive for iNOS or CD206 was normalized to area of DAPI.

3.2.18 Statistical Analysis

All statistics were calculated using GraphPad Prism 9. Statistical significance was assessed by either one-way ANOVA, two-way ANOVA with Tukey's multiple comparisons test, two-way ANOVA with Sidak's multiple comparisons test, or Student's t-test when appropriate. *p*-values <0.05 were considered statistically significant.

3.3 Results and Discussion

3.3.1 Synthesis and annealing of microgels

Microgels were synthesized using a previously established high-throughput microfluidic device capable of producing up to 30 mL h⁻¹ (**Figure 3.3.S1**, Supporting Information).^[14] We fabricated devices with different channel heights to produce microgels of different diameters. The use of an 8-arm PEG-vinyl sulfone (PEG-VS) allows us to fine tune the number of arms used for crosslinking while leaving arms available for biofunctionalization with peptides. To facilitate microgel annealing, we crosslinked a fraction of the arms and kept the remaining free arms available for photoannealing (**Figure 3.1A**). We stoichiometrically controlled the number of free arms by altering the ratio of 8-arm PEG-VS to the crosslinker PEG-dithiol (PEG-DT). By using the vinyl sulfone moiety for both microgel crosslinking and annealing, we avoid the use of additional complex or costly reagents required for enzymatic catalysis or host-guest interactions.^[26,27]

To anneal the microgels, we added our annealing solution of PEG-DT in HEPES with photoinitiator (**Figure 3.1B**). The microgels were then spun down and supernatant removed. For larger microgels, a higher centripetal force is required to effectively jam the microgels due to the increased void space between them. The aggregated microgels may be mixed with cells or other additives, as the microgels exhibit shear thinning behavior and can easily be manipulated. The microgel slurry was plated and exposed to UV light to finish the annealing process. To determine necessary time for annealing, we measured the storage modulus of microgel slurries during UV exposure (**Figure 3.1C**). We found UV exposure at 20 mW cm⁻² for 1 minute significantly increased storage modulus, while

2 minutes resulted in a stronger annealing response. The increase in storage modulus in the control group without UV light can be attributed to slight annealing of the microgels through Michael Addition. This could be modulated by changing the pH of the annealing solution. Our approach is advantageous compared to other methods that may require hours for assembly.^[26,28] Furthermore, the capacity to anneal microgels at room temperature with only a UV light source increases clinical accessibility. This strategy is amenable to the use of other photoinitiators sensitive to different wavelengths such as those found in the visible light spectrum (e.g., eosin Y).^[17]

We created microgels with 50, 60, and 70% of the arms crosslinked to determine how many of the VS groups to leave for annealing. We tested the compressive moduli of scaffolds made from these microgels to observe how strongly they were annealed. We also tested the addition of N-vinyl-2-pyrrolidone (NVP), which has been reported to increase gelation of PEG-VS by increasing the diffusion of free radicals.^[29,30] We found the addition of PEG-DT necessary to promote annealing, while the inclusion of NVP increased the annealing strength across all groups (**Figure 3.1D**). Microgels with 60% of the arms crosslinked before annealing resulted in the highest compressive modulus. We hypothesize this is due to crosslinking a sufficient fraction of arms to increase the compressive moduli of a microgel while leaving enough arms free to anneal neighboring microgels. Based on these results, the remainder of our studies utilized microgels with 60% of the PEG-VS arms crosslinked. We also tested several concentrations of PEG-DT in our annealing solution, with a 4.8 mM concentration theoretically being the maximum concentration needed to fully crosslink the remaining PEG-VS arms in 3% w/v PEG-VS microgels (**Figure 3.1E**). While 2 mM resulted in a large portion of the microgels

dissociating from the scaffold, 5 mM and 10 mM PEG-DT resulted in similar amounts of dissociation, indicating the vinyl sulfone groups were fully saturated with 5 mM. This indicates the annealing reaction is efficient enough to not require excess PEG-DT beyond that needed to crosslink the remaining arms. As a result, we utilized solutions of PEG-DT with a concentration matching the concentration of free arms for annealing in further experiments.

Finally, we verified that we could create microgel scaffolds that were of clinically relevant dimensions (**Figure 3.S2**, Supporting Information). We fabricated microgel scaffolds that were up to 1 cm in thickness, confirming the microgels do not significantly attenuate UV light in large scaffolds. Furthermore, the 1 cm thick photoannealed microgel scaffold withstood cyclically applied compression, demonstrating the strength of the annealed scaffold (**Video S1**, Supporting Information). This approach was designed to minimize the steps needed for scaffold formation. By stoichiometrically controlling the number of arms used for crosslinking and annealing, we minimize the number of reagents needed to form an annealed microgel scaffold.

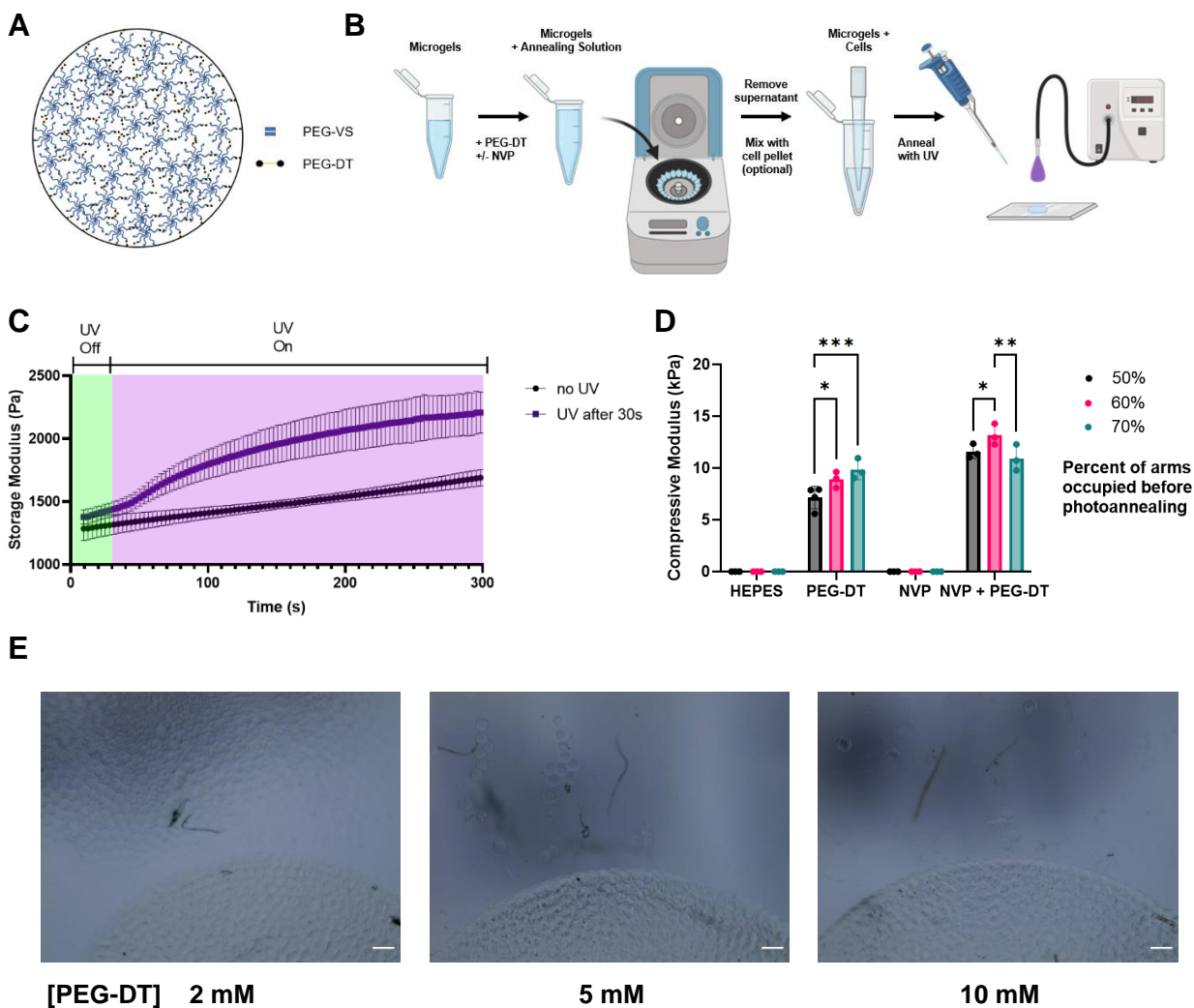


Figure 3.1 Annealing PEG-VS microgels. **(A)** The ratio of PEG-VS to PEG-DT can be stoichiometrically controlled so that arms are left free for annealing. **(B)** Microgels are soaked in an annealing solution containing PEG-DT before being spun down and supernatant aspirated. The microgel slurry is then deposited in the desired location and exposed to UV light for 2 minutes to anneal. **(C)** Storage modulus of microgel scaffolds increases over time when exposed to UV light. **(D)** The annealing solution containing NVP and PEG-DT produced the strongest annealed scaffold. **(E)** A comparison of different PEG-DT concentrations in the annealing solution. A 5 mM solution was sufficient for

maximum annealing. Scale bar represents 200 μm . Statistics: two-way ANOVA, Tukey's multiple comparisons test. $n \geq 4$. * $p < 0.05$, ** $p < 0.01$, and *** $p < 0.001$

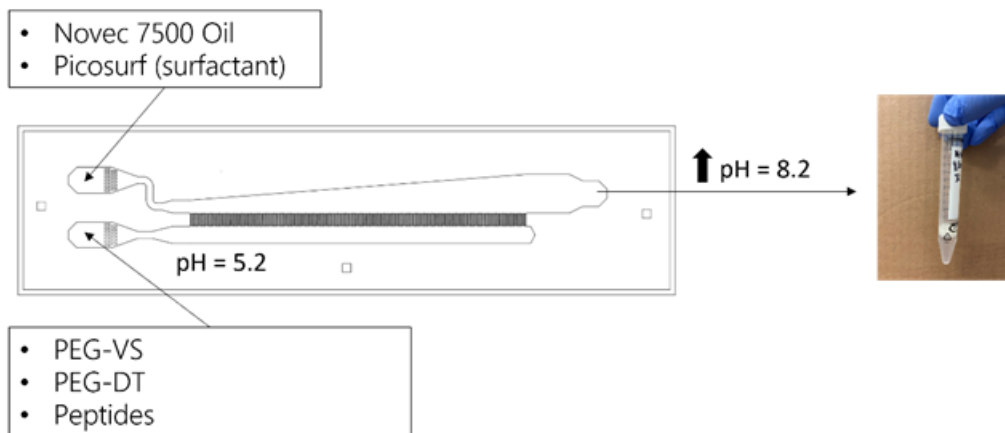


Figure 3.S1 Schematic of microfluidic device used for microgel synthesis. The device consists of an oil channel (contains Novec 7500 and Picosurf) and an aqueous channel (contains PEG-VS, PEG-DT, and peptides). The aqueous channel flows up to the oil channel through hundreds of small perpendicular channels where the aqueous solution is pinched off into droplets. The pH is then raised downstream crosslinking the microgels via Michael Addition.

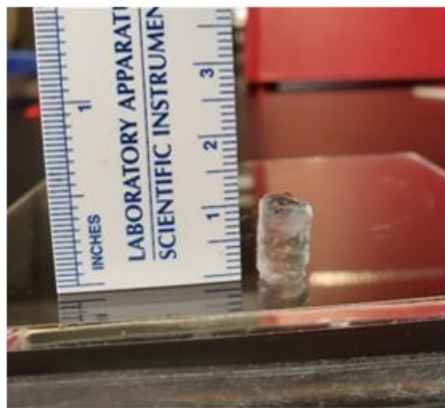


Figure 3.S2 Constructs over 1 cm in thickness were annealed using UV light.

3.3.2 Mechanical properties and assessing potential for microgel cryopreservation

The design and application of microgels requires an accurate understanding of their mechanical properties. Scaffolds are commonly engineered to match the mechanical moduli of the target tissue.^[31] There is a lack of research on how the microscale properties of a material compare to the macroscopic properties of its bulk counterpart. We utilized a MicroTester to test the compressive modulus of individual microgels (**Figure 3.2A**). This device allowed us to measure the mechanical modulus of individual microgels by measuring force and displacement of the microgel (**Video S2**, Supporting Information).

We compared the mechanical properties of our individual microgels to conventional PEG-VS bulk gels (**Figure 3.2B**). As expected, all groups followed a similar trend of increased compressive modulus with increased concentration of PEG-VS. We generated microgels with stiffnesses ranging from ~10 – 82 kPa with macromer concentrations of 3% and 12%, respectively. A larger range of mechanical properties could be generated by lowering or raising the macromer concentration. The moduli of the individual microgels were higher than their respective bulk gels in the 9% and 12% conditions. This could be due to the difference in testing methods, as microgels were tested on a MicroTester and the bulk gels were tested on an Instron. Alternatively, this could be due to individual microgels being more homogeneous than their bulk counterparts, which often may not be uniformly smooth or crosslinked. The slight heterogeneity of bulk gels may yield a softer modulus. We also compared the moduli of microgels made from 10 kDa versus 20 kDa PEG-VS. The 10 kDa microgels trended toward a higher

modulus due to the monomers having shorter arms which results in closer packing (**Figure 3.2C**). We selected the 10 kDa PEG-VS for the remainder of our studies due to the capacity to fabricate microgels with a larger range of stiffness.

The ability of the microgels to be cryopreserved is important for long-term storage, production in a high-throughput manner, and for clinical application. Recently, microgels have been cryopreserved in the pursuit of reproducible particle size after rehydration.^[32] We performed mechanical testing on 6% PEG-VS microgels frozen at -20°C for up to a month and observed no change in mechanical properties when tested upon thawing (**Figure 3.2D**). We also assessed the ability of RGD-functionalized microgels to remain bioactive after cryostorage. Peptides can be utilized to influence cell behavior such as attachment or differentiation.^[33] We verified that we could functionalize our microgels using fluorescent peptides. The fluorescent peptide was clearly present on the microgels both upon synthesis and after 3 days (**Figure 3.2E**). These findings confirmed that washing and collection steps did not impede peptide attachment. We observed comparable cell spreading by human mesenchymal stromal cells (MSCs) in both frozen and freshly made microgels compared to unmodified microgels (**Figure 3.2F**). Interestingly, the cells in microgels without peptides formed cellular aggregates, most likely due to the lack of adhesive sites on the microgels and the cell-cell adhesion that occurred. Fresh and frozen microgels supported similar levels of cellular metabolic activity (**Figure 3.2G**).

By measuring the mechanical properties of the microgels and demonstrating their ability to be cryopreserved, we further illustrate their potential utility in the clinic. The large range of stiffnesses and ability to impart bioactivity via peptide incorporation enable these

microgels to be tailored for a variety of applications. The microgels demonstrate their ability to maintain a constant compressive modulus and peptide function after cryopreservation, opening the door for on-demand use in the clinic.

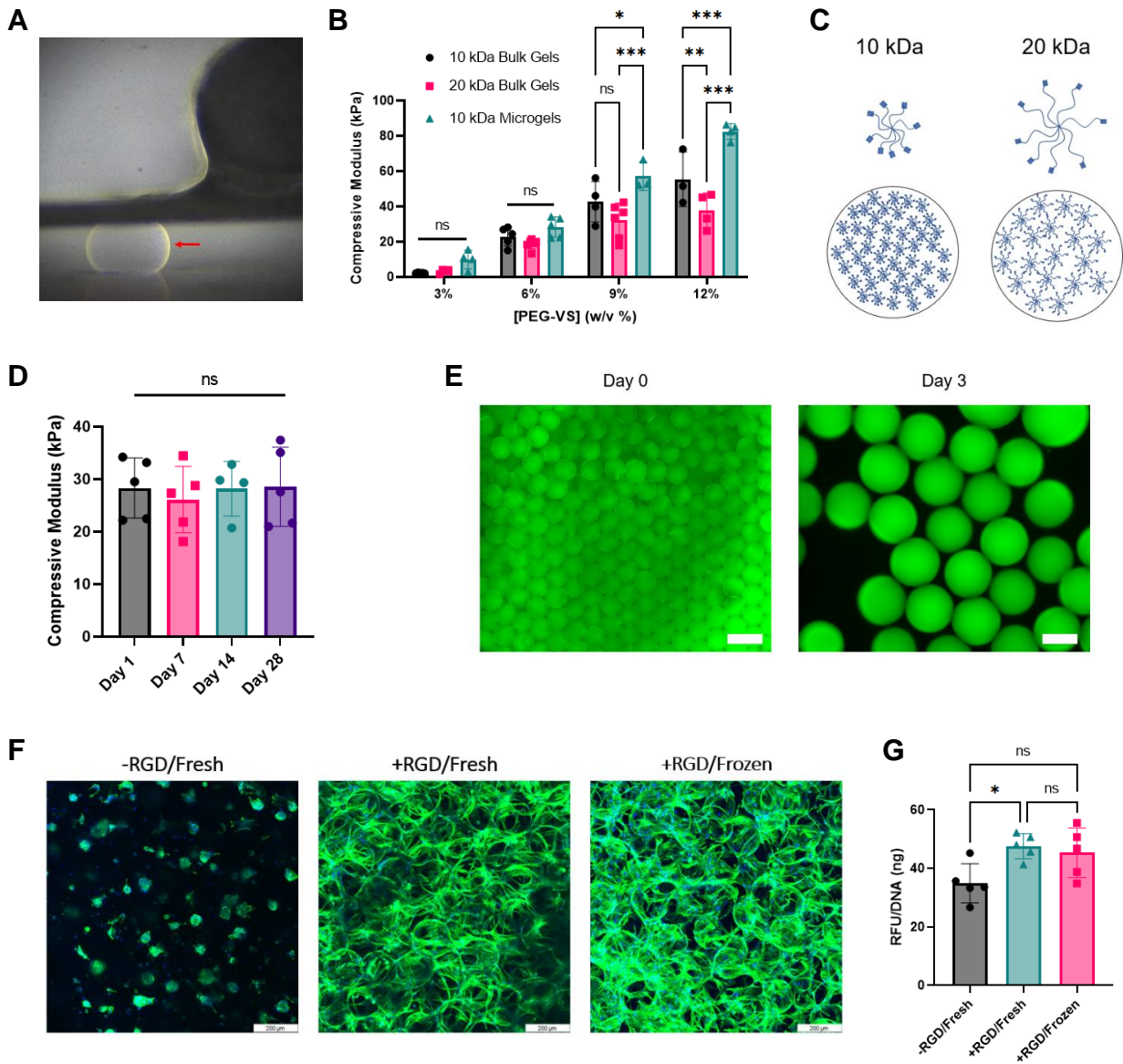


Figure 3.2 Mechanical testing and cryopreservation. **(A)** Large microgel (red arrow) compressed between the two plates of the MicroTester. **(B)** Compressive modulus of bulk gels versus microgels. **(C)** 10 kDa PEG-VS monomers pack closer together compared to

20 kDa monomers. **(D)** Compressive modulus of frozen microgels remains constant after thawing. **(E)** Addition of fluorescent peptide to verify successful peptide addition. Scale bar at Day 0 represents 500 μm . Scale bar at Day 3 represents 100 μm . **(F)** Cell spreading on frozen and fresh gels compared to rounded cells on negative control. Scale bar represents 200 μm . **(G)** alamarBlue assay confirms that fresh and frozen microgels support similar levels of bioactivity. Statistics: **(B)** Two-way ANOVA, Tukey's multiple comparisons test. **(D,G)** Ordinary one-way ANOVA, Tukey's multiple comparisons test. $n \geq 3$. * $p < 0.05$, ** $p < 0.01$, and *** $p < 0.001$

3.3.3 Modeling of void space in annealed microgels

The porosity of our microgel scaffolds is a strong predictor for how cells may migrate, aggregate, and differentiate within our constructs. Smaller diameter microgels will have less void space between them, and therefore, cells will be increasingly monodispersed with less room to spread. Conversely, larger diameter microgels will possess increased void space between them so cells will be able to more easily migrate and aggregate. Similarly, more polydisperse microgels will exhibit larger void space due to the microgels being unable to pack together in an optimal manner.

To simulate microgel packing, we used MATLAB to identify and measure the diameters of batches of large and small microgels (**Figure 3.3A**). Large microgels had an average diameter of $146.1 \pm 2.7 \mu\text{m}$, while small microgels had an average diameter of $47.9 \pm 4.1 \mu\text{m}$ (**Figure 3.3B**). The slightly larger standard deviation in the smaller microgels can be attributed to the increased surface area-to-volume ratio requiring more surfactant. We then imported the measured diameters into a custom MATLAB script

based on established code^[34] which will close pack the microgels and minimize the sum of distances between them (**Figure 3.3C**). The microgels will converge to hexagonal close packing (HCP) with greater monodispersity.

We used ImageJ to calculate the area of the void space between the microgels (**Figure 3.3D**). For the more monodisperse large microgels, much of the void space area is triangular due to convergence to HCP, while some larger theoretical areas are observable between the more polydisperse microgels. We used microscopy to measure the void space area in annealed scaffolds and found that the actual average void space between microgels was not significantly different from our predicted area (**Figure 3.3E**). Minor variance between the two could be attributed to the microgels slightly compressing or packing imperfectly. While actual diameters were used in the modeling, a list of theoretical diameters could be inputted to predict what other void spaces may result.

The ability to model void space is beneficial for many cell-based projects that vary greatly in the scale of biologics used. There are significant differences between cell types such as red blood cells and adipocytes which can range from 7.5 μm to over 100 μm in diameter, respectively.^[35,36] Aggregates of cells such as MSC spheroids can reach up to 600 μm without a hypoxic core.^[37] It is also useful for the incorporation of other additives such as drug-loaded nanoparticles.^[38] Overall, modeling is a powerful tool that can be utilized to fabricate microgels for a specific porosity to influence cell phenotype.

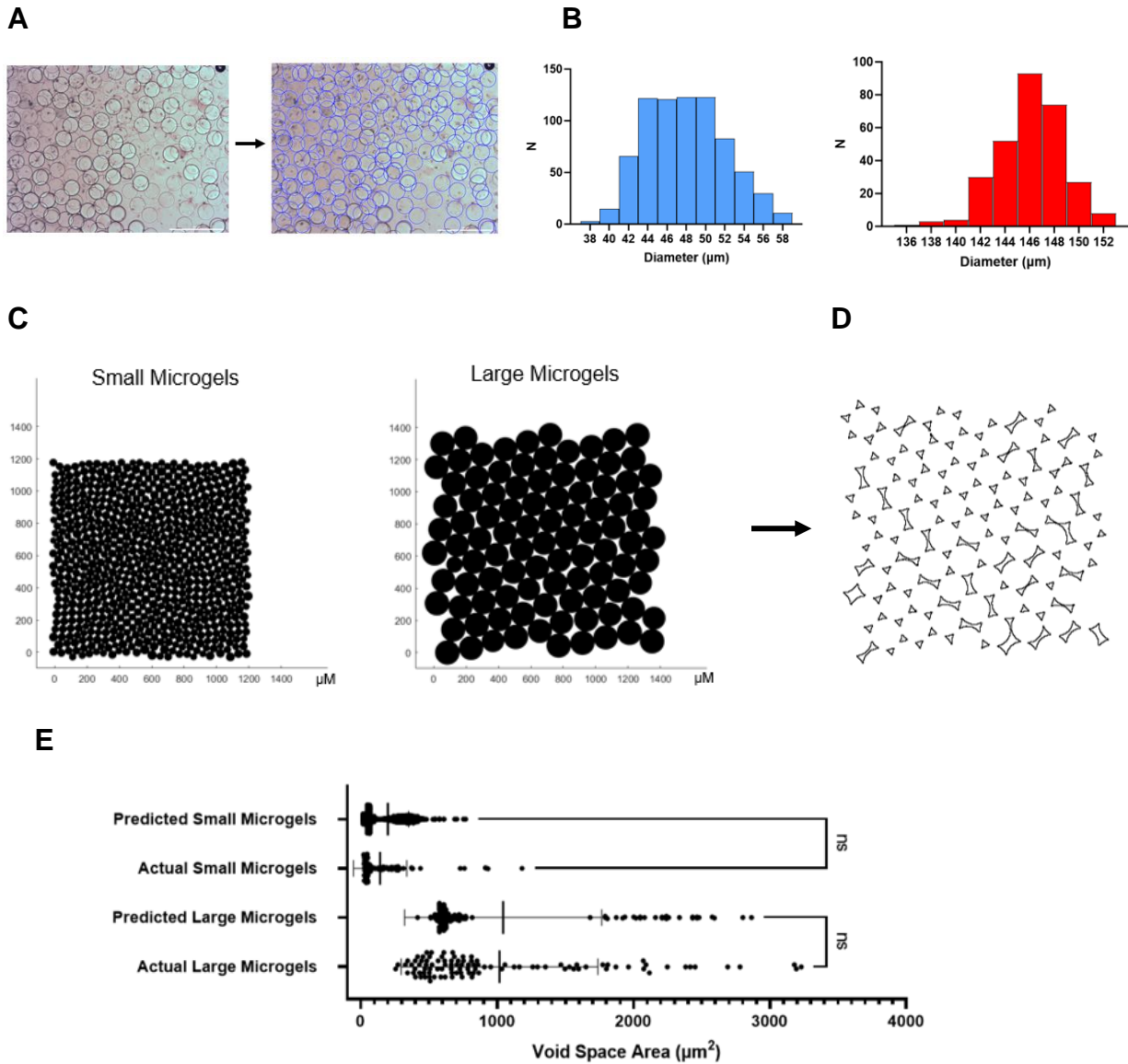


Figure 3.3 Modeling void space between microgels in annealed scaffolds. **(A)** Custom MATLAB code detects and measures microgel diameters. Scale bar represents 500 μm . **(B)** Histograms of small and large microgel diameters. **(C)** Modeling microgel annealing in MATLAB. **(D)** Measuring void space area in ImageJ. **(E)** Predicted void space area vs experimentally measured void space area. Statistics: Ordinary one-way ANOVA, Tukey's multiple comparisons test. $n \geq 100$. * $p < 0.05$, ** $p < 0.01$, and *** $p < 0.001$

3.3.4 Evaluation of annealed microgels to promote formation of cell aggregates

Multicellular spheroids can act as building blocks that capture complex aspects of *in vivo* environments and represent improved model systems to study development and disease. Spheroids exhibit increased viability along with enhanced proangiogenic, anti-inflammatory, and tissue-forming potential.^[39] Thus, the development of a platform that can promote the formation of cellular aggregates would be useful for many tissue engineering applications. To further investigate the impact of microgel size on cellular aggregate formation, we seeded monodisperse MSCs in small and large microgel scaffolds lacking adhesive motifs to encourage cell-cell adhesion and promote aggregate formation. We observed spheroid formation over the first 48 hours, which is a typical timeframe for spheroid formation using other methods such as hanging drop^[40] or formation in non-adhesive well plates.^[24,25]

Aggregate formation was visible in large diameter microgel scaffolds after 12 hours, with monodisperse cells still present throughout the scaffold. The average aggregate size was consistent over 48 hours. MSCs in small diameter microgels formed smaller aggregates after 12 hours with many cells remaining monodisperse (**Figure 3.4A**). We observed a trend towards a smaller aggregate diameter over 48 hours, which may be due to compaction of the aggregates.^[39] Quantification of average aggregate size over time illustrates how the void space in large microgel scaffolds promotes increased aggregate size compared to small microgel scaffolds (**Figure 3.4B**). The average aggregate diameters at 48 hours in the large and small microgel scaffolds were ~32.0 μm and 14.8 μm , respectively, which strongly correlates with the observed void space areas in **Figure 3.3E**.

Confocal microscopy of large diameter microgel scaffolds at 48 hours allowed us to clearly visualize aggregates through the scaffold (**Figure 3.4C**). While some cells remained monodisperse, the majority were contained in aggregates. We observed minimal cell spreading, possibly due to the deposition of extracellular matrix (ECM) by the MSCs. Furthermore, we were able to dissociate the microgels and retrieve viable cellular aggregates (**Figure 3.4D**). For this application, we weakly annealed the microgels by avoiding NVP in our annealing solution, which permitted dissociation by simple pipetting. This demonstrates the potential for microgels to be used as a spheroid formation platform, where spheroids can be formed and collected for use in another medium. However, the aggregates formed in this platform are significantly smaller compared to aggregates achievable *via* other methods such as hanging drop, which has resulted in aggregates over 1000 μm in diameter.^[40] While this platform may not be able to generate aggregates as large as established methods, it is feasible that larger microgels could yield larger aggregate formation as needed. A scaffold which promotes spheroid formation may eliminate the need to form spheroids *a priori*, which commonly requires a minimum of 48 hours.^[25] Given the correlation between our model of void space and aggregate size, it would be possible to design specific size microgels for formation of a desired spheroid size.

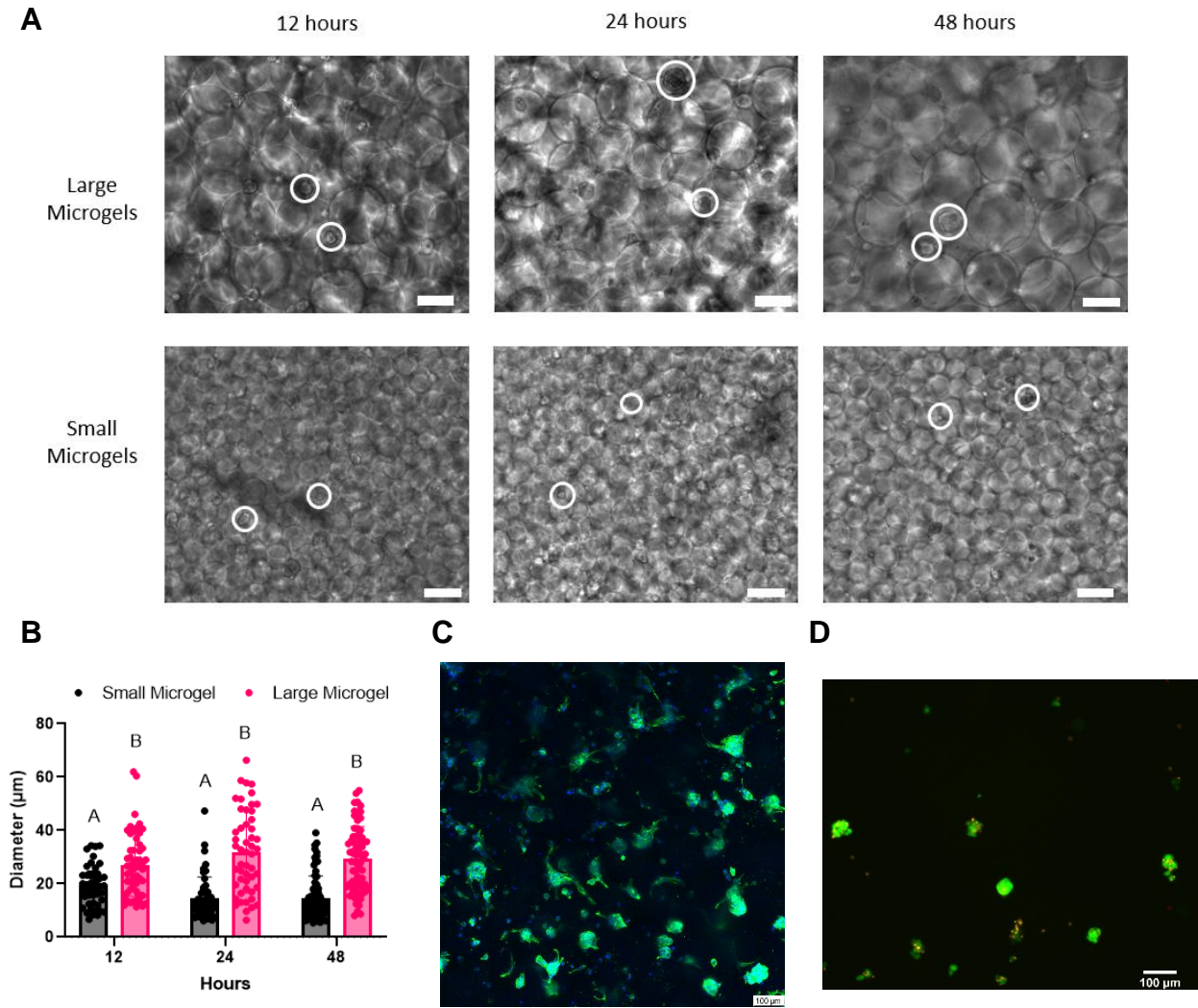


Figure 3.4 Microgels as an aggregate-forming platform. **(A)** MSC aggregate formation in large and small microgels over 48 hours. More monodisperse cells are seen in small microgels. MSCs circled in white. **(B)** Quantification of aggregate size demonstrates how larger aggregates form in large microgel scaffolds. **(C)** DAPI/Phalloidin stain reveals the formation of aggregates throughout the large microgel scaffold after 48 hours. **(D)** Live/dead stain of aggregates after retrieval from large microgel scaffolds. Scale bars represent 100 μm. Statistics: two-way ANOVA, Sidak's multiple comparisons test. $n \geq 46$. $p < 0.05$ was considered significant. Data points with different letters are significantly different from one another.

3.3.5 Effects of microgel diameter on cell proliferation and spreading

The void space between microgels allows for rapid cell infiltration and proliferation without cells needing to remodel the surrounding environment, as is required in bulk hydrogels.^[8] To assess how void space influences cell spreading, we seeded spheroids in scaffolds composed of large and small microgels. By seeding the microgels with spheroids, we can examine migration distance and density which is not possible if the cells were distributed throughout as monodisperse cells. Microgels increase MSC retention and proliferation compared to traditional nanoporous hydrogels.^[41] However, spheroid growth in our specific microgel sizes has not been reported. We hypothesized the increased surface area present in small microgel scaffolds would promote faster cell migration from the spheroid into the scaffold.

We seeded 15,000 cell spheroids composed of MSCs and endothelial cells at a 2:1 ratio in our microgel scaffolds, as we previously demonstrated this spheroid composition forms robust cellular networks.^[42] Microgels were modified with RGD to promote cell adhesion and migration. We assessed network formation and migration distance on Day 1 and Day 7 *via* confocal microscopy and stained cells with phalloidin and DAPI to visualize the actin cytoskeleton and nuclei, respectively (**Figure 3.5A**).

Both large and small microgels promoted rapid migration of cells into the scaffold. The leading edge of cell migration was comparable for both microgel sizes on Days 1 and 7 (**Figure 3.5B**). The greater porosity within large microgel scaffolds did not significantly hinder cell migration. However, the smaller diameter microgel scaffold resulted in a higher cell density on Days 1 and 7 (**Figure 3.5C**). This can be attributed to the higher surface area-to-volume ratio of the smaller microgels that provide more attachment sites for cell

spreading. Both scaffolds promoted similar levels of metabolic activity when normalized to DNA, indicating both formulations promote high viability (**Figure 3.5D**).

The rapid migration of cells in both conditions highlights the advantage of inherent porosity in microgel scaffolds. The measurable migration on Day 1 reflects the cells ability to immediately migrate without first remodeling the surrounding environment. While void space size is significantly smaller in small microgel scaffolds compared to large microgel scaffolds, it was sufficient to permit cell movement. Future work could utilize different size microgels to regulate the density of cell infiltration and spreading.

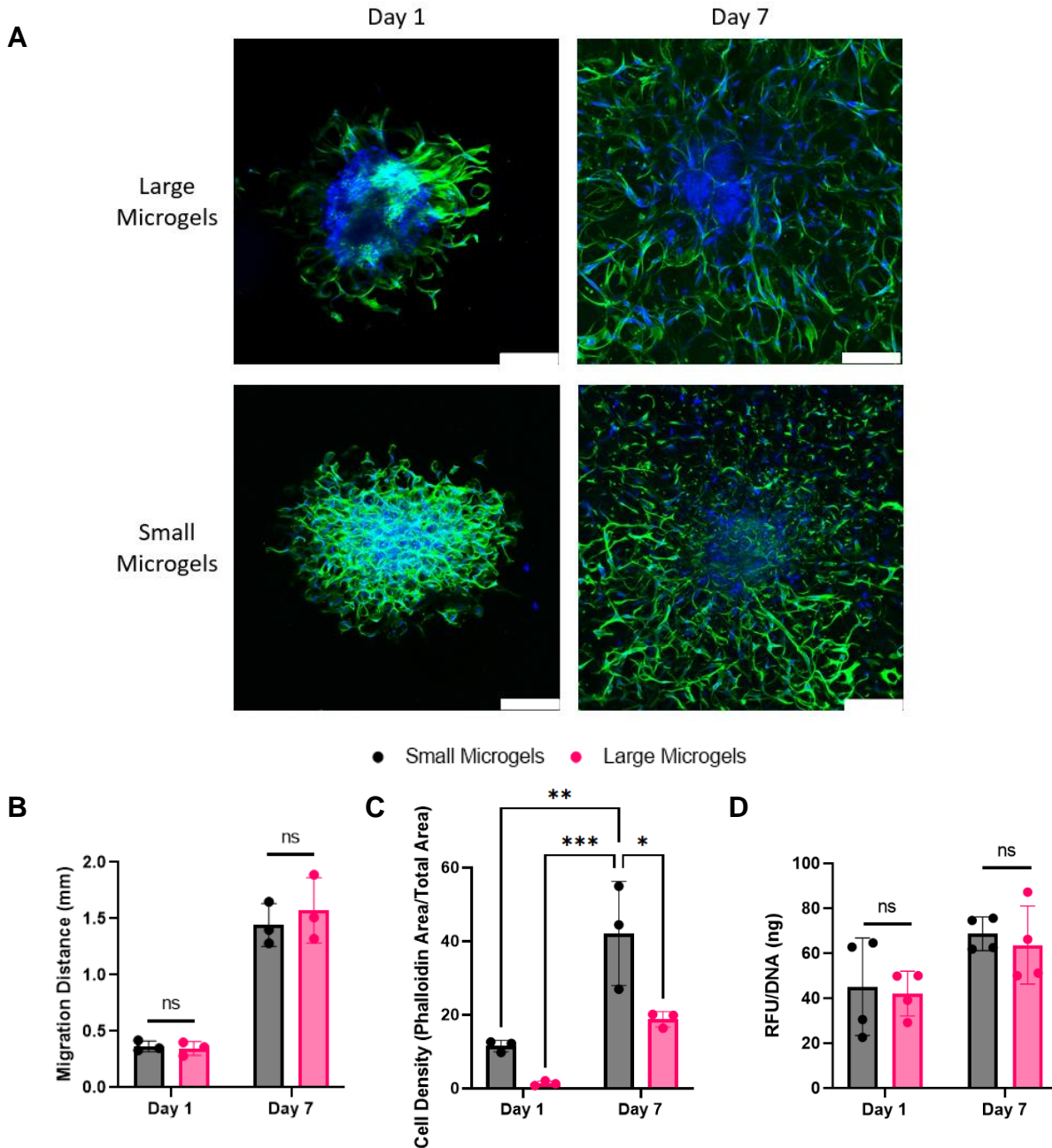


Figure 3.5 Spheroids spread rapidly in large and small microgel scaffolds. **(A)** DAPI/Phalloidin stains illustrate that void space inherent in microgel scaffolds facilitates rapid spreading in large and small microgel scaffolds. Scale bars represent 200 μm . **(B)** Migration distance did not differ between microgel scaffolds. **(C)** Cell spreading is denser in small microgel scaffolds versus large microgel scaffolds at Day 1 and Day 7. **(D)**

alamarBlue assay confirms that both scaffolds promote high cell metabolic activity. Statistics: Two-way ANOVA, Tukey's multiple comparisons test. $n \geq 3$. * $p < 0.05$, ** $p < 0.01$, and *** $p < 0.001$

3.3.6 Effects of microgel size on macrophage polarization

Solid biomaterial implants often induce a foreign body response, regulated by macrophages, that is characterized by poor vascularization and fibrosis.^[43] Ideally, a biomaterial will promote a pro-regenerative response characterized by cell infiltration and material integration.^[44] Microgels can promote a pro-regenerative M2 phenotype compared to clinical controls such as Oasis Wound Matrix decellularized ECM.^[45] While the influence of macrophage polarization within a single microgel scaffold has been reported,^[46] the impact of altering microgel size and void space on macrophage polarization has not been described.

We seeded IC-21 macrophages in 4.5% PEG-VS large and small microgel scaffolds modified with 1 mM RGD to enable attachment. We also seeded macrophages polarized toward an M1 phenotype to assess how macrophages predisposed toward an inflammatory phenotype respond to differences in void space. We chose this medium stiffness formulation to minimize the effect of substrate stiffness on macrophage polarization.^[47,48] Macrophages were collected after 6 days in culture for assessment of polarization *via* flow cytometry. We utilized our "weak" annealing formulation lacking NVP described in section 2.4 to facilitate macrophage recovery from the gels. A subset of macrophages was stained with CellTrace to permit visualization with fluorescent microscopy and observe their interaction with the microgel scaffolds.

Confocal microscopy of the macrophages revealed that in small microgel scaffolds, macrophages were often sandwiched between individual microgels, with several exhibiting an elongated morphology. Conversely, macrophages easily fit in the void spaces of large microgel scaffolds and generally maintain a rounded morphology (**Figure 3.6A**). In some cases, clusters of macrophages can be seen that were not visible in the small microgel scaffold.

Flow cytometry revealed that both microgels supported high cell viability (**Figure 3.6B,E**). Macrophages with an M1 phenotype (F4/80+CD86+iNOS+ populations) were more prevalent in small microgel scaffolds with both naïve and polarized macrophages (**Figure 3.6C,F**). Macrophages with an M2 phenotype (F4/80+CD206+ARG1+ populations) accounted for significantly more of the macrophages in the large microgel scaffold in both macrophage conditions (**Figure 3.6D,G**). These observations agree with earlier work wherein minimizing macrophage adhesion to implants upregulates the M2 phenotype.^[43,45,49] We also show similar trends exist between naïve and M1 polarized macrophages. This is relevant to wound or surgical sites where M1 macrophages are typically associated.^[50] The increased void space between large microgels limits the amount of contact macrophages have with the scaffold, often with macrophages contacting only one microgel. Conversely, in the small microgel scaffold, macrophages often are contacting multiple microgels at once and are stimulated from all sides. By increasing the porosity, it may be possible to reduce the foreign body response (FBR) to a material and increase the presence of pro-regenerative M2 macrophages as previously reported with other platforms.^[51] Microgels are a promising candidate for porous biomaterials given the tunable void space that exists between them. While the porosity in

the small microgel scaffold was large enough to promote rapid and dense spreading as demonstrated in section 2.5, it may be so small as to promote unintended effects such as a pro-inflammatory response from macrophages. Therefore, when picking a microgel size, it is important to consider the resultant porosity between them.

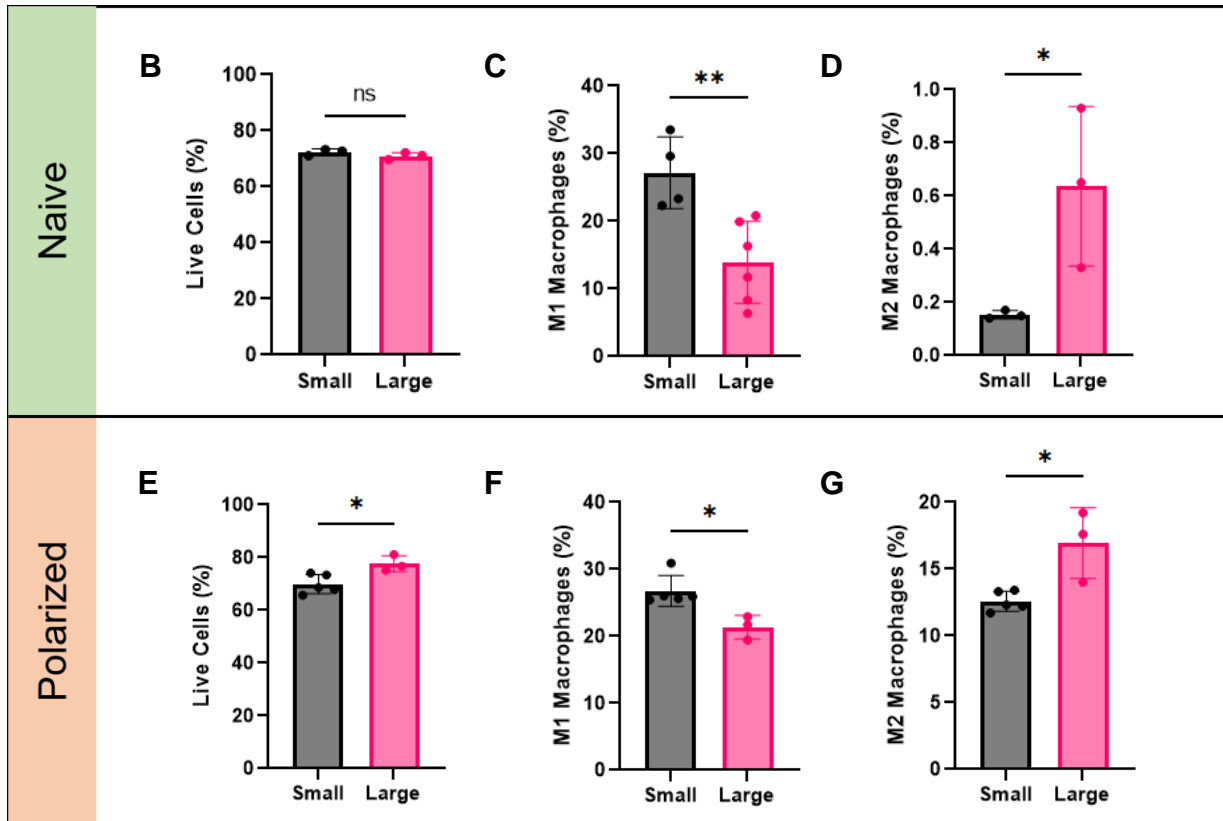
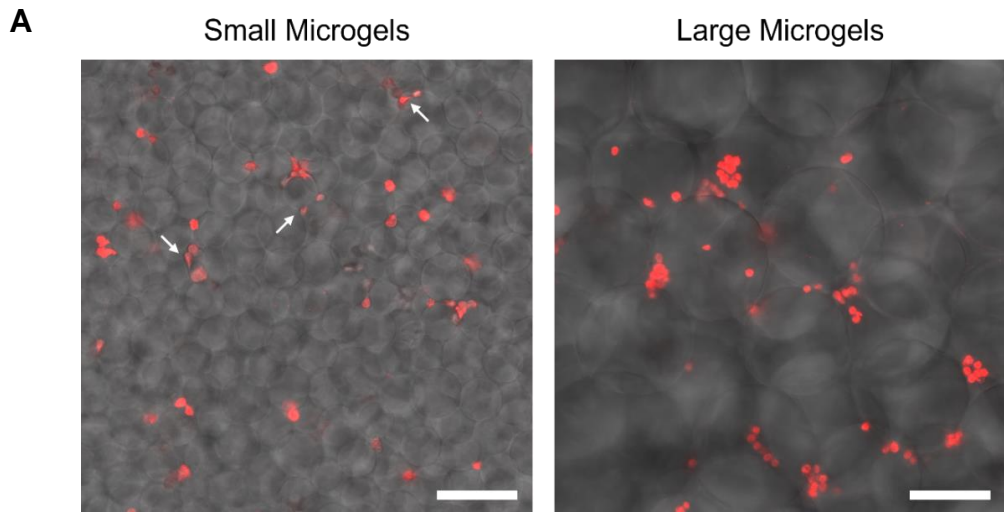


Figure 3.6 Microgel size influences macrophage polarization. **(A)** Macrophages (red) in small microgel scaffolds are trapped between them and exhibit an elongated cell morphology (white arrows). Macrophages in large microgel scaffolds are more rounded and can be found in clusters. **(B,E)** Cell viability is similar in both small and large microgel scaffolds. **(C,F)** M1 polarization is trending towards being higher in the smaller microgel scaffolds. **(D,G)** M2 polarization is greater in large microgel scaffolds. Scale bars represent 100 μm . Statistics: Unpaired Student's t tests. $n \geq 4$. * $p < 0.05$, ** $p < 0.01$.

3.3.7 Microgel scaffolds permit endogenous cell infiltration *in vivo*

Finally, we interrogated how cellular infiltration and macrophage polarization *in vivo* may be influenced in scaffolds formed from different sized microgels. We implanted small and large microgel scaffolds in C57BL/6 mice for 2 weeks to assess endogenous cell migration (**Figure 3.7A**). We used PDMS molds to prevent infiltration from one side of the scaffold to accurately assess migration from the other side (**Figure 3.7B**). Implants were harvested after 2 weeks for histological processing.

Hematoxylin and eosin (H&E) staining revealed that cells tended to migrate further in the large microgel scaffolds (**Figure 3.7C**). Where cells did infiltrate, they surround both sizes of microgels, indicating the porosity in both scaffolds was sufficient for migration. The reduced migration depth in the smaller microgel scaffolds could be a result of the smaller porosity hindering migration or the increased surface area resulting in cells spreading out more densely and impeding invasion. Increased extracellular matrix deposition, evidenced by Masson's trichrome staining, corroborated the increased migration seen in the large microgel scaffolds (**Figure 3.7C**). Larger aggregates of cells

are present between the larger microgels. Notably, collagen is present primarily around the surface of the implants but is scarce in between the microgels themselves. While this indicates a FBR to the PDMS mold in which the microgel scaffolds were housed, it appears the FBR to the microgels themselves was minimized. Immunohistochemistry revealed the presence of both M1 (iNOS+) and M2 (CD206+) macrophages (**Figure 3.7D**). While we did not detect a significant difference in the presence of M2 macrophages, we observed significantly fewer M1 macrophages in the large microgel scaffold (**Figure 3.7E**). The reduction in M1 macrophages as a function of microgel diameter *in vivo* agrees with our *in vitro* findings and suggests that increased scaffold porosity could reduce a pro-inflammatory response to implanted materials.

In vivo implantation resulted in robust endogenous cell spreading and infiltration in our microgel scaffolds. The increased surface area of the smaller microgels resulted in denser spreading near the surface of the scaffold but less migration into the scaffold. Conversely, endogenous cells consistently migrated the depth of the larger microgel scaffolds but were more spread out. This study demonstrates microgels are a promising biomaterial to promote rapid cell infiltration and biomaterial integration. Furthermore, these data further illustrate the importance of pore size and its direct effect on cell density and spreading.

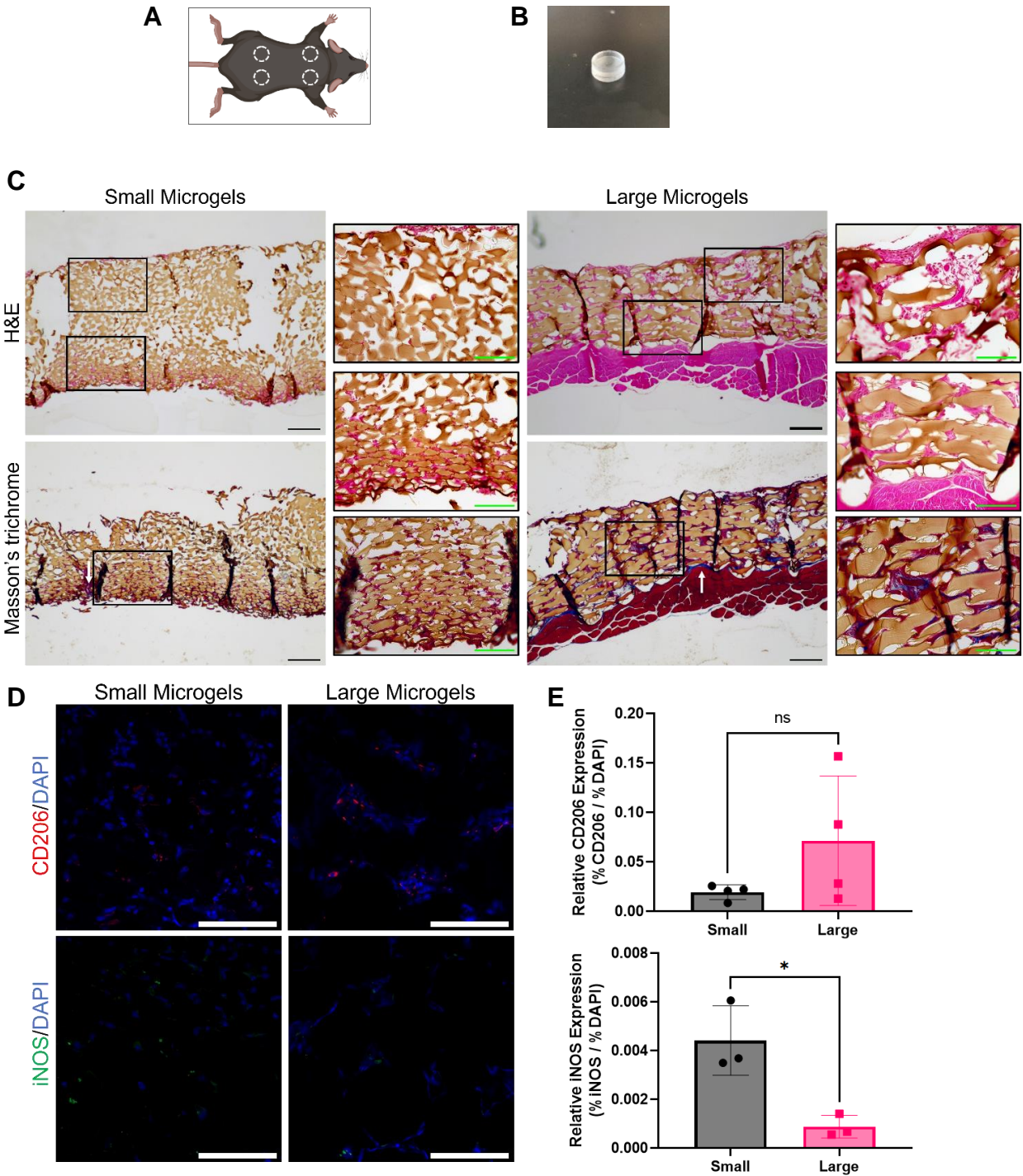


Figure 3.7 Subfascial implantation of microgel scaffolds. **(A)** Microgel scaffolds were implanted in four locations per mouse. **(B)** PDMS mold that was loaded with microgels and implanted. **(C)** H&E and Masson's trichrome staining illustrate greater cell infiltration

into large microgel scaffolds. Fibrous tissue is sometimes present at the microgel interface (white arrows). Primary scale bars represent 200 μm . Inset scale bars represent 100 μm . **(D,E)** IHC reveals a correlation between microgel diameter and macrophage phenotype. Scale bars represent 100 μm . Statistics: Unpaired Student's t tests. $n \geq 3$. * $p < 0.05$.

3.4 Conclusion

Microgels have immense potential in tissue engineering and regeneration given their tailorability, clinical accessibility, and inherent porosity which can be decoupled from stiffness. This method has the advantage of a strong annealing strength, short annealing time, inexpensive reagents, and the ability to anneal at room temperature. The microgels exhibit a large range of stiffnesses and can be frozen without degradation or loss of bioactivity of adhered peptides. We modeled and predicted the differences in void space that emerge due to microgel diameter. We demonstrated how the void space in the microgels can be used as a platform for spheroid formation. Furthermore, we established that while both large and small microgel scaffolds promote rapid cell spreading, the smaller microgels provide more surface area and increase cell density. Upon seeding macrophages in different size microgel scaffolds, we observed increased M2 polarization in the larger microgel scaffold. Finally, we observed robust cell invasion and a limited foreign body response when scaffolds were implanted *in vivo*. Large microgel scaffolds had fewer M1 polarized macrophages compared to small microgel scaffolds *in vivo*, corroborating our *in vitro* findings.

This work contributes to the growing body of work on microgels to guide cell behavior. Our approach to rapidly anneal PEG-VS microgels, coupled with their stability upon cryostorage, makes them even more accessible in the clinic or for preclinical studies. Furthermore, we show how our specific microgel sizes of $\sim 48 \mu\text{m}$ and $146 \mu\text{m}$ facilitate cell spreading, aggregate formation, and macrophage polarization. As the body of evidence grows, we will gain an increased appreciation for how microgel diameter influences cell behavior. The many variables contributing to microgel scaffolds such as polymer composition, crosslinker, stiffness, diameter, packing density, and annealing enable tremendous tunability and expand the possible type and techniques to synthesize microgel formulations. This work expands upon the possible combinations and offers insight into how this specific annealing method and microgel formulation could be utilized for research on the bench and in the clinic.

This work demonstrates not only the advantages of microgel scaffolds as an emerging biomaterial, but the importance of designing a biomaterial with the appropriate porosity. Differences in microgel size directly correlate with porosity, which in turn influences how cells spread, interact, and ultimately their phenotype. Microgels are a promising alternative to solid implants or nanoporous bulk hydrogels. They can be delivered in a less invasive manner compared to bulk scaffolds or autologous implants and enable increased porosity compared to conventional bulk hydrogels. The increased cell infiltration and material integration made possible with microgel scaffolds may reduce the foreign body response induced by implants and create an increased pro-regenerative response. Future work can utilize combinations of specifically tailored microgels to target complex tissue repair.

3.5 References

- [1] S.M.V. Belleghem, B. Mahadik, K.L. Snodderly, J.P. Fisher, Overview of Tissue Engineering Concepts and Applications, in: *Biomaterials Science*, Elsevier, 2020: pp. 1289–1316.
- [2] N. Ashammakhi, S. Ahadian, M.A. Darabi, M. El Tahchi, J. Lee, K. Suthiwanich, A. Sheikhi, M.R. Dokmeci, R. Oklu, A. Khademhosseini, Minimally Invasive and Regenerative Therapeutics, *Adv. Mater.* 31 (2019) 1804041.
- [3] J.M. Lowen, J.K. Leach, Functionally Graded Biomaterials for Use as Model Systems and Replacement Tissues, *Adv. Funct. Mater.* 30 (2020) 1909089.
- [4] A.C. Daly, L. Riley, T. Segura, J.A. Burdick, Hydrogel microparticles for biomedical applications, *Nat. Rev. Mater.* 5 (2020) 20–43.
- [5] A.S. Caldwell, B.A. Aguado, K.S. Anseth, Designing Microgels for Cell Culture and Controlled Assembly of Tissue Microenvironments, *Adv. Funct. Mater.* 30 (2020) 1907670.
- [6] B.N. Pfaff, L.J. Pruetz, N.J. Cornell, J. de Rutte, D. Di Carlo, C.B. Highley, D.R. Griffin, Selective and Improved Photoannealing of Microporous Annealed Particle (MAP) Scaffolds, *ACS Biomater. Sci. Eng.* 7 (2021) 422–427.
- [7] D.R. Griffin, W.M. Weaver, P.O. Scumpia, D. Di Carlo, T. Segura, Accelerated wound healing by injectable microporous gel scaffolds assembled from annealed building blocks, *Nat. Mater.* 14 (2015) 737–744.
- [8] T.H. Qazi, J. Wu, V.G. Muir, S. Weintraub, S.E. Gullbrand, D. Lee, D. Issadore, J.A. Burdick, Anisotropic Rod-Shaped Particles Influence Injectable Granular Hydrogel Properties and Cell Invasion, *Adv. Mater.* (2022) 2109194.

- [9] S. Xin, C.A. Gregory, D.L. Alge, Interplay between degradability and integrin signaling on mesenchymal stem cell function within poly(ethylene glycol) based microporous annealed particle hydrogels, *Acta Biomater.* 101 (2020) 227–236.
- [10] Q. Feng, D. Li, Q. Li, X. Cao, H. Dong, Microgel assembly: Fabrication, characteristics and application in tissue engineering and regenerative medicine, *Bioact. Mater.* 9 (2022) 105–119.
- [11] T.H. Qazi, J.A. Burdick, Granular hydrogels for endogenous tissue repair, *Biomater. Biosyst.* 1 (2021) 100008.
- [12] M.P. Lutolf, J.L. Lauer-Fields, H.G. Schmoekel, A.T. Metters, F.E. Weber, G.B. Fields, J.A. Hubbell, Synthetic matrix metalloproteinase-sensitive hydrogels for the conduction of tissue regeneration: Engineering cell-invasion characteristics, *Proc. Natl. Acad. Sci. U.S.A.* 100 (2003) 5413–5418.
- [13] B.P. James, W. Sicheng, P.-H. Qiang, Q.-J. Marianne, Secretion of matrix metalloproteinase-9 by macrophages, *in vitro*, in response to *Helicobacter pylori*, *FEMS Immunol. Med. Microbiol.* 45 (2005) 159–169.
- [14] J.M. de Rutte, J. Koh, D. Di Carlo, Scalable High-Throughput Production of Modular Microgels for In Situ Assembly of Microporous Tissue Scaffolds, *Adv. Funct. Mater.* 29 (2019) 1900071.
- [15] C. Ji, A. Khademhosseini, F. Dehghani, Enhancing cell penetration and proliferation in chitosan hydrogels for tissue engineering applications, *Biomaterials.* 32 (2011) 9719–9729.

- [16] N. Annabi, J.W. Nichol, X. Zhong, C. Ji, S. Koshy, A. Khademhosseini, F. Dehghani, Controlling the Porosity and Microarchitecture of Hydrogels for Tissue Engineering, *Tissue Eng., Part B*. 16 (2010) 371–383.
- [17] E. Sideris, D.R. Griffin, Y. Ding, S. Li, W.M. Weaver, D. Di Carlo, T. Hsiai, T. Segura, Particle Hydrogels Based on Hyaluronic Acid Building Blocks, *ACS Biomater. Sci. Eng.* 2 (2016) 2034–2041.
- [18] A.S. Caldwell, G.T. Campbell, K.M.T. Shekiri, K.S. Anseth, Clickable Microgel Scaffolds as Platforms for 3D Cell Encapsulation, *Adv. Healthcare Mater.* 6 (2017) 1700254.
- [19] N.F. Truong, E. Kurt, N. Tahmizyan, S.C. Lesher-Pérez, M. Chen, N.J. Darling, W. Xi, T. Segura, Microporous annealed particle hydrogel stiffness, void space size, and adhesion properties impact cell proliferation, cell spreading, and gene transfer, *Acta Biomater.* 94 (2019) 160–172.
- [20] S. Xin, O.M. Wyman, D.L. Alge, Assembly of PEG Microgels into Porous Cell-Instructive 3D Scaffolds via Thiol-Ene Click Chemistry, *Adv. Healthcare Mater.* 7 (2018) 1800160.
- [21] H. Lv, L. Li, M. Sun, Y. Zhang, L. Chen, Y. Rong, Y. Li, Mechanism of regulation of stem cell differentiation by matrix stiffness, *Stem Cell Res. Ther.* 6 (2015) 103.
- [22] J. Whitehead, K.H. Griffin, M. Gionet-Gonzales, C.E. Vorwald, S.E. Cinque, J.K. Leach, Hydrogel mechanics are a key driver of bone formation by mesenchymal stromal cell spheroids, *Biomaterials*. 269 (2021) 120607.
- [23] T. Gonzalez-Fernandez, A.J. Tenorio, A.M. Saiz Jr, J.K. Leach, Engineered Cell-Secreted Extracellular Matrix Modulates Cell Spheroid Mechanosensing and

- Amplifies Their Response to Inductive Cues for the Formation of Mineralized Tissues, *Adv. Healthcare Mater.* 11 (2022) 2102337.
- [24] C.E. Vorwald, S.S. Ho, J. Whitehead, J.K. Leach, High-Throughput Formation of Mesenchymal Stem Cell Spheroids and Entrapment in Alginate Hydrogels, in: K. Chawla (Ed.), *Biomaterials for Tissue Engineering*, Springer New York, New York, NY, 2018: pp. 139–149.
- [25] T. Gonzalez-Fernandez, A.J. Tenorio, J.K. Leach, Three-Dimensional Printed Stamps for the Fabrication of Patterned Microwells and High-Throughput Production of Homogeneous Cell Spheroids, *3D Print. Addit. Manuf.* 7 (2020) 139–147.
- [26] L.R. Nih, E. Sideris, S.T. Carmichael, T. Segura, Injection of Microporous Annealing Particle (MAP) Hydrogels in the Stroke Cavity Reduces Gliosis and Inflammation and Promotes NPC Migration to the Lesion, *Adv. Mater.* 29 (2017) 1606471.
- [27] J.E. Mealy, J.J. Chung, H. Jeong, D. Issadore, D. Lee, P. Atluri, J.A. Burdick, Injectable Granular Hydrogels with Multifunctional Properties for Biomedical Applications, *Adv. Mater.* 30 (2018) 1705912.
- [28] Q. Feng, Q. Li, H. Wen, J. Chen, M. Liang, H. Huang, D. Lan, H. Dong, X. Cao, Injection and Self-Assembly of Bioinspired Stem Cell-Laden Gelatin/Hyaluronic Acid Hybrid Microgels Promote Cartilage Repair In Vivo, *Adv. Funct. Mater.* 29 (2019) 1906690.
- [29] J.R. Day, A. David, J. Kim, E.A. Farkash, M. Cascalho, N. Milašinović, A. Shikanov, The impact of functional groups of poly(ethylene glycol) macromers on the physical

- properties of photo-polymerized hydrogels and the local inflammatory response in the host, *Acta Biomater.* 67 (2018) 42–52.
- [30] Y. Hao, H. Shih, Z. Muñoz, A. Kemp, C.-C. Lin, Visible light cured thiol-vinyl hydrogels with tunable degradation for 3D cell culture, *Acta Biomater.* 10 (2014) 104–114.
- [31] C.F. Guimarães, L. Gasperini, A.P. Marques, R.L. Reis, The stiffness of living tissues and its implications for tissue engineering, *Nat. Rev. Mater.* 5 (2020) 351–370.
- [32] A.R. Anderson, E. Nicklow, T. Segura, Particle fraction is a bioactive cue in granular scaffolds, *Acta Biomater.* 150 (2022) 111–127.
- [33] K. Hosoyama, C. Lazurko, M. Muñoz, C.D. McTiernan, E.I. Alarcon, Peptide-Based Functional Biomaterials for Soft-Tissue Repair, *Front. Bioeng. Biotechnol.* 7 (2019) 205.
- [34] T. Xu, Random close packing (RCP) on arbitrary distribution of circle sizes, (n.d.). <https://github.com/BluesBlues213/random-close-packing> (accessed April 2, 2022).
- [35] M. Diez-Silva, M. Dao, J. Han, C.-T. Lim, S. Suresh, Shape and Biomechanical Characteristics of Human Red Blood Cells in Health and Disease, *MRS Bull.* 35 (2010) 382–388.
- [36] M.B. Ginzberg, R. Kafri, M. Kirschner, On being the right (cell) size, *Science.* 348 (2015) 1245075–1245075.
- [37] K.C. Murphy, B.P. Hung, S. Browne-Bourne, D. Zhou, J. Yeung, D.C. Genetos, J.K. Leach, Measurement of oxygen tension within mesenchymal stem cell spheroids, *J. R. Soc., Interface.* 14 (2017) 20160851.

- [38] M. Fathi-Achachelouei, H. Knopf-Marques, C.E. Ribeiro da Silva, J. Barthès, E. Bat, A. Tezcaner, N.E. Vrana, Use of Nanoparticles in Tissue Engineering and Regenerative Medicine, *Front. Bioeng. Biotechnol.* 7 (2019) 113.
- [39] M.A. Gionet-Gonzales, J.K. Leach, Engineering principles for guiding spheroid function in the regeneration of bone, cartilage, and skin, *Biomed. Mater.* 13 (2018) 034109.
- [40] K.C. Murphy, S.Y. Fang, J.K. Leach, Human mesenchymal stem cell spheroids in fibrin hydrogels exhibit improved cell survival and potential for bone healing, *Cell Tissue Res.* 357 (2014) 91–99.
- [41] J. Koh, D.R. Griffin, M.M. Archang, A. Feng, T. Horn, M. Margolis, D. Zalazar, T. Segura, P.O. Scumpia, D. Carlo, Enhanced In Vivo Delivery of Stem Cells using Microporous Annealed Particle Scaffolds, *Small.* 15 (2019) 1903147.
- [42] C.E. Vorwald, S. Joshee, J.K. Leach, Spatial localization of endothelial cells in heterotypic spheroids influences Notch signaling, *J. Mol. Med.* 98 (2020) 425–435.
- [43] B.D. Ratner, A pore way to heal and regenerate: 21st century thinking on biocompatibility, *Regener. Biomater.* 3 (2016) 107–110.
- [44] Y. Liu, T. Segura, Biomaterials-Mediated Regulation of Macrophage Cell Fate, *Front. Bioeng. Biotechnol.* 8 (2020) 609297.
- [45] L.J. Pruet, C.H. Jenkins, N.S. Singh, K.J. Catallo, D.R. Griffin, Heparin Microislands in Microporous Annealed Particle Scaffolds for Accelerated Diabetic Wound Healing, *Adv. Funct. Mater.* 31 (2021) 2104337.

- [46] A.S. Caldwell, V.V. Rao, A.C. Golden, D.J. Bell, J.C. Grim, K.S. Anseth, Mesenchymal stem cell-inspired microgel scaffolds to control macrophage polarization, *Bioeng. Transl. Med.* 6 (2021).
- [47] M. Haschak, S. LoPresti, E. Stahl, S. Dash, B. Popovich, B.N. Brown, Macrophage phenotype and function are dependent upon the composition and biomechanics of the local cardiac tissue microenvironment, *Aging.* 13 (2021) 16938–16956.
- [48] M. Chen, Y. Zhang, P. Zhou, X. Liu, H. Zhao, X. Zhou, Q. Gu, B. Li, X. Zhu, Q. Shi, Substrate stiffness modulates bone marrow-derived macrophage polarization through NF- κ B signaling pathway, *Bioact. Mater.* 5 (2020) 880–890.
- [49] E.M. Sussman, M.C. Halpin, J. Muster, R.T. Moon, B.D. Ratner, Porous Implants Modulate Healing and Induce Shifts in Local Macrophage Polarization in the Foreign Body Reaction, *Ann. Biomed. Eng.* 42 (2014) 1508–1516.
- [50] P. Krzyszczyk, R. Schloss, A. Palmer, F. Berthiaume, The Role of Macrophages in Acute and Chronic Wound Healing and Interventions to Promote Pro-wound Healing Phenotypes, *Front. Physiol.* 9 (2018) 419.
- [51] L.R. Madden, D.J. Mortisen, E.M. Sussman, S.K. Dupras, J.A. Fugate, J.L. Cuy, K.D. Hauch, M.A. Laflamme, C.E. Murry, B.D. Ratner, Proangiogenic scaffolds as functional templates for cardiac tissue engineering, *Proc. Natl. Acad. Sci. U.S.A.* 107 (2010) 15211–15216.

Chapter 4: Osteogenic and Chondrogenic Microgels for Spatial Differentiation of Mesenchymal Stromal Cells

4.1 Introduction

Cartilage degeneration results in pain and loss of joint mobility and can progress to osteoarthritis, which affects nearly 530 million people globally as of 2019.^[1] Osteochondral lesions involve both the articular cartilage and the subchondral bone which make up the osteochondral unit. Damage to the subchondral bone can introduce fissures that penetrate calcified cartilage, resulting in the exchange of cytokines and prostaglandins that further result in tissue damage.^[2] Common treatments for osteochondral repair include microfracture and autologous (*i.e.*, MACI) or allogeneic juvenile chondrocyte implantation. However, these approaches suffer from shortcomings such as fibrocartilage formation, donor site morbidity, and disease transmission, respectively.^[3,4]

Tissue engineering has emerged as an alternative strategy for the repair of osteochondral defects.^[5] Mesenchymal stromal cells (MSCs) are typically used due to their ability to differentiate into both osteoblasts and chondrocytes.^[6,7] As a result, many studies aim to design a biomaterial which can promote differentiation into both lineages.^[8] Functionally graded biomaterials provide suitable substrates for complex tissues by mimicking gradients in properties such as stiffness or porosity.^[9] Multi-phasic scaffolds have been widely studied, such as a chitosan-gelatin /poly(L-lactide-co-glycolide) scaffolds with dual-delivery of transforming growth factor beta 1 (TGF- β 1) and bone morphogenetic 2 (BMP-2).^[10] Bilayer, peptide-functionalized scaffolds increased wound

healing in a rabbit osteochondral defect model.^[11] More recently, microgel platforms have been used which have several advantages over bulk hydrogels including modularity and inherent microporosity which permits increased cell migration. Microgels with different levels of stiffness have been 3D printed with bone ink to selectively promote osteogenesis and chondrogenesis.^[12] Chondroitin sulfate functionalized microgels have been injected into a rat knee osteochondral defect to promote articular cartilage regeneration, resulting in increased glycosaminoglycan production and minimal inflammatory response.^[13] Microgel adhesivity and mineralization have also been tuned to dictate osteogenic or chondrogenic differentiation in rabbit adipose stromal cells.^[14] However, none of these studies used photoannealing to assemble two distinct microgel populations *in situ*. While 3D printing can be used to layer two microgel formulations, it is difficult to 3D print directly into an irregularly shaped defect. Furthermore, the use of Michael addition for annealing requires the mixing of an additional solution containing crosslinker at a suitable pH and can assemble in as little as 3 seconds, leaving little room for adjustment of scaffold shape.^[14]

To build upon this previous work, we present a novel microgel platform that uses biochemical and mechanical signaling to direct MSC differentiation. Through the addition of peptides and modulation of stiffness, we describe a tunable platform to spatially control the differentiation of MSCs. The modularity of microgels permits us to create a heterogeneous scaffold well suited to the complex nature of osteochondral tissue. Annealing the microgels *via* UV light enables seamless integration between our scaffold layers after they are deposited. Comparatively, multi-layer hydrogel scaffolds with sequential polymerization steps can result in weak interfacial strength and delamination,

along with an abrupt transition of cues.^[15,16] Herein, we examine MSC differentiation in our microgel platform compared to a conventional degradable bulk hydrogel. We then synthesize a heterogeneous scaffold composed of osteogenic and chondrogenic microgels and examine the ability of microgels to spatially control MSC differentiation.

4.2. Materials and methods

4.2.1 PEG-DWIVA fabrication

The thiol group of the cysteine amino acid in the DWIVA peptide (GCGGGDWIVAG, Genscript, Piscataway, NJ) was coupled to PEG-vinyl sulfone (PEG-VS) *via* Michael addition reaction as previously described.^[17] Briefly, PEG-VS was dissolved (1% w/v) in 200 mM triethanolamine (TEOA, pH 8, Millipore Sigma, Burlington, MA). DWIVA in solution (50 mM in PBS) was added dropwise to reach a final concentration of 2 mM when fabricated into a hydrogel. The solution was left stirring overnight at room temperature after which it was pipetted into 3500 Da molecular weight cut off (MWCO) dialysis tubing (Spectrum Laboratories, New Brunswick, NJ). The tubes were maintained in ultrapure water for the next 2.5 days, with water changes every 6-12 hr. The PEG-VS-DWIVA solution was then recovered from the tubing, filtered through a 0.22 μm pore filter, and lyophilized until dry. Other peptides were added during hydrogel fabrication as described below. Peptide modification of PEG was confirmed via ^1H NMR.^[18] Briefly, samples were dissolved in D_2O (Millipore Sigma) at 1 mM concentration and recorded using an 800 MHz Bruker Avance III NMR spectrometer.

4.2.2 Microgel fabrication

Microgels were fabricated using a previously described microfluidic device.^[19] For chondrogenic microgels, the aqueous phase consisted of 8-arm 10 kDa PEG-VS (JenKem, Plano, Tx), 3.5 kDa PEG-dithiol (PEG-DT) (JenKem), and HAVDI peptide (Ac-HAVDIGGGC, Genscript) in 0.15 M TEOA (pH 5.1) buffer. The final microgel concentrations were 3 mM PEG-VS, 7.2 mM PEG-DT, and 1 mM HAVDI. To fabricate osteogenic microgels, the aqueous phase consisted of 8-arm 10 kDa PEG-VS pre-functionalized with DWIVA peptide, 3.5 kDa PEG-DT, and RGD peptide (Ac-RGDSPGERCG-NH₂, Genscript). The final concentrations were 9 mM PEG-VS, 21.6 mM PEG-DT, 2 mM DWIVA, and 1 mM RGD. The oil phase consisted of Novec 7500 Oil and 0.75 wt% Picosurf (Sphere Fluidics, Cambridgeshire, UK). After exiting the device, microgels were combined with a solution of 1% v/v triethylamine (TEA, Millipore Sigma) in Novec 7500 Oil using a Y-junction (IDEX Health and Science, Rohnert Park, CA) and left at room temperature overnight to ensure complete crosslinking. Microgels were cleaned as we described.^[20] Microgels were imaged with brightfield microscopy (Nikon Eclipse TE2000U) and diameters measured using ImageJ. Peptide modification was confirmed *via* ¹H NMR as described above.

4.2.3 PEG bulk gel fabrication

Bulk gels were formed with the same concentration of reagents except PEG-DT was replaced with the MMP-degradable crosslinker GPQ-A (GCRDGPQGIAGQDRCG, Genscript). A precursor solution consisting of PEG-VS and peptides in a solution of alpha medium (α -MEM, Invitrogen, Carlsbad, CA) at 2x concentration was combined with cells

and pipetted into 6 mm or 8mm x 1.5 mm cylindrical silicon molds. An equal volume of 2x GPQ-A (pH 8.3) in media was then mixed in by pipetting up and down. The gels were incubated at 37°C for 15 minutes before being transferred to a well plate.

4.2.4 Microgel annealing

Microgels were annealed as described in Lowen et al.^[20] Briefly, microgels were suspending in an annealing solution consisting of additional crosslinker in HEPES containing 0.4% VA-086 photoinitiator (FUJIFILM, College Station, Tx) equal to the volume of microgels. After incubating for 1 min, the microgels were spun down for 3 min at 14,000xg. The supernatant was removed and microgels optionally mixed with cells before plating in 6 mm or 8mm x 1.5 mm cylindrical silicon molds. For bilayer scaffolds, the first layer of microgels was deposited into an 8 mm x 1.5 mm cylindrical mold. A second identical mold was laid on top in which the second layer of microgels was deposited. The microgel slurries were then exposed to UV light (20 mW/cm², 320-500 nm, Omnicure S2000) for 2 min to form cylindrical annealed scaffolds with final dimensions of 8 mm x 3 mm. For mixed bilayer scaffolds, osteogenic and chondrogenic microgels were mixed at 1:1 ratio for both layers.

4.2.5 Mechanical testing

The shear storage moduli of 8 mm diameter gels were tested using a Discovery HR2 Hybrid Rheometer (TA Instruments, New Castle, DE) with a stainless steel, cross hatched, 8 mm plate geometry. An oscillatory strain sweep ranging from 0.004% to 4% strain was performed on each gel using an initial 0.3N axial force to obtain the linear

viscoelastic region before failure. Individual microgels were examined using a MicroTester (CellScale, Waterloo, Canada) by loading onto an anvil in a water bath filled with phosphate buffered saline (PBS).^[20] The microgels were then compressed over 30 s to 50% of their original diameter by a stainless-steel platen attached to a tungsten rod. Displacement and force were tracked *via* MicroTester software. The linear region of the of compressive modulus vs nominal strain graph was recorded as the calculated modulus.

4.2.6 Cell culture

Human bone marrow-derived MSCs (RoosterBio, Frederick, MD) from a single donor (21-year-old male) were expanded in growth medium (GM) consisting of α -MEM supplemented with 10% fetal bovine serum (FBS; Atlanta Biologicals, Flowery Branch, GA) and 1% penicillin/streptomycin (Gemini Bio-Products, Sacramento, CA). MSCs were cultured under standard conditions until use at passage 4. Cells were seeded in the gels at 5 million cells/mL, and media changes were performed every 2–3 days. For osteogenic differentiation, scaffolds were kept in α -MEM for 1 day before switching to osteogenic media (GM supplemented with ascorbate 2-phosphate (50 μ g/mL), 10 mM β -glycerophosphate, and 10 nM dexamethasone (all from Millipore Sigma)) for 21 days. For chondrogenic differentiation, scaffolds were kept in α -MEM for 1 day before switching to chondrogenic media (DMEM supplemented with 1% penicillin/streptomycin, 100 μ g/mL sodium pyruvate, 40 μ g/mL L-proline, 50 μ g/mL l-ascorbic acid 2-phosphate, 4.7 μ g/mL linoleic acid, 1.5 mg/mL bovine serum albumin, 1 \times insulin–transferrin–selenium, 10 nM dexamethasone (all from Millipore Sigma) and 10 ng/mL human TGF- β 3 (PeproTech, Westlake Village, CA)) for 21 days. Bilayer scaffolds were cultured in mixed media

consisting of a 50:50 volume ratio of osteogenic and chondrogenic differentiation media, and all media were exchanged every 2 days.

4.2.7 Biochemical assays

DNA content was quantified using the PicoGreen Quant-iT Assay Kit (Invitrogen). Samples were collected in passive lysis buffer (Promega, San Luis Obispo, CA), minced with a razor blade, and homogenized using a Tissue-tearor (Biospec, Bartlesville, OK) at the highest speed for 10 s. Samples were then sonicated for 10 s. Chondrogenic samples were digested with papain enzyme (Millipore Sigma) before quantification. Total collagen content was determined by measuring the hydroxyproline content using the dimethylaminobenzaldehyde and chloramine T assay, assuming a hydroxyproline to collagen ratio of 1:7.69. sGAG content was assessed using the dimethyl methylene blue dye-binding (DMMB) assay. Intracellular ALP expression was quantified using a *p*-nitrophenyl phosphate (PNPP) colorimetric assay wherein absorbance is measured at 405 nm. Calcium deposition was quantified using a Stanbio™ Calcium Liquid Reagent kit (Thermo Fisher, Chicago, IL) after digestion in 1M HCl for 48 hr.

4.2.8 Histology

Scaffolds were fixed in 4% paraformaldehyde (PFA), washed with PBS, paraffin-embedded, and sectioned at 7 μ m. Chondrogenesis was assessed by staining with Alcian Blue (Millipore Sigma) and Nuclear Fast Red (Abcam, Fremont, CA). For immunohistochemical staining, slides were rehydrated and exposed to proteinase K

(Abcam) for antigen retrieval. Samples were then incubated in blocking buffer composed of 10% goat serum and 10 mg/mL Bovine Serum Albumin (BSA) for 30 min at room temperature. Osteocalcin-stained slides were incubated with anti-osteocalcin antibody (1:100, Abcam, ab93876) overnight at 4°C. Slides were then treated with a secondary goat-anti rabbit antibody conjugated to Alexa fluor 647 (1:300, Abcam, b150083) for 1 hr at room temperature. Aggrecan-stained slides were incubated with anti-aggrecan antibody (1:100, Abcam, ab3778) overnight at 4°C. Slides were then treated with a secondary goat-anti mouse antibody conjugated to Alexa fluor 555 (1:300, Abcam, ab150118) for 1 hr at room temperature. Collagen X-stained slides were incubated with an anti-collagen X antibody (1:100, Abcam, ab49945) overnight at 4°C. Slides were then treated with a secondary goat-anti mouse conjugated to Alexa fluor 568 (Abcam, ab175702). DLX5 stained slides were incubated with anti-DLX5 (1:100, AF6710, R&D Systems, Minneapolis, MN) overnight at 4°C. Slides were then treated with NorthernLights 557-conjugated secondary antibody (1:200; NL010, R&D Systems) for 1 hr at room temperature. Slides were counterstained with DAPI (Thermo Fisher). Large tile scans were taken at 20x using confocal microscopy (Leica Stellaris 5, Wetzlar, Germany). Positive signal was quantified in ImageJ after using the Triangle threshold.^[21]

4.2.9 Spatial transcriptomics

Digital spatial profiling (DSP) was performed with the GeoMx DSP (Nanostring, Seattle, WA) human whole-transcriptome atlas. Slides were rehydrated, treated with proteinase K, and stained with aggrecan and osteocalcin antibodies at the concentrations described above. DAPI was replaced with a 1:10 solution of CYTO13 (Thermo Fisher),

as UV light is needed for barcode cleavage. UV-photocleavable barcode-conjugated RNA were hybridized on the slides to capture mRNA from regions of interest (ROIs). Each bilayer scaffold was sectioned into 5 distinct zones (Bone edge, Bone center, Center, Cartilage center, and Cartilage edge), and three technical replicates from each zone were taken from 4 biological replicates. ROIs that expressed less than 3% of the genes, and genes that were expressed in less than 5% of the ROIs, were filtered out. Next, the limit of quantification (LOQ) was defined as two standard deviations above the geometric mean of the negative control probes for each ROI. Targets below the LOQ were excluded from the study. Q3 normalization was performed on all ROIs. Principal component analysis (PCA) and analysis of gene expression was performed using the GeoMx DSP Analysis Suite. Data was exported and graphed in GraphPad Prism 9.

4.2.10 In vivo study

Treatment of experimental animals was in accordance with UC Davis animal care guidelines and all National Institutes of Health animal handling procedures. Before implantation, bilayer and mixed scaffolds were synthesized as described above and preconditioned in mixed media for 1 week. Male and female twelve-week-old NOD/SCID/IL2 γ ^{null} (NSG) mice (Jackson Laboratories, West Sacramento, CA) were anesthetized and maintained under a 2% isoflurane/O₂ mixture delivered through a nose cone. Each animal received two subfascial implants: bilayer microgel scaffold (lower left) and mixed microgel scaffold (lower right). Following a dorsal midline incision, fascia was incised, and blunt dissection was performed between the fascia and muscle belly. Annealed microgels were placed on the muscle and sutured in place with 4-0 Monocryl

sutures (Ethicon, Cornelia, GA). Animals were euthanized after 3 weeks, and gels were collected and fixed in 4% PFA overnight at 4°C. Samples were then washed twice in PBS, paraffin-embedded, and sectioned at 7 µm. IHC staining was performed as described above.

4.2.11 Statistical analysis

Statistical analysis was performed using GraphPad Prism 9. Statistical significance was assessed by either Student's t-test, ratio paired t-test, or one-way ANOVA with Tukey's multiple comparisons test when appropriate. *p*-values <0.05 were considered statistically significant.

4.3 Results

4.3.1 Peptide addition does not alter microgel compressive moduli and microgels have low polydispersity

Microgels were designed to promote MSC differentiation toward an osteogenic or a chondrogenic lineage through biochemical and mechanical cues (**Figure 4.1A**). Chondrogenic microgels contained N-cadherin mimetic peptide (HAVDI) which has been demonstrated to promote chondrogenesis.^[22,23] Osteogenic microgels contained RGD and a BMP-2 mimetic peptide (DWIVA) which has previously promoted osteogenesis.^[17,24] HAVDI and RGD peptides were added during microgel synthesis, while PEG monomer was functionalized with DWIVA beforehand due to solubility issues during fabrication. Successful peptide addition was verified using ¹H NMR analysis (**Figure 4.1B**). DWIVA was confirmed *via* the presence of tryptophan peaks between 7-8

ppm. The presence of RGD was established by arginine peaks at 1.59-1.7 ppm and glutamic acid peaks at 2.4 ppm. Valine and isoleucine peaks confirmed the presence of HAVDI at 0.82-0.88 ppm and 1.9 ppm. Chondrogenic microgels had a compressive modulus of ~12 kPa, and osteogenic microgels had a compressive modulus ~50 kPa. The addition of the peptides did not alter compressive moduli, in keeping with previous results (**Figure 4.1C**).^[25] Chondrogenic microgels had an average diameter of 155 ± 7.0 μm (**Figure 4.1D**), and osteogenic microgels an average diameter of 152 ± 6.1 μm (**Figure 4.1D**). These data verify the synthesis of two microgel populations with distinct mechanical and biochemical properties., yet similar initial diameters. Chondrogenic microgels are softer and present N-cadherin peptides to mimic cell-cell interactions, and osteogenic microgels are stiffer with RGD and DWIVA peptides to promote adhesion and osteogenic differentiation.

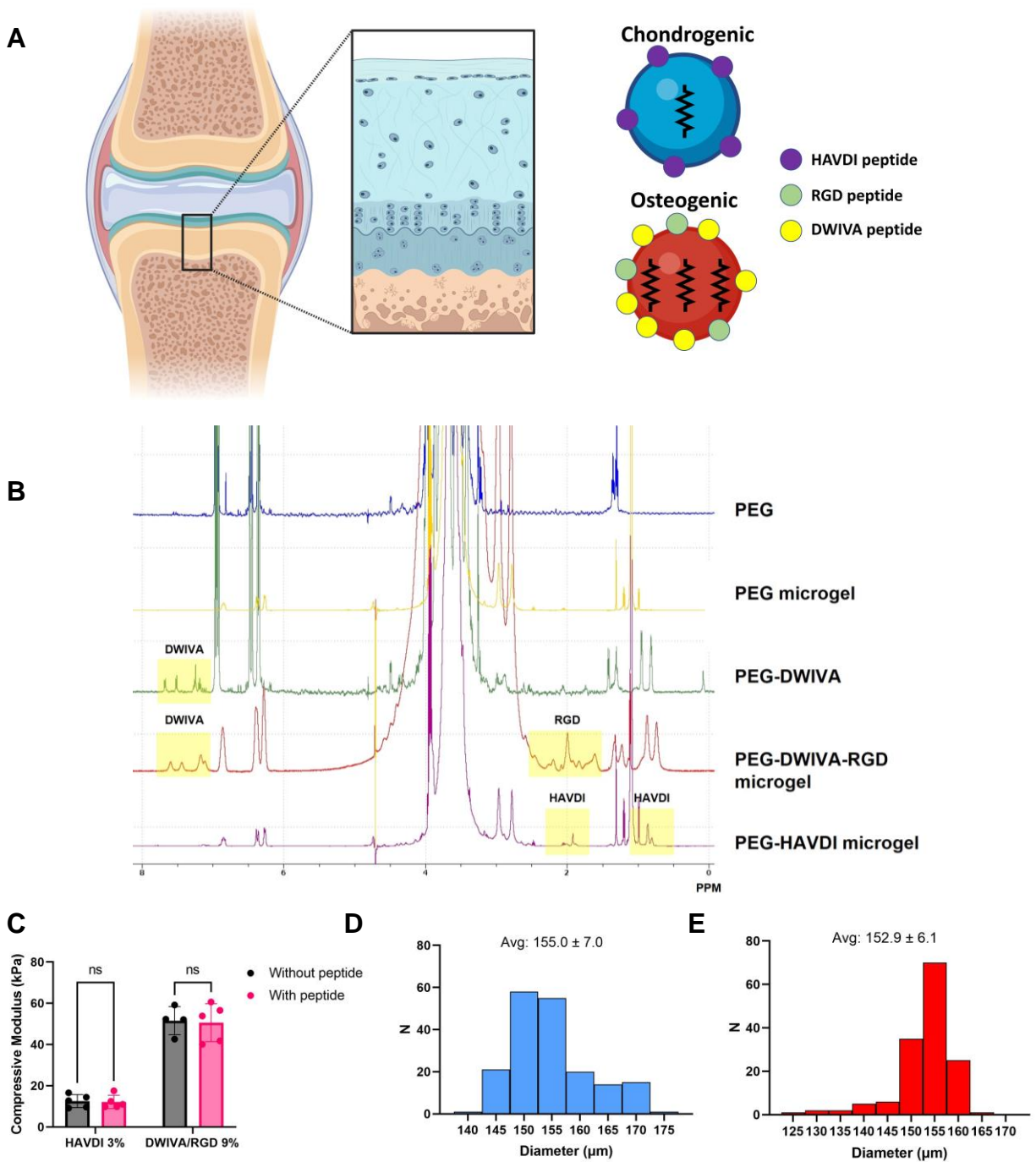


Figure 4.1 Chondrogenic and osteogenic microgels have unique peptides and mechanical properties. (A) Cartoon of osteogenic and chondrogenic microgels and the relevant osteochondral tissue in the knee. Chondrogenic microgels were softer and

contained HAVDI peptide. Osteogenic microgels were stiffer and contained RGD and DWIVA peptides. **(B)** H-NMR confirms the presence of peptides on the microgels. **(C)** Compressive moduli of osteogenic and chondrogenic microgels are not altered by peptide addition. **(D)** Histogram of chondrogenic microgel diameters. **(E)** Histogram of osteogenic microgel diameters. Statistics: Unpaired Student's t tests. $n \geq 4$. $*p < 0.05$.

4.3.2 Chondrogenic microgels outperform bulk gels

To test their chondrogenic potential, we seeded microgel scaffolds with MSCs for 3 weeks and cultured them in chondrogenic media. We compared these constructs to MSCs entrapped in bulk PEG-VS gels containing the same HAVDI peptide. For bulk gels, we used the MMP-degradable crosslinker GPQ-A instead of PEG-DT to permit cellular degradation and migration throughout the gels (**Figure 4.2A**). We found that switching to the GPQ-A crosslinker decreased the storage modulus, so we increased the polymer concentration in the bulk gels to ensure the initial storage moduli were similar (**Figure 4.2B**). After 3 weeks in culture, there was a significant increase in collagen in the microgels compared to bulk gels assessed *via* hydroxyproline assay (**Figure 4.2C**). Normalization to DNA confirmed that not only was there more collagen present, but more collagen was produced per cell. Glycosaminoglycan (GAG) content was also measured *via* DMMB assay after 3 weeks as a marker of chondrogenesis. Similarly, we detected a large increase in GAG content in the microgel scaffolds compared to bulk gels (**Figure 4.2D**). GAG content was assessed visually by staining with Alcian blue (**Figure 4.2E**). The presence of GAGs can be seen around cells in both microgel and bulk constructs. However, there is clearly more GAG deposition in the microgel construct throughout the

microporous void space. These data confirm that microgel scaffolds can support MSC chondrogenesis and outperform conventional bulk gels to promote chondrogenic differentiation.

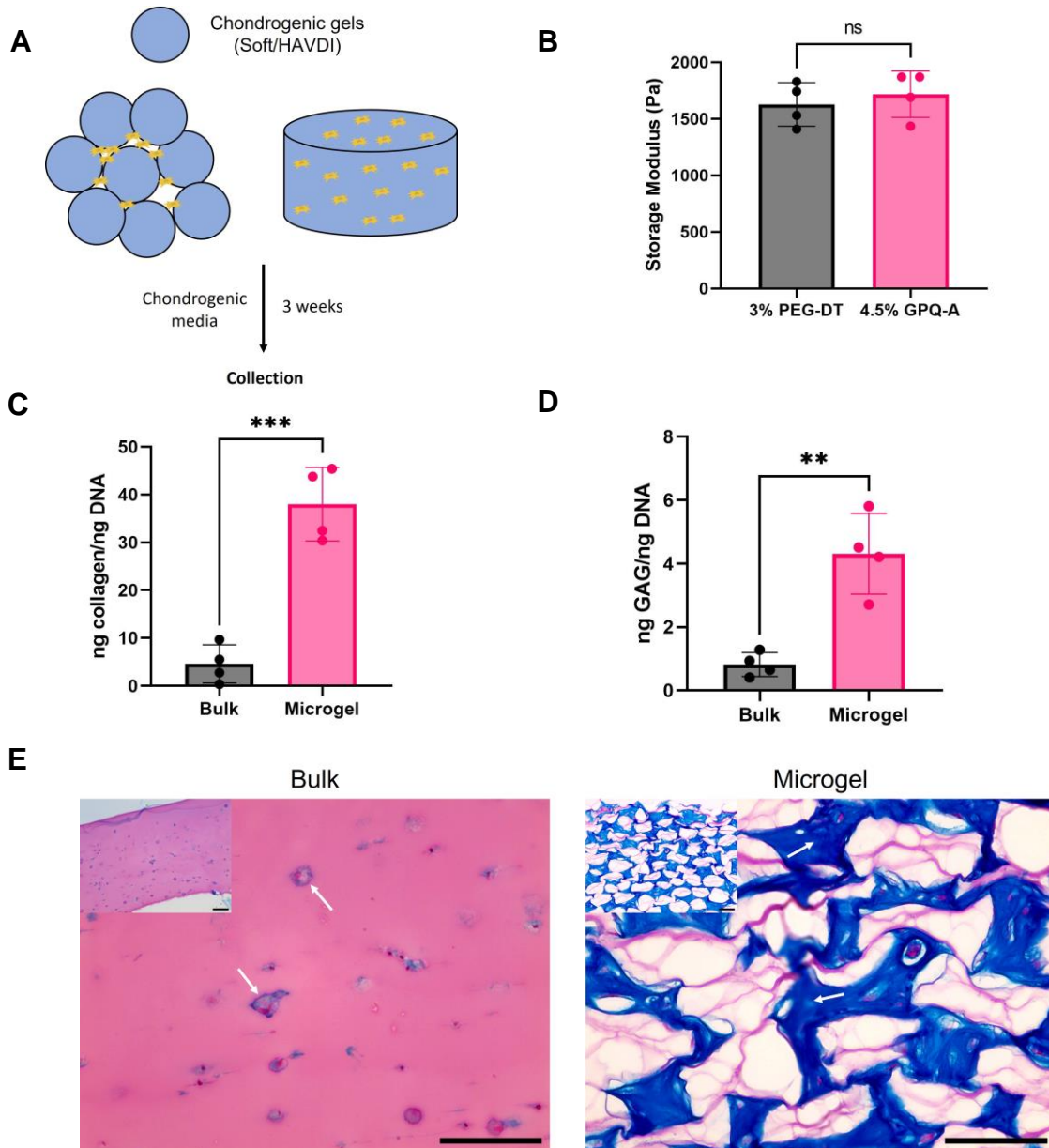


Figure 4.2 Chondrogenic microgels outperform bulk gels. (A) Chondrogenic microgel and bulk gel scaffolds were cultured in chondrogenic media for 3 weeks before collection.

(B) Storage moduli of PEG-VS crosslinked with PEG-DT was matched to PEG-VS crosslinked with GPQ-A. Both (C) collagen content and (D) GAG content were higher in microgel scaffolds compared to bulk gel scaffolds at 3 weeks. (E) Alcian blue stain confirms the presence of increased GAGs in microgel scaffolds (white arrows). Scale bars represent 100 μ m. Statistics: Unpaired Student's t tests. $n \geq 4$. * $p < 0.05$.

4.3.3 Osteogenic microgels outperform bulk gels

We next examined the osteogenic potential of osteogenic microgel scaffolds compared to their bulk gel counterpart. MSCs were seeded in microgels or bulk gels and cultured in osteogenic media for 3 weeks (**Figure 4.3A**). Similar to the chondrogenic bulk gels, osteogenic bulk gels used the MMP degradable crosslinker GPQ-A. To achieve a similar initial storage modulus, polymer concentration was increased from 9% to 13% for GPQ-A containing gels (**Figure 4.3B**). To assess osteogenic differentiation, we measured alkaline phosphatase (ALP) activity at 1 and 3 weeks (**Figure 4.3C**). MSCs in microgel scaffolds had increased ALP activity compared to bulk scaffolds at both timepoints, indicating increased early osteogenic activity. We also assessed calcium output as a late-stage marker of osteogenic differentiation at 3 weeks (**Figure 4.3D**). Overall, calcium output was low for both gels, with bulk gels containing more calcium. However, given the low calcium values, this is most likely due to nonspecific binding and entrapment in the hydrogel. Furthermore, the high ALP output at week 3 suggests it is too early to see significant cellular mineralization as ALP activity is cyclical.^[26] We also performed immunofluorescence staining to observe the presence of osteocalcin, another late-stage marker of osteogenesis.^[27] Osteocalcin was far more abundant in the microgel scaffolds

compared to the bulk gels (**Figure 4.3E**). Together, these data demonstrate our osteogenic microgels can support MSC osteogenesis better than their bulk counterpart.

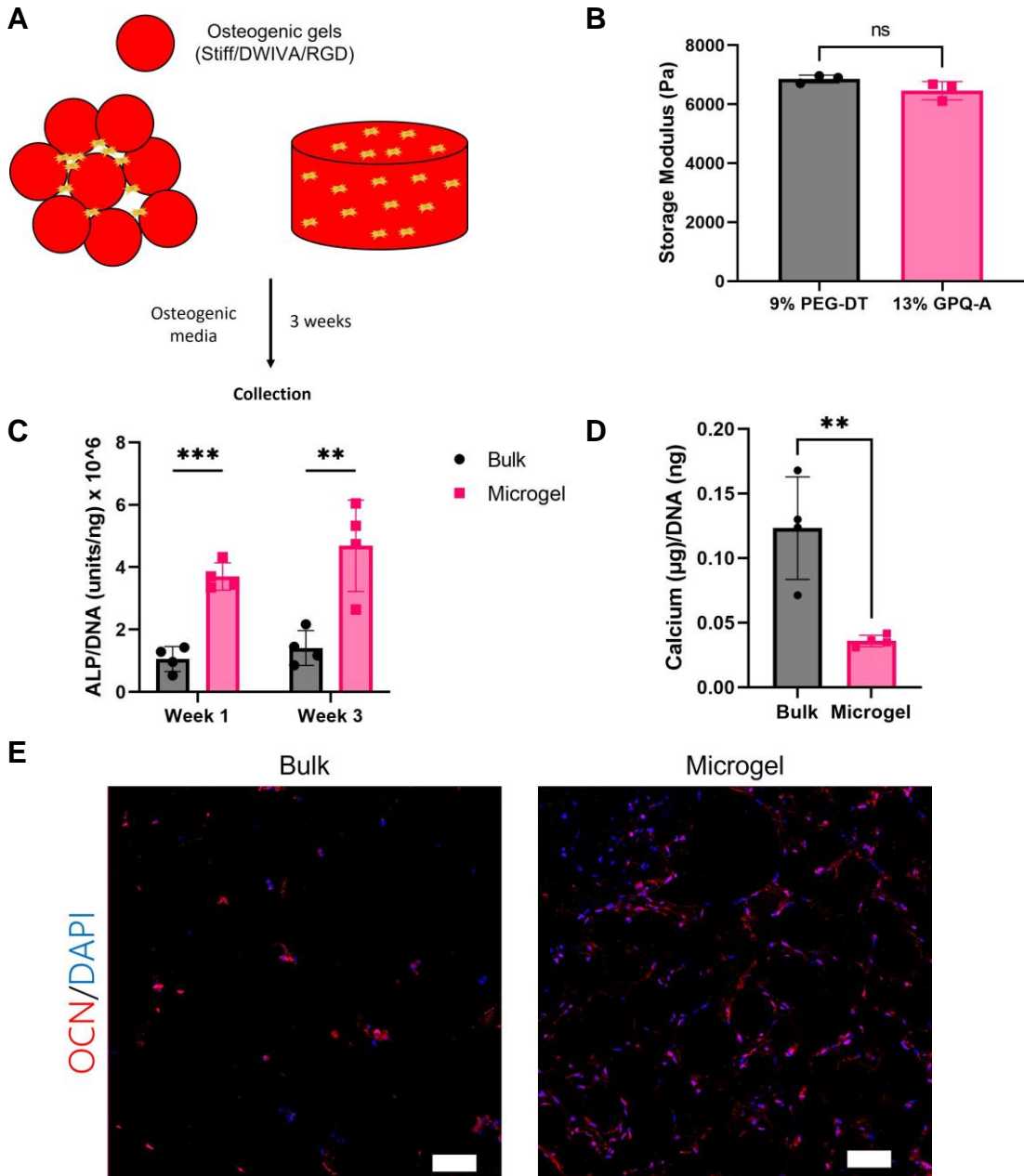


Figure 4.3 Osteogenic microgels outperform bulk gels. (A) Osteogenic microgel and bulk gel scaffolds were cultured in osteogenic media for 3 weeks before collection. **(B)**

Storage moduli of PEG-VS crosslinked with PEG-DT was matched to PEG-VS crosslinked with GPQ-A (n=3). **(C)** ALP expression is higher in microgel scaffolds at week 1 and week 3 (n=4). **(D)** Calcium content is overall low in both gels, but higher in bulk gels due to retention from the media (n=4). **(E)** Osteocalcin staining is significantly higher in microgel scaffolds. Scale bars represent 100 μ m. Statistics: Unpaired Student's t tests. n \geq 3. *p < 0.05, **p < 0.01, and ***p < 0.001.

4.3.4 Bilayer scaffolds promote differential protein expression

We next harnessed the modularity of microgels to build an osteochondral scaffold containing both osteogenic and chondrogenic cues. Bilayer scaffolds consisted of a layer of chondrogenic microgels and a layer osteogenic microgels (**Figure 4.4A**). The scaffolds were seeded with MSCs and cultured for 3 weeks in mixed media. A control scaffold consisting of a random arrangement of osteogenic and chondrogenic microgels was also formed. Hematoxylin and eosin (H&E) staining depicts robust cellular proliferation and ECM deposition after 3 weeks and illustrates the two distinct microgel populations within the scaffolds (**Figure 4.4B**). Increased cellular aggregation is present in some voids on the cartilage side, and a continuous interface between the scaffolds is observed with robust ECM deposition throughout. We examined osteocalcin protein expression as a marker of osteogenesis (**Fig 4C**). When normalized to the void space area on each respective half of the scaffold (necessary to remove the contribution of the microgels), we detected a significant increase of osteocalcin in the osteogenic side of the scaffold. (**Figure 4.4D**) Next, we examined aggrecan as a marker of chondrogenesis (**Figure 4.4E**). We observed a significant increase of aggrecan in the chondrogenic half of the

scaffold when normalized to void space area (**Figure 4.4F**). Collagen X, a marker of endochondral ossification, was more prevalent on the osteogenic side of the bilayer scaffold (**Figure 4.4G,H**). When normalized to total scaffold area there was a trend toward increased osteocalcin and collagen X on the bone side, and increased aggrecan on the cartilage side. The presence of collagen X indicates some of the MSCs are potentially hypertrophic chondrocytes undergoing endochondral ossification. Of note, the mixed microgel scaffold did not have increased osteogenic or chondrogenic protein expression compared to the bone or cartilage side of the microgel scaffolds. data indicate that both the osteogenic and chondrogenic microgels promote MSC differentiation toward their respective phenotype.

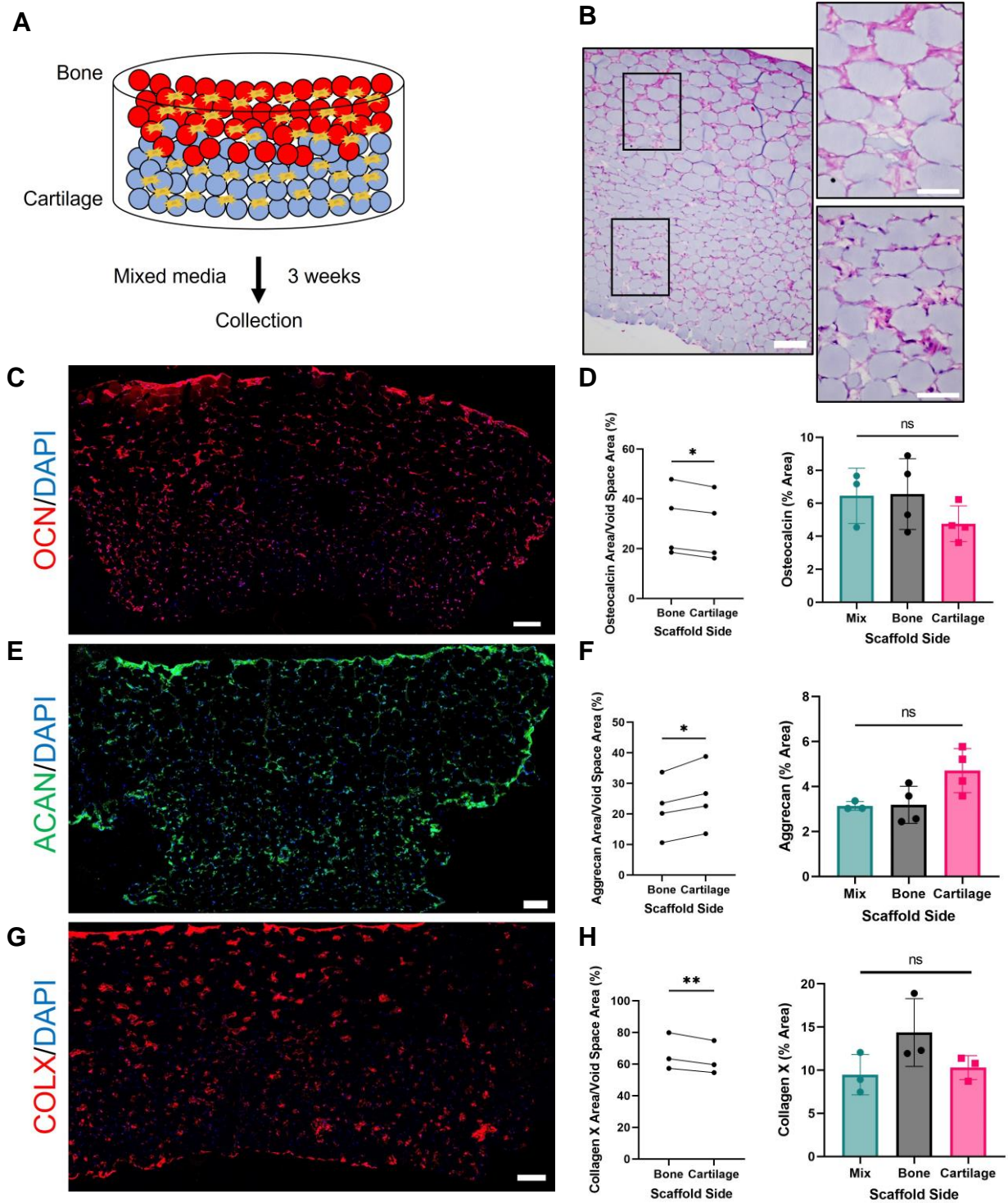


Figure 4.4 Bilayer scaffolds promote osteochondral protein expression. (A) Bilayer microgel scaffolds were cultured in mixed media for 3 weeks. (B) H&E staining illustrates osteogenic and chondrogenic microgel compartments, with smaller microgels on the

chondrogenic side. **(C)** Osteocalcin staining is increased on the bone side of the bilayer scaffold **(D)** Quantification of osteocalcin staining normalized to void space area and total area. **(E)** Aggrecan staining is increased on cartilage side of scaffold. **(F)** Quantification of aggrecan staining normalized to void space area and total area. **(G)** Collagen X staining is increased on the bone side of the scaffold. **(H)** Quantification of collagen x normalized to void space area and total area. Scale bars: **(B)** Primary scale bar represents 200 μm . Inset scale bars represents 100 μm . **(C,E,G)** Scale bar represents 200 μm . Statistics: Ratio paired t test and ordinary one-way ANOVA. $n \geq 3$. * $p < 0.05$, ** $p < 0.01$.

4.3.5 Bilayer scaffolds promote differential gene expression

To further characterize the bilayer scaffolds, we analyzed gene expression using the Nanostring GeoMx Digital Spatial Profiler. Each scaffold was divided into 5 sections (bone edge, bone center, center, cartilage center, and cartilage edge) to assess RNA expression **(Figure 4.5A)**. PCA analysis revealed distinct clustering for each ROI, indicating that not only did microgel population have an influence on cell genotype, but proximity towards the edge or center of the scaffold also had an effect **(Figure 4.5B)**. This distinct clustering was further confirmed through unsupervised hierarchical clustering, which clusters the segments in order of similar gene expression **(Figure 4.5C)**. Through the unbiased hierarchical clustering the zones were generally clustered in order from cartilage edge to bone edge, reaffirming that gene expression changed as a function of scaffold location. Finally, we assessed osteogenic and chondrogenic gene expression in each section of the scaffold relative to each other. **(Figure 4.5D)**. Osteogenic genes were upregulated in the bone edge and bone center, and generally downregulated in the center

and cartilage center. Meanwhile, chondrogenic gene expression was strongly down regulated in the bone edge and upregulated in the bone center, center, and cartilage center. *Sox9* was most upregulated in the cartilage center. The cartilage edge exhibited limited expression of osteogenic and chondrogenic genes, apart from downregulated *Runx2* and *OGN*. *COL10A1*, a gene encoding for collagen X, was upregulated in the bone edge yet down regulated in the center and cartilage center. Overall, these results demonstrate the upregulation of osteogenic genes on the bone side of the scaffold and chondrogenic genes on the cartilage side of the scaffold.

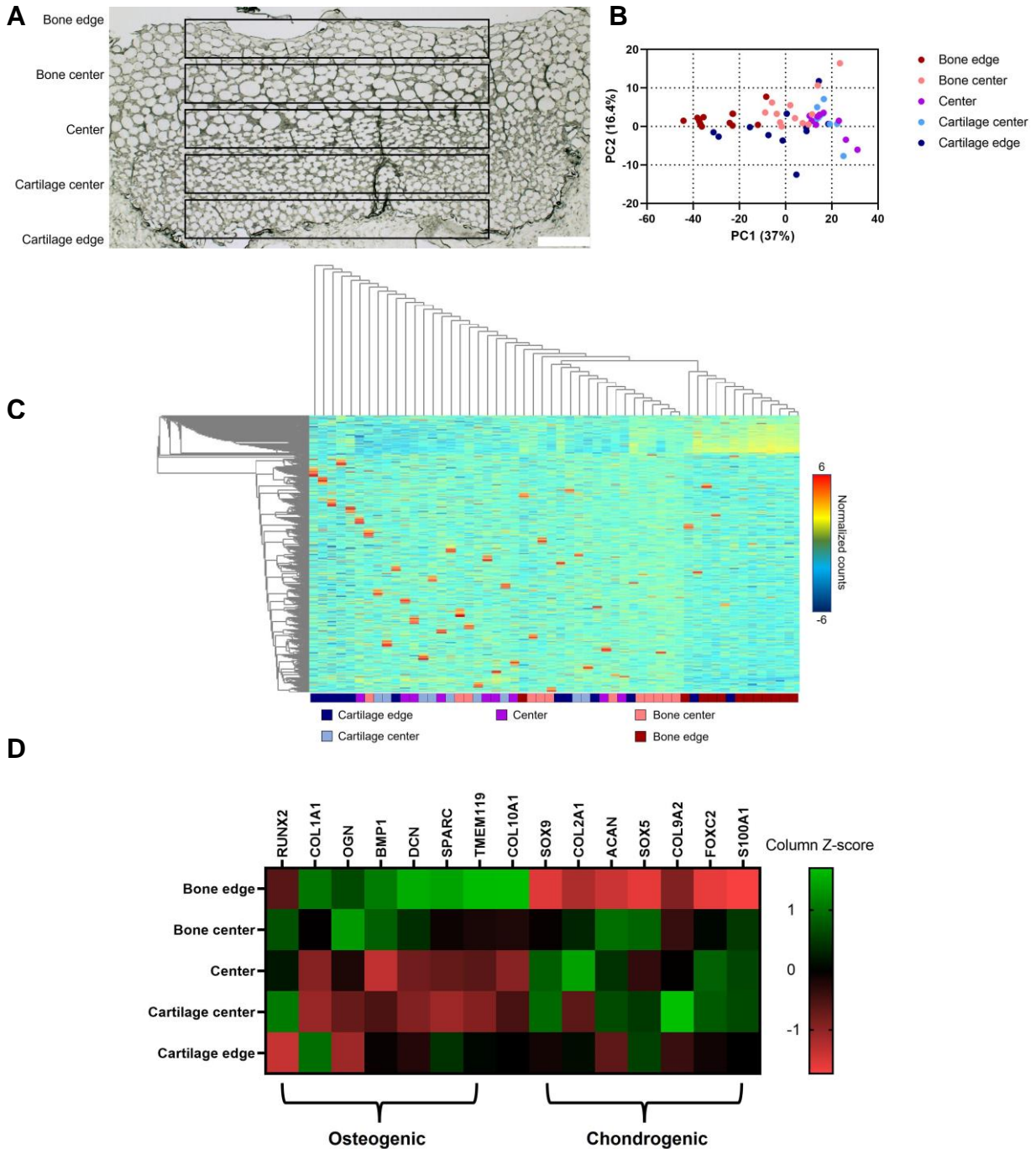


Figure 4.5 Bilayer scaffolds promote osteochondral gene expression as a function of spatial position. (A) Bilayer scaffolds were divided into 5 zones for analysis of RNA expression. Scale bar represents 200 μ m. (B) PCA plot shows clustering for each of the 5 zones. (C) Unsupervised hierarchical clustering further demonstrated clustering of

zones, as well as general ordering from cartilage edge to bone edge. **(D)** Osteogenic genes and chondrogenic genes were upregulated in their respective halves of the scaffold.

4.3.6 Subfascial bilayer scaffolds promote increased osteogenesis on bone side of scaffold

Finally, we investigated the ability of the scaffolds to maintain an osteochondral phenotype when implanted. Scaffolds were preconditioned in mixed media for 1 week and implanted in the back of NSG mice for 3 weeks, after which they were explanted and stained. **(Figure 4.6A)** H&E staining confirmed robust ECM deposition with notable infiltration on both sides of the scaffold **(Figure 4.6B)**. Alcian blue staining revealed GAG deposition primarily in the center of the scaffold, with a lack of staining near the edges where host cell invasion occurred. **(Figure 4.6C)**. We then stained for human-specific anti-distal-less homeobox 5 (DLX5), a marker of MSC osteogenesis **(Figure 4.6D)**.^[28] There was a notable increase in DLX5 on the osteogenic microgel side of the scaffold. Taken together, these data indicate the ability of the osteogenic microgels to maintain an osteogenic phenotype, while both microgels could support GAG deposition in the absence of exogenous cues.

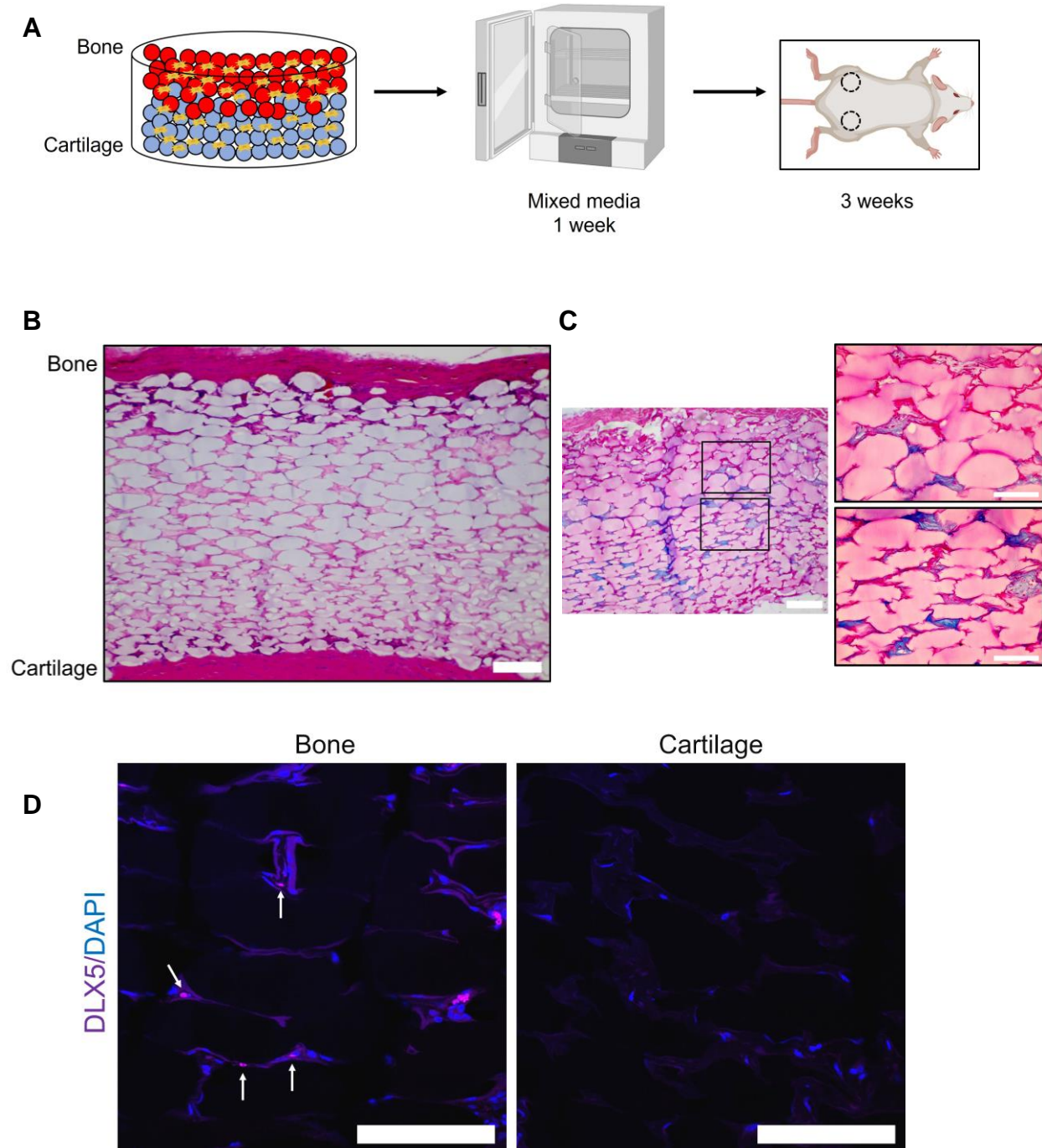


Figure 4.6 Subfascial implantation of bilayer scaffolds. (A) Bilayer scaffolds were preconditioned in mixed media for 1 week followed by subfascial implantation in NSG mice for 3 weeks. (B) H&E demonstrates robust ECM deposition and infiltration on both sides of the scaffold. Scale bar represents 200 μm . (C) Alcian blue is positive on both

sides of the scaffold. Primary scale bar represents 200 μm . Inset scale bar represents 100 μm . **(D)** Positive DLX5 staining is only present on the bone side of the microgel scaffold (white arrows). Scale bar represents 100 μm .

4.4 Discussion

Microgels are an increasingly popular scaffold choice in tissue engineering due to their inherent void space, modularity, and tunability, making them an ideal choice for heterogeneous structures such as osteochondral tissue found at the bone-cartilage interface.^[29] Furthermore, the modular nature of microgels and use of a single annealing step permits microgels to seamlessly integrate between scaffold layers, creating a strong interface. In this work, we designed osteogenic and chondrogenic microgels to promote lineage-specific differentiation of MSCs. Previously, studies have combined microgels with bone ink,^[12] as well as tuned microgel adhesivity,^[14] to promote formation of osteochondral tissue. To our knowledge, this is the first study that controls microgel stiffness with the combination of bioactive peptides to promote osteochondral differentiation of MSCs. Furthermore, these studies represent the first description of spatial transcriptomics to investigate MSC gene expression throughout an osteochondral microgel scaffold. This work expands upon the available tools to promote MSC differentiation and offers insight for how microgel tunability can be harnessed to create complex scaffolds.

Chondrogenic microgels had a Young's modulus of ~ 12 kPa which is in the "intermediate" stiffness range (~ 3 -30 kPa), previously reported to drive chondrogenesis.^[30,31] Chondrogenic microgels also contained the N-cadherin mimetic

peptide, HAVDI, which has been shown to promote chondrogenesis.^[22,23] N-cadherin is a transmembrane protein that directs cell-cell binding during mesenchymal condensation expressed early on in chondrogenesis.^[32,33] By replicating these early cell-cell interactions, in combination with a soft mechanical moduli, these microgels recapitulate the environment wherein MSCs undergo chondrogenesis. When compared to bulk gels with the same stiffness and peptide formulation, chondrogenic microgels outperformed bulk hydrogels in both GAG and collagen production. These data showcase the benefit of the inherent void space present in microgels.

Osteogenic microgels had a Young's modulus of ~ 51 kPa which is in the (~30-100 kPa) stiffness range of uncalcified osseous matrix reported to drive osteogenic differentiation.^[34,35] The microgels were functionalized with RGD peptide to promote adhesion and DWIVA, a BMP-2 knuckle peptide. BMP-2 signaling is vital in skeletal development and bone homeostasis and induces MSC osteogenesis.^[36,37] ALP activity, which is an early marker of osteogenesis, was higher in the microgels on weeks 1 and 3 compared to bulk gels. However, bulk gels outperformed microgels in calcium deposition at the 3-week timepoint. However, given the overall low levels of calcium, which is a late-stage marker of osteogenesis, and the high levels of ALP at week 3, it is likely that not enough time had passed to allow for significant mineral deposition.^[26] The increased calcium in the bulk gels could be attributed to the bulk gels retaining more calcium from the media. We also assessed osteocalcin deposition as another late-stage marker of osteogenesis,^[27] which was abundant throughout the microgel scaffold compared to bulk gels. Overall, these data demonstrate the successful fabrication of osteogenic and

chondrogenic microgels that outperform their bulk counterparts for lineage-specific differentiation.

When osteogenic and chondrogenic microgels were formed into a bilayer scaffold and seeded with MSCs, we observed significant trends in protein deposition as a function of microgel type. Osteocalcin was more apparent on the osteogenic microgel side of the scaffold. Meanwhile aggrecan, a marker of chondrogenesis,^[23,38] was enriched on the chondrogenic side of the scaffold. Interestingly, collagen X, a marker of hypertrophic chondrocytes and endochondral ossification, was more apparent on the osteogenic side of the scaffold.^[39,40] The presence of collagen X, combined with the presence aggrecan and osteocalcin, indicates that both sides were undergoing endochondral ossification to some extent. This could be due to the mixed media providing both osteogenic and chondrogenic stimuli for the duration of the 3 weeks. However, the osteogenic and chondrogenic microgels promoted their phenotypes to a greater extent on their respective scaffold sides. These data illustrate that while the soluble cues from the mixed media were a predominant force in guiding MSC differentiation, the instructive cues from the microgels were able to guide MSCs toward their intended pathway. In addition to immunofluorescent staining, H&E staining revealed robust ECM deposition between the microgel layers, highlighting the ability of microgels to form a continuous interface. On the chondrogenic side of the scaffold, we observed greater microgel compression due to the lower mechanical modulus, along with increased cellular aggregation due to the minimal adhesion of HAVDI. The combination of microgel stiffness and lineage-specific peptides provide an exciting opportunity to direct MSC differentiation.

Upon analysis of spatially restricted gene expression, we further confirmed the presence of increased osteogenic expression on the bone side and greater chondrogenic expression on the cartilage side of the scaffold. Osteogenic factors were most highly expressed in the bone edge except for *Runx2*. However, this could be due to *Runx2* expression being downregulated in mature osteoblasts.^[41] Conversely, the upregulation of *Runx2* in the cartilage center could be an indicator of hypertrophic chondrocytes undergoing endochondral ossification.^[42] Chondrogenic genes were most upregulated in the center and cartilage center, with *Sox9* most highly expressed in the cartilage center. The upregulation of chondrogenic genes in the center could also be influenced by transport limitations, with hypoxic conditions favoring chondrogenesis.^[43] RGD, shown to increase chondrogenesis of MSCs at low concentrations, could explain the strong chondrogenic expression in the center of the scaffold.^[23] Surprisingly, while the cartilage edge strongly downregulated *Runx2*, the chondrogenic genes were not as highly expressed. This could be a result of paracrine signaling, cell migration from the surface of the osteogenic half to the surface of the chondrogenic half, or decreased cell-biomaterial interaction at the edge of the scaffold. Interestingly, gene expression at the bone edge was different from the bone center. This could again be due to paracrine signaling, or the increased cell spreading along the outside of the scaffold.

Finally, when implanted subfascially after one week of preconditioning in mixed media, the bilayer scaffolds were able to induce DLX5 staining on the bone side of the scaffold and GAG deposition throughout the bilayer construct. This indicates that after one week of preconditioning in mixed media, the osteogenic microgels were able to promote osteogenesis without continued exogenous cues. There is a lack of GAG

deposition along both edges of the scaffold, most likely due to endogenous cell migration preventing deposition from MSCs. Future work would include implanting this construct in an osteochondral defect *in vivo*, where the natural tissue environment would provide cues that work synergistically with the microgels.

4.5 Conclusion

We fabricated osteogenic and chondrogenic microgels through the addition of instructive peptides and modulation of stiffness. The microgels outperformed their bulk counterparts in promoting MSC differentiation and permitted robust cell proliferation and ECM deposition. We harnessed the modularity of microgels to make a bilayer scaffold capable of spatially instructing MSCs with a continuous interface between the layers. These studies demonstrate the potential of microgels for engineering heterogeneous scaffolds.

4.6 References

- [1] H. Long, Q. Liu, H. Yin, K. Wang, N. Diao, Y. Zhang, J. Lin, A. Guo, Prevalence Trends of Site-Specific Osteoarthritis From 1990 to 2019: Findings From the Global Burden of Disease Study 2019, *Arthritis Rheumatol.* 74 (2022) 1172–1183.
- [2] S.I.M. Lepage, N. Robson, H. Gilmore, O. Davis, A. Hooper, S. St. John, V. Kamesan, P. Gelis, D. Carvajal, M. Hurtig, T.G. Koch, Beyond Cartilage Repair: The Role of the Osteochondral Unit in Joint Health and Disease, *Tissue Eng., Part B.* 25 (2019) 114–125.
- [3] A.R. Martín, J.M. Patel, H.M. Zlotnick, J.L. Carey, R.L. Mauck, Emerging therapies for cartilage regeneration in currently excluded ‘red knee’ populations, *Npj Regener. Med.* 4 (2019) 12.
- [4] D.J. Huey, J.C. Hu, K.A. Athanasiou, Unlike Bone, Cartilage Regeneration Remains Elusive, *Science.* 338 (2012) 917–921. <https://doi.org/10.1126/science.1222454>.
- [5] W. Wei, H. Dai, Articular cartilage and osteochondral tissue engineering techniques: Recent advances and challenges, *Bioact. Mater.* 6 (2021) 4830–4855.
- [6] M.F. Pittenger, A.M. Mackay, S.C. Beck, R.K. Jaiswal, R. Douglas, J.D. Mosca, M.A. Moorman, D.W. Simonetti, S. Craig, D.R. Marshak, Multilineage Potential of Adult Human Mesenchymal Stem Cells, *Science.* 284 (1999) 143–147.
- [7] A. Wilson, A. Webster, P. Genever, Nomenclature and heterogeneity: consequences for the use of mesenchymal stem cells in regenerative medicine, *Regener. Med.* 14 (2019) 595–611.

- [8] S. Barui, D. Ghosh, C.T. Laurencin, Osteochondral regenerative engineering: challenges, state-of-the-art and translational perspectives, *Regener. Biomater.* 10 (2023) rbac109.
- [9] J.M. Lowen, J.K. Leach, Functionally Graded Biomaterials for Use as Model Systems and Replacement Tissues, *Adv. Funct. Mater.* 30 (2020) 1909089.
- [10] F. Han, F. Zhou, X. Yang, J. Zhao, Y. Zhao, X. Yuan, A pilot study of conically graded chitosan-gelatin hydrogel/PLGA scaffold with dual-delivery of TGF- β 1 and BMP-2 for regeneration of cartilage-bone interface, *J. Biomed. Mater. Res.* 103 (2015) 1344–1353.
- [11] J.L. Guo, Y.S. Kim, G.L. Koons, J. Lam, A.M. Navara, S. Barrios, V.Y. Xie, E. Watson, B.T. Smith, H.A. Pearce, E.A. Orchard, J.J.J.P. van den Beucken, J.A. Jansen, M.E. Wong, A.G. Mikos, Bilayered, peptide-biofunctionalized hydrogels for in vivo osteochondral tissue repair, *Acta Biomater.* 128 (2021) 120–129.
- [12] G.K. Jalandhra, T.G. Molley, T. Hung, I. Roohani, K.A. Kilian, In situ formation of osteochondral interfaces through “bone-ink” printing in tailored microgel suspensions, *Acta Biomater.* (2022) S1742706122005293.
- [13] C. Schaeffer, B.N. Pfaff, N.J. Cornell, L.S. Salopek, S. Shan, J. Viyar, W. Omesiete, D.R. Griffin, P.S. Cottler, B.R. DeGeorge, Injectable Microannealed Porous Scaffold for Articular Cartilage Regeneration, *Ann. Plast. Surg.* 84 (2020) S446–S450.
- [14] P. Xia, S. Yan, G. Li, J. Yin, Preparation of Assemblable Chondral and Subchondral Bone Microtissues for Osteochondral Tissue Engineering, *ACS Appl. Mater. Interfaces.* 14 (2022) 12089–12105.

- [15] C. Gegg, F. Yang, Spatially patterned microribbon-based hydrogels induce zonally-organized cartilage regeneration by stem cells in 3D, *Acta Biomater.* 101 (2020) 196–205.
- [16] B. Sharma, C.G. Williams, T.K. Kim, D. Sun, A. Malik, M. Khan, K. Leong, J.H. Elisseeff, Designing Zonal Organization into Tissue-Engineered Cartilage, *Tissue Eng.* 13 (2007) 405–414.
- [17] K.A. Gultian, R. Gandhi, K. DeCesari, V. Romiyo, E.P. Kleinbart, K. Martin, P.M. Gentile, T.W.B. Kim, S.L. Vega, Injectable hydrogel with immobilized BMP-2 mimetic peptide for local bone regeneration, *Front. Biomater. Sci.* 1 (2022) 948493.
- [18] S.S. Ho, A.T. Keown, B. Addison, J.K. Leach, Cell Migration and Bone Formation from Mesenchymal Stem Cell Spheroids in Alginate Hydrogels Are Regulated by Adhesive Ligand Density, *Biomacromolecules.* 18 (2017) 4331–4340.
- [19] J.M. de Rutte, J. Koh, D. Di Carlo, Scalable High-Throughput Production of Modular Microgels for In Situ Assembly of Microporous Tissue Scaffolds, *Adv. Funct. Mater.* 29 (2019) 1900071.
- [20] J.M. Lowen, G.C. Bond, K.H. Griffin, N.K. Shimamoto, V.L. Thai, J.K. Leach, Multisized Photoannealable Microgels Regulate Cell Spreading, Aggregation, and Macrophage Phenotype through Microporous Void Space, *Adv. Healthcare Mater.* (2023) 2202239.
- [21] L. Nichele, V. Persichetti, M. Lucidi, G. Cincotti, Quantitative evaluation of ImageJ thresholding algorithms for microbial cell counting, *OSA Continuum.* 3 (2020) 1417.

- [22] L. Bian, M. Guvendiren, R.L. Mauck, J.A. Burdick, Hydrogels that mimic developmentally relevant matrix and N-cadherin interactions enhance MSC chondrogenesis, *Proc. Natl. Acad. Sci. U.S.A.* 110 (2013) 10117–10122.
- [23] S.L. Vega, M.Y. Kwon, K.H. Song, C. Wang, R.L. Mauck, L. Han, J.A. Burdick, Combinatorial hydrogels with biochemical gradients for screening 3D cellular microenvironments, *Nat. Commun.* 9 (2018) 614.
- [24] L. Oliver-Cervelló, H. Martín-Gómez, N. Mandakhbayar, Y. Jo, E.A. Cavalcanti-Adam, H. Kim, M. Ginebra, J. Lee, C. Mas-Moruno, Mimicking Bone Extracellular Matrix: From BMP-2-Derived Sequences to Osteogenic-Multifunctional Coatings, *Adv. Healthcare Mater.* 11 (2022) 2201339.
- [25] B.P. Hung, J.N. Harvestine, A.M. Saiz, T. Gonzalez-Fernandez, D.E. Sahar, M.L. Weiss, J.K. Leach, Defining hydrogel properties to instruct lineage- and cell-specific mesenchymal differentiation, *Biomaterials.* 189 (2019) 1–10.
- [26] F. Yang, C.G. Williams, D. Wang, H. Lee, P.N. Manson, J. Elisseeff, The effect of incorporating RGD adhesive peptide in polyethylene glycol diacrylate hydrogel on osteogenesis of bone marrow stromal cells, *Biomaterials.* 26 (2005) 5991–5998.
- [27] Y.-T. Tsao, Y.-J. Huang, H.-H. Wu, Y.-A. Liu, Y.-S. Liu, O. Lee, Osteocalcin Mediates Biomineralization during Osteogenic Maturation in Human Mesenchymal Stromal Cells, *Int. J. Mol. Sci.* 18 (2017) 159.
- [28] J.N. Harvestine, T. Gonzalez-Fernandez, A. Sebastian, N.R. Hum, D.C. Genetos, G.G. Loots, J.K. Leach, Osteogenic preconditioning in perfusion bioreactors improves vascularization and bone formation by human bone marrow aspirates, *Sci. Adv.* 6 (2020) eaay2387.

- [29] A.C. Daly, L. Riley, T. Segura, J.A. Burdick, Hydrogel microparticles for biomedical applications, *Nat. Rev. Mater.* 5 (2020) 20–43.
- [30] T. Wang, J.H. Lai, F. Yang, Effects of Hydrogel Stiffness and Extracellular Compositions on Modulating Cartilage Regeneration by Mixed Populations of Stem Cells and Chondrocytes *In Vivo*, *Tissue Eng., Part A.* 22 (2016) 1348–1356.
- [31] T. Roncada, R. Bonithon, G. Blunn, M. Roldo, Soft substrates direct stem cell differentiation into the chondrogenic lineage without the use of growth factors, *J. Tissue Eng.* 13 (2022) 204173142211221.
- [32] S. Tavella, P. Raffo, C. Tacchetti, R. Cancedda, P. Castagnola, N-CAM and N-Cadherin Expression during in Vitro Chondrogenesis, *Exp. Cell Res.* 215 (1994) 354–362.
- [33] S.A. Oberlender, R.S. Tuan, Spatiotemporal Profile of N-Cadherin Expression in the Developing Limb Mesenchyme, *Cell Adhes. Commun.* 2 (1994) 521–537.
- [34] A.J. Engler, S. Sen, H.L. Sweeney, D.E. Discher, Matrix Elasticity Directs Stem Cell Lineage Specification, *Cell.* 126 (2006) 677–689.
- [35] N. Huebsch, E. Lippens, K. Lee, M. Mehta, S.T. Koshy, M.C. Darnell, R.M. Desai, C.M. Madl, M. Xu, X. Zhao, O. Chaudhuri, C. Verbeke, W.S. Kim, K. Alim, A. Mammoto, D.E. Ingber, G.N. Duda, D.J. Mooney, Matrix elasticity of void-forming hydrogels controls transplanted-stem-cell-mediated bone formation, *Nat. Mater.* 14 (2015) 1269–1277.
- [36] V. Rosen, BMP2 signaling in bone development and repair, *Cytokine Growth Factor Rev.* 20 (2009) 475–480.

- [37] S.S. Ho, N.L. Vollmer, M.I. Refaat, O. Jeon, E. Alsberg, M.A. Lee, J.K. Leach, Bone Morphogenetic Protein-2 Promotes Human Mesenchymal Stem Cell Survival and Resultant Bone Formation When Entrapped in Photocrosslinked Alginate Hydrogels, *Adv. Healthcare Mater.* 5 (2016) 2501–2509.
- [38] F. Barry, R.E. Boynton, B. Liu, J.M. Murphy, Chondrogenic Differentiation of Mesenchymal Stem Cells from Bone Marrow: Differentiation-Dependent Gene Expression of Matrix Components, *Exp. Cell Res.* 268 (2001) 189–200.
- [39] G. Shen, The role of type X collagen in facilitating and regulating endochondral ossification of articular cartilage, *Orthod. Craniofac. Res.* 8 (2005) 11–17.
- [40] W.T. Grant, G.J. Wang, G. Balian, Type X collagen synthesis during endochondral ossification in fracture repair., *J. Biol. Chem.* 262 (1987) 9844–9849.
- [41] T. Komori, Regulation of Proliferation, Differentiation and Functions of Osteoblasts by Runx2, *Int. J. Mol. Sci.* 20 (2019) 1694.
- [42] K. Nagata, H. Hojo, S.H. Chang, H. Okada, F. Yano, R. Chijimatsu, Y. Omata, D. Mori, Y. Makii, M. Kawata, T. Kaneko, Y. Iwanaga, H. Nakamoto, Y. Maenohara, N. Tachibana, H. Ishikura, J. Higuchi, Y. Taniguchi, S. Ohba, U. Chung, S. Tanaka, T. Saito, Runx2 and Runx3 differentially regulate articular chondrocytes during surgically induced osteoarthritis development, *Nat. Commun.* 13 (2022) 6187.
- [43] C. Merceron, C. Vinatier, S. Portron, M. Masson, J. Amiaud, L. Guigand, Y. Chérel, P. Weiss, J. Guicheux, Differential effects of hypoxia on osteochondrogenic potential of human adipose-derived stem cells, *Am. J. Physiol. Cell Physiol.* 298 (2010) C355–C364.

Chapter 5: Conductive microgel annealed scaffolds enhance myogenic potential of myoblastic cells

5.1 Introduction

Muscle tissue engineering is a promising strategy for repairing large muscle wounds such as volumetric muscle loss (VML) that surpass the body's innate healing ability. VML and other musculoskeletal disorders, which affect over 500 million people worldwide, may result in reduced mobility (and in some cases disability) and significant economic burden of billions of dollars each year.^[1,2] The current gold standard of treatment is autologous muscle graft which has negative side effects of donor site morbidity and atrophy. Muscle tissue engineering seeks to address these shortcomings by providing alternative strategies for healing.^[3,4] An engineered tissue approach has numerous and specific requirements to recapitulate muscle's hierarchical, anisotropic, elastic, vascularized, and innervated properties, and VML injuries also face the challenge of being irregularly shaped.

Synthetic and natural polymers have been developed for specific applications in muscle tissue engineering including aligned structures to recapitulate muscle isotropy, elastic materials to mimic the contractile function of muscle tissue, and hydrogels for use as volume fillers and cell delivery vehicles. Hydrogels are a popular biomaterial for use in cell and drug delivery due to their tunability and viscoelastic behavior which mimics that of native tissues.^[5] Bulk hydrogels have been widely studied for use in muscle tissue engineering due to their ease of handling, cell-friendly nature, and extensive control of their biophysical properties. However, bulk hydrogels are typically nanoporous in nature,

which limits cell-cell interaction and cell migration until the surrounding extracellular matrix (ECM) is degraded. Microgels are emerging as a promising hydrogel platform due to their modularity and microporosity.^[6] Unlike conventional nanoporous bulk hydrogels, the inherent void space between microgels permits immediate cell migration without the need to first remodel the local environment. Furthermore, their ability to be cryopreserved after fabrication and then injected increases their translational potential for the clinic.^[7,8] A multitude of studies have examined bulk hydrogels for muscle tissue engineering,^[5] yet there are limited examples on the use of microgels. In one example, microgels were mixed with silver nanoparticles to form a conductive mixture that conferred electric signals across *ex vivo* tissues, yet their influence on muscle cell regeneration was not reported.^[9]

Bioelectricity is a potent but understudied stimulus that plays a key role in muscle tissue formation and function.^[10] Biomaterials that possess bioelectric potential (i.e., conductivity) are an exciting strategy to advance the field of tissue engineering. Electrically conductive biomaterials are gaining popularity for such applications owing to their ability to direct cell differentiation and maturation, particularly for nerve^[11] and cardiac tissue repair.^[12] Synthetic conductive polymers such as polypyrrole, polyaniline, and PEDOT:PSS (poly(3,4-ethylenedioxythiophene) polystyrene sulfonate)) or carbon-based materials (e.g., carbon nanotubes, graphene, etc.) are frequently used to imbue hydrogels with electroactive properties.^[10,13] For example, synthetic electrospun fibers were developed for muscle tissue engineering that contained either polyaniline blends^[14,15] or PEDOT:PSS nanoparticles.^[16] Moreover, polypyrrole was incorporated into directionally aligned collagen scaffolds to instruct myoblast behavior.^[17] While these reports include

both electrical and physical cues to promote cell differentiation toward myogenesis, the interplay between conductivity and scaffold porosity has yet to be directly interrogated.

Herein, we aim to combine the microporosity of microgel annealed scaffolds with the conductivity of PEDOT:PSS to enhance myogenic differentiation. We demonstrate a conductive microgel platform which outperforms both conductive bulk degradable and non-conductive scaffolds in promoting myogenic differentiation. We generate microgel scaffolds with a conductivity $\sim 3.5 \times 10^{-6}$ S/cm and a compressive modulus ~ 28 kPa, parameters characteristic of native muscle tissue. Cell viability and scaffold stiffness is not altered by the addition of PEDOT:PSS, and conductive microgels can be annealed into a contiguous scaffold. Gene and protein expression indicative of myotube maturation is upregulated in our conductive microgel scaffolds when seeded with murine C2C12 myoblasts and human skeletal muscle derived cells, suggesting the importance of both electroactivity and microporosity for muscle regeneration.

5.2 Materials and Methods

5.2.1 Microgel synthesis

Microgels were fabricated using a previously described microfluidic device^[18] that was subsequently adapted by our group.^[7] For the production of nondegradable microgels, the aqueous phase consisted of 10 kDa 8-arm PEG-vinyl sulfone (PEG-VS) (JenKem, Plano, TX) and RGD (Ac-RGDSPGERCG-NH₂, Genscript, Piscataway, NJ) in 100 mM HEPES buffer (N-2-hydroxyethylpiperazine-N'-2-ethanesulfonic acid, pH 5.25, Sigma, St. Louis, MO) mixed with 3.5 kDa PEG-DT (JenKem) dissolved in diH₂O with or without PEDOT:PSS (PH1000, Ossila, Sheffield, UK). The final microgel concentrations

were 4.5 mM PEG-VS, 10.8 mM PEG-DT, 1 mM RGD, and 0.25 wt% PEDOT:PSS. The oil phase consisted of Novec 7500 Oil and 0.75 wt% Picosurf (Sphere Fluidics, Cambridge, UK). After exiting the device, microgels were combined with a solution of 1 v/v% triethylamine (TEA, Sigma) in Novec 7500 Oil using a Y-junction (IDEX Health and Science, Oak Harbor, WA) and left at room temperature overnight to ensure complete crosslinking. Microgels were cleaned to remove residual oil and surfactant as described.^[7]

5.2.2 Annealing microgels

Microgels were annealed as previously described.^[7] Briefly, microgels were suspended in an annealing solution consisting of additional crosslinker in HEPES containing 0.4% VA-086 photoinitiator (FUJIFULM Wako Chemicals, Richmond, VA) equal to the aggregate volume of microgels. After incubating for 1 min, the microgels were spun down for 3 min at 14,000 × g. The supernatant was removed and microgels were optionally mixed with cells before plating in the desired mold. The microgel slurry was then exposed to UV light (20 mW/cm², 320-500 nm, Omnicure S2000) for 2 min to form annealed scaffolds.

5.2.3 Bulk degradable gel synthesis

GPQ-A (GCRDGPQGIAGQDRCG, Genscript) was substituted for PEG-DT to permit matrix metalloproteinase (MMP)-mediated degradation. The final concentrations were 8 mM PEG-VS, 19.2 mM GPQ-A, 1 mM RGD, and 0.25 wt% PEDOT:PSS. A precursor solution consisting of PEG-VS, RGD, and optionally PEDOT:PSS in HEPES (25 mM, pH 7.2) at 2X concentration was combined with cells and pipetted into the desired

mold. An equal volume of 2X GPQ-A (pH 8.3) in media was then mixed in by pipetting up and down. The gels were incubated at 37°C for 15 min before being transferred to a well plate.

5.2.4 Conductivity testing

Annealed microgels were electrically characterized as described previously.^[19] Briefly, 6 mm scaffolds were constrained by a PDMS mold and sandwiched between two brass plates. The sandwich was then stabilized between the jaws of a tabletop angle vise using PDMS blocks as a barrier between the plate and the jaw. One brass plate was connected to a power supply (BK Precision 1735A, Yorba Linda, CA) using alligator clips and the other plate was connected to a multimeter (SparkFun Electronics, Niwot, CO) to measure output current. Voltages ranging from 100 to 500 mV, chosen to avoid the electrolysis of water, were applied to obtain current-voltage curves. After testing, hydrogel diameter and thickness were measured with calipers and hydrogel cross-sectional area was calculated. Current-voltage curves were analyzed for linearity and datasets with an R^2 value ≥ 0.9 were accepted for resistance calculations. Conductivity was calculated using Pouillet's law (**Equation 5.1**). Hydrogels for conductivity testing were stored in ultrapure water to eliminate the confounding effects of ions in other solutions.

Equation 5.1:

$$\sigma = \frac{t}{RA}$$

Where σ is conductivity in S/cm, t is thickness of the hydrogel (cm), R is resistance (Ω), and A is cross-sectional area (cm^2).

5.2.5 Mechanical testing

Bulk hydrogel scaffolds were loaded onto a Discovery HR2 Rheometer (TA Instruments, New Castle, DE) with a stainless steel, cross hatched, 8 mm plate geometry. An oscillatory strain sweep ranging from 0.004% to 4% strain was performed on each gel using an initial 0.3N axial force to obtain the linear viscoelastic region (LVR) before failure. Individual microgels were examined using a MicroTester (CellScale, Waterloo ON, Canada). Microgels were loaded onto an anvil in a water bath filled with PBS. The microgels were then compressed to half their diameter by a stainless-steel platen attached to a tungsten rod over 30 s. Displacement and force were traced via MicroTester software. The slope of the linear region of the compressive modulus versus nominal strain graph was recorded as the calculated modulus.^[7,20]

5.2.6 Cell culture

C2C12 murine myoblasts (CRL-1772, Lot #70013341, ATCC, Manassas, VA) were cultured in DMEM (Thermo Fisher Scientific, Walham, MA) supplemented with 10% FBS (GenClone, San Diego, CA) and 1% Penicillin-Streptomycin (P/S, Gemini Bio Products, West Sacramento, CA) (DMEM-G) in standard culture conditions (i.e., 37°C, 5% CO₂). Cultures were maintained until <70% confluent to prevent myoblast differentiation. Differentiation media was prepared by supplementing DMEM with 2% heat-inactivated horse serum (Thermo Fisher Scientific) and 1% FBS (DMEM-D). C2C12s were seeded in tissue culture plastic flasks at 5,000 cells/cm². Cells were seeded to achieve a final concentration of 50,000 cells per gel. Cells seeded into gels were handled with DMEM-G and cell-laden scaffolds were cultured in 24-well plates containing

DMEM-G for approximately 24 h (0d) before transferring to a fresh well plate containing DMEM-D (1d). Metabolic activity and differentiation of myoblasts in microgel and bulk degradable scaffolds were assessed at 3 and 7 days. Primary human skeletal muscle derived cells (skMDCs) and all associated cell culture reagents were purchased from Cook Myosite (Pittsburgh, PA). The donor was a 29-year-old Caucasian male with BMI 29 and no history of smoking or diabetes (SK-1111-P01547-29M). Cells were handled according to the manufacturer's instructions. Briefly, cells were expanded in MyoTonic™ Basal Medium supplemented with MyoTonic™ Growth Supplement. Cells were seeded into microgel scaffolds at 100,000 cells per scaffold. Annealed scaffolds were maintained in growth medium for 1 days before transferring to MyoTonic™ Differentiation media. Muscle cell differentiation and myotube formation was assessed at 1, 3, and 7 d, and the medium conditioned by these cells was collected for later use.

5.2.7 Biochemical assessment of metabolic activity and proliferation

Metabolic activity of C2C12s in microgel scaffolds was assessed using the alamarBlue™ Cell Viability Reagent according to the manufacturer's instruction (Thermo Fisher Scientific). In short, cell-laden scaffolds were transferred to fresh DMEM-D with 1:10 alamarBlue reagent™ and incubated at 37°C for 2 h before analysis. Results were normalized to the DNA content measured using the Quant-iT PicoGreen dsDNA Kit (Thermo Fisher Scientific).

5.2.8 Immunostaining

Scaffolds were fixed in 4% paraformaldehyde for 1 h and incubated in blocking buffer composed of 10% goat serum (MP Bio, Santa Ana, CA) and 10 mg/mL Bovine Serum Albumin (BSA, Sigma) for 30 min at room temperature. Constructs were then incubated with myosin heavy chain antibody conjugated with Alexa Fluor 488 (1:50; Santa Cruz Biotechnology, 376157) and myogenin antibody conjugated with Alexa Fluor 680 (1:50, Santa Cruz Biotechnology, 12732). Samples were rinsed with PBS and incubated with DAPI (1:500 in PBS; ThermoFisher Scientific) for 10 min. Z-stacks were taken on a confocal microscope (Leica Stellaris 5), and max projections were used to illustrate cell morphology throughout the scaffolds.

5.2.9 qPCR

Total RNA was isolated from cells using TRIzol reagent (ThermoFisher Scientific) according to the manufacturer's instructions. RNA quality and quantity was measured using a Nanodrop One[®] instrument (ThermoFisher Scientific) before reverse transcribing to cDNA with the QuantiTect Reverse Transcription kit (Qiagen, Hilden, Germany). All cDNA samples were diluted with PCR-grade ultrapure water to 12.5 ng/ μ L prior to qPCR. qPCR was performed using Taq PCR Master Mix kit (Qiagen), TaqMan Gene Expression Assay probes (Cat. 4331182, Thermo Fisher Scientific), and a QuantStudio[™] 6 instrument (Thermo Fisher Scientific). Samples were activated at 94°C for 3 min, followed by 40 cycles of 94°C for 30 s, 60°C for 30 s, and 72°C for 1 min, and underwent a final annealing step at 72°C for 10 min.

C2C12 expression of the myogenic differentiation markers MyoD (Myod1, Mm00440387_m1), myogenin (Myog, Mm00446194_m1) and myosin heavy chain (Myh7, Mm00600555_m1) was interrogated at 3 and 7d. Myogenic differentiation and maturation of skMDC was assessed via expression of the same genes (MyoD (Myod1, Hs00159528_m1), myogenin (Myog, Hs01072232_m1), myosin heavy chain (Myh7, Hs01110632_m1)) at 1, 3, and 7d to capture potential differences at earlier timepoints. All genes were normalized to the housekeeping gene GAPDH (Mm99999915_g1, Hs02786624_g1) to yield ΔCt . Gene expression of C2C12s was further normalized to the 0.00% PEDOT:PSS group at 3d to calculate $\Delta\Delta\text{Ct}$. Expression of skMDCs was normalized to that of cells taken prior to microgel seeding. Fold change was calculated using the $2^{-\Delta\Delta\text{Ct}}$ method.

5.2.10 Characterization of skMDC secreted factors

Media conditioned by the skMDCs in microgels was collected on 1, 3, and 7d and frozen at -80°C until analyzed using a Human Cytokine Array C5 kit (Ray Biotech, San Diego, CA) according to the manufacturer's instructions. Blots were imaged using an Odyssey® XF Imaging System (LI-COR, Lincoln, NE) and normalized against MyoTonic™ Differentiation media to account for myokines present in the media alone. Data were analyzed using ImageJ with the Protein Array Analyzer plugin.^[21]

5.2.11 Statistical analysis

Data are presented as means \pm standard deviation. GraphPad Prism 9 software was used to plot all graphs and perform statistical testing. Statistically significant groups

are denoted by two conventions: asterisks were used to denote differences when using a t-test or 1-way ANOVA, whereas letters were used when a 2-way ANOVA was employed. Groups denoted by different letters are statistically different. Datasets with additional interactions were analyzed using MATLAB.

5.3 Results

5.3.1 PEG microgels can be annealed into conductive scaffolds with mechanical properties appropriate for muscle tissue engineering

PEG microgel were fabricated as previously described and covalently modified with RGD to facilitate cell adhesion.^[7] PEDOT:PSS was optionally introduced into the aqueous phase of microgel fabrication such that the final concentration within each microgel was 0.25 wt% (**Figure 5.1A**). Microgels were successfully annealed into 8 mm scaffolds with good retention of PEDOT:PSS, as depicted in **Figure 1B**. The addition of PEDOT:PSS caused a significant increase in annealed scaffold conductivity from $1.58 \pm 0.68 \times 10^{-6}$ S/cm to $3.52 \pm 0.96 \times 10^{-6}$ S/cm ($p < 0.01$; **Figure 5.1C**). Next, we assessed if addition of PEDOT:PSS affected the mechanical properties of the microgels and annealed scaffolds. We measured the compressive modulus of individual microgels on a MicroTester (**Figure 5.1D**) which was ~ 28 kPa for both groups. Using Hooke's law for isotropic materials and a Poisson's ratio of approximately 0.5, the storage modulus of each microgel is estimated to be 10 kPa.^[22] Since cells interact directly with individual microgels, these mechanical properties were considered appropriate for muscle tissue engineering applications.^[23] The storage modulus of annealed scaffolds also did not significantly differ between groups, indicating that PEDOT:PSS did not affect annealing

ability (**Figure 5.1E**). Together, these data illustrate successful incorporation of PEDOT:PSS into PEG microgels without altering mechanical properties. The microgels can be annealed to form scaffolds with decoupled electrical and mechanical properties suitable for muscle tissue engineering.

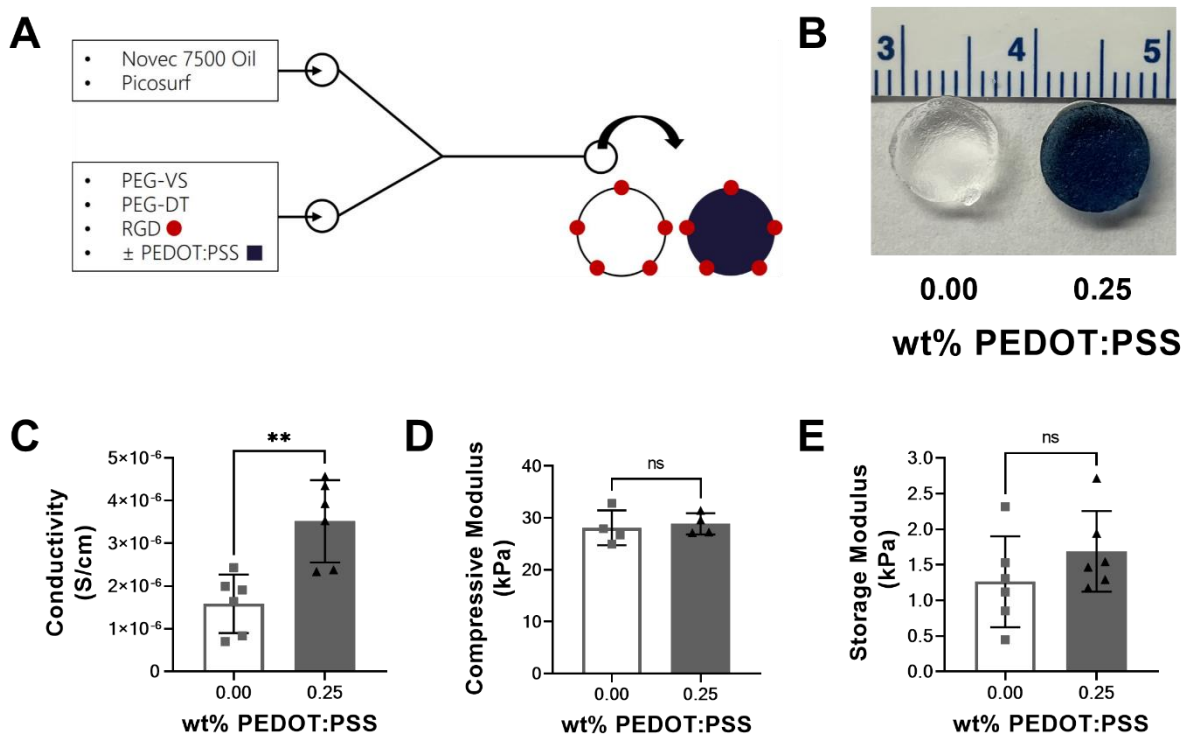


Figure 5.1 The electrical and mechanical properties of conductive microgels can be decoupled. **(A)** Schematic of PEG microgel modification and PEDOT:PSS incorporation. **(B)** Gross images of 8 mm scaffolds demonstrate successful annealing with UV light and retention of PEDOT:PSS. **(C)** Scaffolds containing PEDOT:PSS were significantly more conductive than non-conductive controls (n=6). By contrast, PEDOT:PSS did not affect **(D)** the compressive modulus of individual microgels (n=4) or **(E)** the storage modulus of annealed microgel scaffolds (n=6). Groups were compared using a two-tailed t-test where **p≤0.01 and ns = not significant.

5.3.2 Conductive microgel scaffolds support C2C12 myoblast metabolic activity

C2C12 mouse myoblasts were seeded into annealed microgel scaffolds or bulk degradable hydrogels as a control. After 3 and 7d, metabolic activity of the cells was measured with the alamarBlue assay, the results of which were normalized to DNA content. Cells in conductive annealed microgel scaffolds exhibited greater proliferation at 3d than those in the non-conductive control, evidenced by the increase in DNA content (**Figure 5.2A**). However, the metabolic activity of cells on 3d appeared lower in the conductive group, though results were not significant (**Figure 5.2B**). This may indicate the conductive microgels' ability to promote C2C12 differentiation, which is associated with lower metabolic activity.^[24] There were no changes in DNA content or metabolic activity of myoblasts in annealed microgel scaffolds at 7d.

Conversely, C2C12s grown in bulk degradable gels had no difference in DNA content or metabolic activity on 3d, regardless of PEDOT:PSS content. On 7d, however, PEDOT:PSS-containing bulk gels exhibited greater DNA content, indicating that conductive substrates may better support cell viability (**Figure 5.2C**). Metabolic activity on the bulk degradable gels was low at 3d, and the reduction in activity on the conductive gels at 7d compared to the non-conductive controls is also believed to be suggestive of cell differentiation (**Figure 5.2D**).

Overall, these data suggest microgels containing PEDOT:PSS support increased proliferation and differentiation of C2C12s compared to microgels without the conductive additive. Furthermore, these data demonstrate the advantage of microgel annealed

scaffolds in supporting cell viability, proliferation, and metabolic activity compared to nanoporous bulk hydrogels that are frequently used for tissue engineering studies.

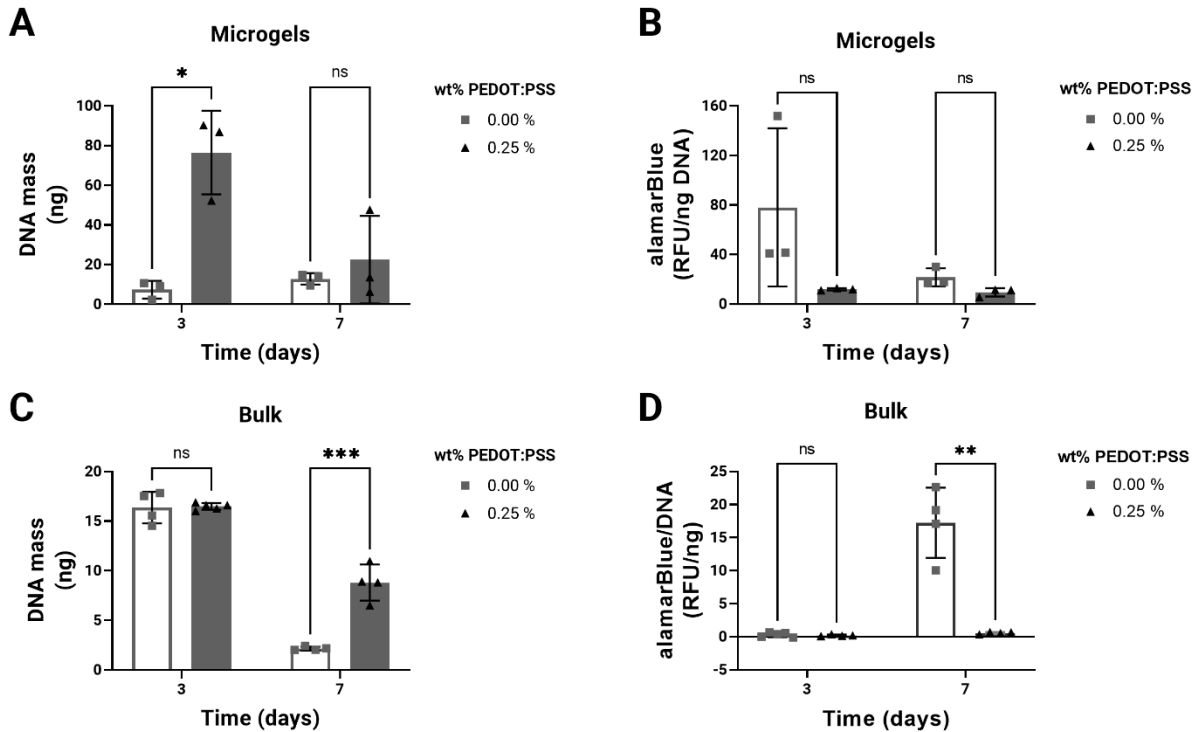


Figure 5.2 Microgel structure promotes C2C12 proliferation compared to bulk hydrogels. (A) DNA content of C2C12s in annealed microgel scaffolds demonstrate conducive scaffolds promoted myoblast proliferation at 3d (n=3, *p≤0.05). **(B)** When normalized to DNA content, metabolic activity appears lower in myoblasts on conductive gels at 3d, which may suggest cells undergoing differentiation (n=3). **(C)** C2C12s cultured in bulk degradable hydrogels had lower proliferation overall, though the conductive hydrogels supported myoblasts better at 7d than non-conductive controls (n=4, ***p≤0.001). **(D)** When normalized to DNA content, the metabolic activity of C2C12s on bulk degradable gels was minimal, indicating the advantage of microporous materials

over nanoporous ones (n=4, **p≤0.01). Groups were compared using multiple, unpaired t-tests where ns = not significant.

5.3.3 C2C12 differentiation is aided by microporous structure and conductivity

The myogenic differentiation of C2C12s seeded in microgel scaffolds was analyzed at 3 and 7d post-seeding via PCR. The early myogenic marker, MyoD (Myod1), did not offer a conclusive pattern in gene expression in response to microgel porosity or conductivity (**Figure 5.3A**). The expression of the slightly later myogenic marker, myogenin (Myog), indicated cell response was unaffected by substrate conductivity, but was sensitive to hydrogel structure and time (**Figure 5.3B**). While Myog expression was generally downregulated compared to the control, it was higher at 3 than at 7d, as expected. No changes in gene expression were observed when cells were seeded in bulk degradable controls. Expression of the later myogenic marker, myosin heavy chain (Myh7), suggested potential interactions between conductivity, physical structure, and time (**Figure 5.3C**). Most notably, there was a significant increase in Myh7 expression by cells maintained in conductive microgel scaffolds compared to the non-conductive group at 7d. Few differences existed between the remaining interactions, though a trend for greater Myh7 expression was observed in the cells grown in conductive bulk gels at 7d compared to those in their non-conductive counterpart, as well. When the interactions between time, physical properties, and electrical properties were analyzed with a three-way ANOVA, Myh7 expression was influenced by the combination of time and electrical cues (p=0.0002) as well as time and physical cues (p=0.0073).

Immunostaining for MHC was much more pronounced in conductive microgels at 7d compared to non-conductive controls (**Figure 5.3D**). Although nuclei staining indicated good cell distribution within the microgel scaffolds, there was no discernable MHC staining at 3d for either microgel group. C2C12s seeded on bulk degradable gels had minimal activity, as evidenced by their rounded morphology and minimal MHC staining. Cells were also stained for myogenin, but signal was limited and only visible when cells were cultured in the conductive microgel scaffolds for 7 days. The immunostaining data corroborates the MHC gene expression analysis and affirms both physical and electrical properties of a material influence cell differentiation.

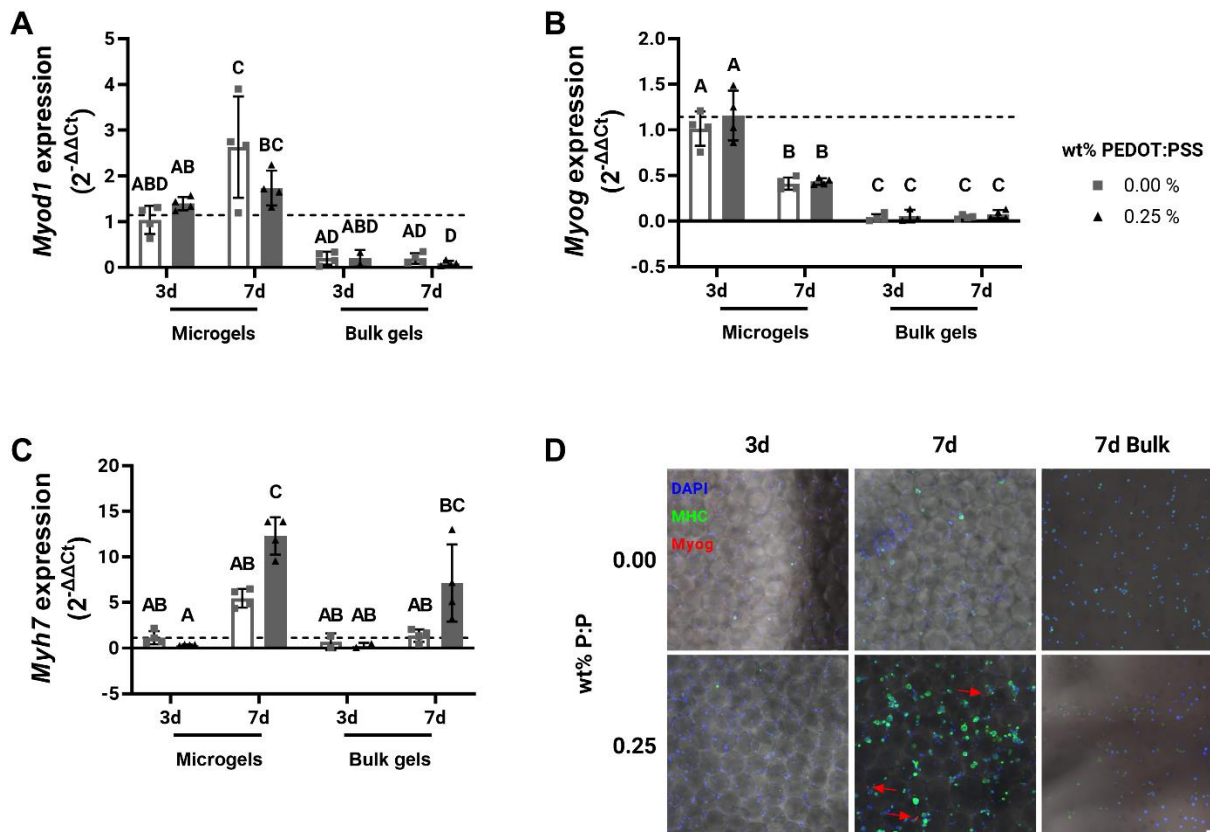


Figure 5.3 Microgel structure aids in expression of early myogenic markers of C212s, and conductivity further enhances expression of late myogenic markers.

(A) Expression of the early myogenic gene, Myod1, is not significantly affected by either the electrical or physical properties of the microgel annealed scaffolds (n=2-4). **(B)** Myogenin gene expression (Myog) was not dependent upon scaffold conductivity but was significantly different in response to scaffold porosity and time (n=3-4). **(C)** Expression of the gene for myosin heavy chain (Myh7) suggest conductivity, porosity, and time each contribute to cell response. Notably, Myh7 expression 7 days after C2C12s were seeded in conductive microgels was significantly higher than those cultured in the non-conductive control and both microgel groups on 3d (n=2-4). The displayed statistics were generated using a two-way ANOVA. Groups denoted with different letters are significantly different. Groups that share letters are statistically similar. **(D)** Immunofluorescence staining of C2C12s demonstrate an upregulation in myosin heavy chain (MHC) protein expression when cultured in conductive microgel scaffolds. Trace myogenin (red arrows) was observed in this group, as well, and was not present in cells grown in the non-conductive gels or bulk gels at both time points. Scale = 100 μ m.

5.3.4 Conductive microgels promote myogenic differentiation of skMDCs at early timepoints

Human skeletal muscle-derived cells (skMDCs) were used as a more clinically relevant in vitro model to probe the role of biomaterial porosity and conductivity on myogenic differentiation. Similar to the studies performed with C2C12s, myogenic potential was interrogated on the transcript and protein level. qPCR results indicated that at 1d, Myod1 gene expression was upregulated in the conductive microgel scaffolds over the non-conductive controls (**Figure 5.4A**). Since Myod1 is involved in cell cycle arrest

associated with differentiation, these data indicate differentiation is initiated sooner in conductive scaffolds. By 7d, the non-conductive microgels appear to boost the expression of Myod1 over the conductive group, though the results are not significant. Trends indicate Myog expression was upregulated in cells cultured in non-conductive scaffolds, though these results are only significant on 7d (**Figure 5.4B**). Myosin heavy chain transcript levels were not detectable on 1d, but by 7d, trends suggest greater Myh7 expression by cells in the non-conductive scaffolds (**Figure 5.4C**). However, when myosin heavy chain protein levels were assessed via immunostaining, there appeared to be similar expression between the conductive and non-conductive groups at all timepoints (**Figure 5.4D**). Cells in the conductive scaffolds had fewer punctate staining patterns than those in the non-conductive group, particularly after 1d, indicating more robust cell structures. Further, there are clearer indications of multinucleated cell bodies in the conductive scaffolds on 7d. Both observations point to the ability of conductive biomaterials to promote myogenic differentiation of a clinically relevant cell model.

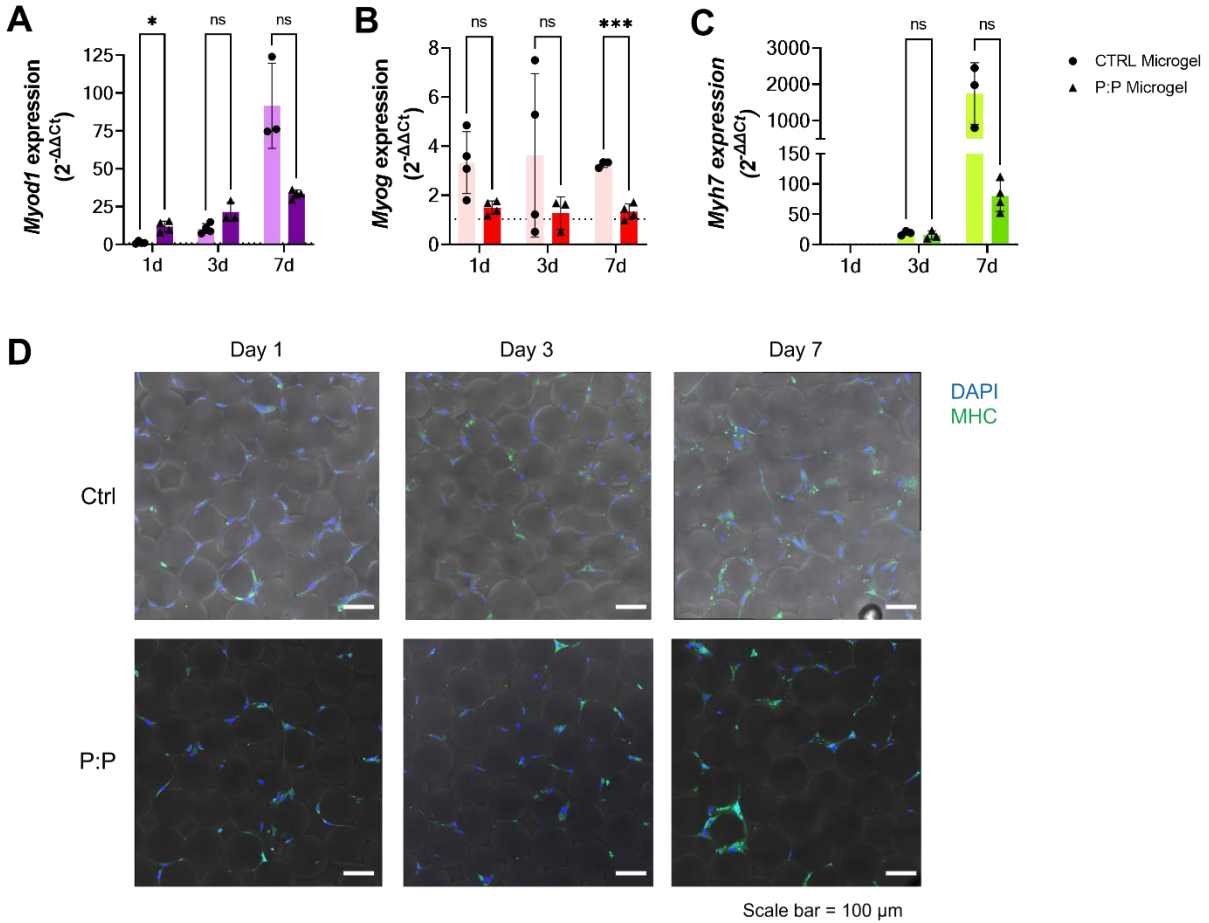


Figure 5.4 Conductive microgel scaffolds promote myogenic differentiation of skMDCs at early timepoints. (A) Myod1 gene expression was significantly higher on 1d when skMDCs were cultured in conductive microgel scaffolds, which points to enhanced initiation of myogenic differentiation (n=3-4, *p≤0.05). Over time, there appeared to be greater Myod1 expression by cells in the non-conductive scaffolds, but relationships were not significant. **(B)** Myog gene expression seemed to be downregulated in cells cultured in the conductive microgel scaffolds compared to the non-conductive group, though results were only significant on 7d (n=3-4, ***p≤0.001). **(C)** Myh7 expression was not detectable in cells on 1d. By 7d, there appeared to be greater myosin heavy chain gene

expression in the non-conductive gels over the conductive gels, though the relationship was not statistically significant (n=3-4, ns=not significant). Statistical analyses of qPCR data were generated using multiple unpaired t-tests with Holm-Šídák correction. **(D)** Immunofluorescence staining of skMDCs demonstrate similarities in myosin heavy chain (MHC) protein expression of cells cultured in conductive or non-conductive microgel scaffolds. However, cells in the conductive scaffolds had more robust MHC staining on 3 and 7d compared to those in the non-conductive group. On 7d, multinucleated cell bodies were visible in the conductive scaffolds only, indicating better myogenic potential of skMDCs in the conductive microgel scaffolds. Scale = 100 μ m.

5.3.5 Conductive microgel scaffolds enhance secretion of cytokines related to myogenic differentiation and wound healing

Myogenic gene and protein expression differed slightly in skMDCs compared to the clear correlation between gene and protein expression in C2C12s. Therefore, we investigated if the skMDCs secreted other myogenic or regenerative factors in response to conductivity. After investigating 80 different analytes via a multiplex protein array, we identified 6 factors of interest that skMDCs expressed in greater quantities in conductive microgel scaffolds during at least at one time point. IL-6 (**Figure 5.5A**) and IL-8 (**Figure 5.5B**) are pro-inflammatory cytokines that are critical for proper wound healing. Both factors were secreted in increased quantities by cells in conductive scaffolds at 3d. At the other time points, these factors are expressed more by cells in the non-conductive scaffolds. Pro-epidermal growth factor (EGF) was expressed nearly identically by cells in conductive and non-conductive scaffolds, except on 3d (**Figure 5.5C**). Muscle cells in

conductive scaffolds secreted more VEGF on 1d, and the effect was maintained through 3d (**Figure 5.5D**). Insulin-like growth factor (IGF-1) was expressed much more by cells in conductive scaffolds on 3d (**Figure 5.5E**). IGF-binding protein (IGFBP -2) was also expressed more by cells in conductive microgel scaffolds on 1d and 3d, though the effect waned over time (**Figure 5.5F**). IGF-1 is implicated in muscle cell growth via hypertrophy and IGFBP-2 prolongs the half-life of IGF-1. These data indicate that when skMDCs are grown on conductive scaffolds, they have greater myogenic potential at early time points. Trends in how other factors were secreted imply that the wound healing or regenerative capacity of skMDCs may be enhanced at earlier timepoints in response to electroactive cues.

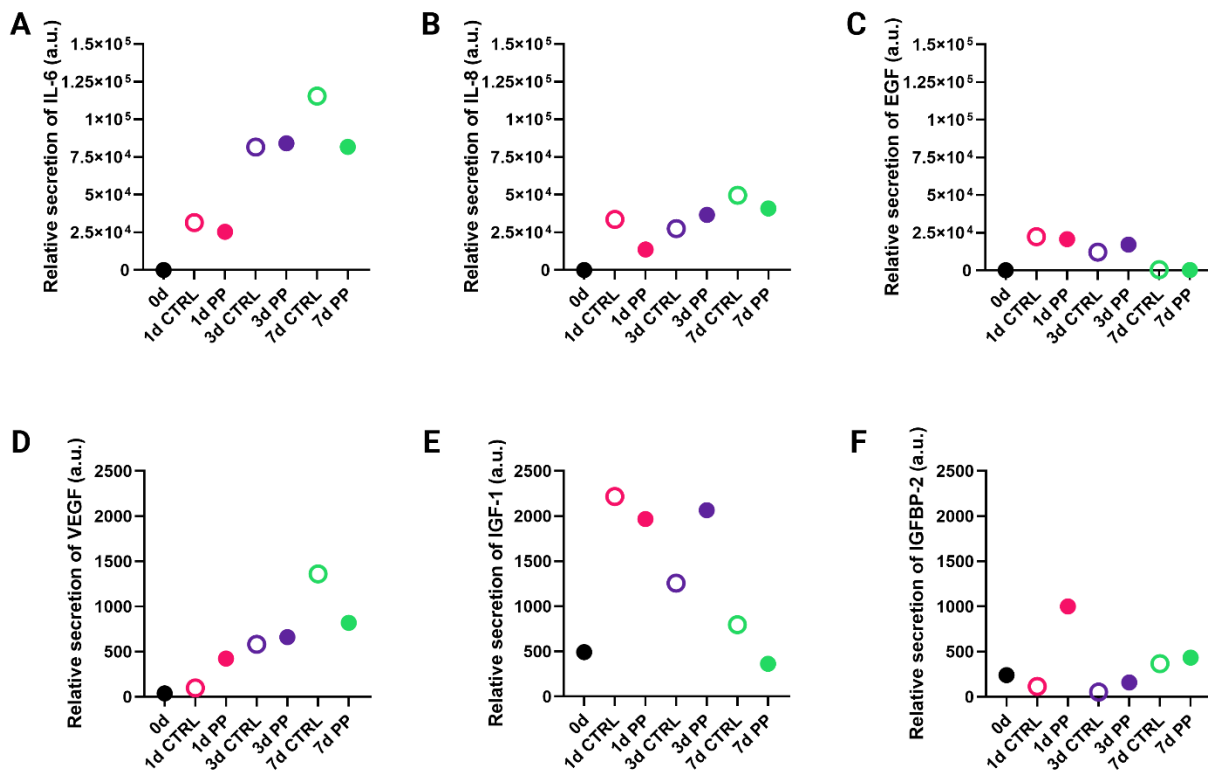


Figure 5.5 Conductive microgel scaffolds enhance early secretion of several cytokines related to myogenic differentiation and wound healing. An 80-analyte

array was used to profile changes in skMDC secretion in response to scaffold conductivity. **(A)** IL-6 and **(B)** IL-8 are both pro-inflammatory cytokines that play a critical role in the wound healing process and were secreted more by skMDCs in the conductive microgel scaffolds on 3d. **(C)** EGF and **(D)** VEGF are also essential factors for wound healing and were secreted more by skMDCs in conductive microgels at early timepoints. **(E)** IGF-1 upregulation is linked to muscle growth via hypertrophy and the **(F)** IGFBP -2 prolongs the half-life of IGF. skMDCs cultured in conductive microporous scaffolds secreted these factors more on 1d and 3d, which has positive implications for early muscle cell repair. Statistical comparison is not possible due to singular replicates for each analyte.

5.4 Discussion

Biophysical and electrical properties of biomaterials used as cell carriers are critical for directing cell behavior and can synergistically promote cell differentiation and maturation. In this work, we developed conductive microgel annealed scaffolds to interrogate myogenic differentiation of murine and human myoblastic cells. While granular scaffolds have been used to investigate many tissue types,^[6,25–28] no studies have reported the benefit of combining the microporosity of microgel annealed scaffolds with conductive polymers. Herein, we demonstrate the ability of conductive microgel annealed scaffolds to enhance myoblast differentiation and maturity.

When entrapped in a biomaterial, it is essential for cells to migrate and proliferate to achieve their therapeutic potential.^[29,30] This critical function motivates the use of naturally derived biomaterials that are vulnerable to degradation by cell-secreted

endogenous proteases or the design of synthetic biomaterials that are enzymatically or hydrolytically degradable to permit cellular invasion.^[31] However, this approach still necessitates delays for material remodeling after cells are implanted. Unlike traditional bulk hydrogels, microgel annealed scaffolds possess inherent void space in between the particles which permit immediate cell migration. Microgel fragments have been employed to create materials with highly tunable mechanical properties.^[32] While these fragments boast a facile workflow, they face the limitation of inconsistent void volumes and unpredictable cell response.^[7] In contrast, the monodisperse nature of microfluidic-produced microgels, as employed here, ensures consistent, predictable, and tunable void space and resultant materials properties.

To further augment the bioactivity of microgels, we used PEDOT:PSS in this work to imbue the microgels with conductive properties. PEDOT:PSS is a conductive polymer frequently used for fabricating conductive biomaterials owing to its commercial availability and its dispersant nature when suspended in water. The hydrophobic PEDOT⁺ core is surrounded by a shell of PSS⁻, which forms micelles that can evenly distribute within a water-based material, such as hydrogels.^[33] This contrasts starkly to other commonly used synthetic conductive materials such as polypyrrole, polyaniline, and graphene. Despite high levels of electrical conductivity, these materials require further chemical processing to overcome their hydrophobic properties for incorporation into hydrogels. Although addition of PEDOT:PSS into the PEG microgels caused the conductivity of annealed scaffolds to double, it did not affect the compressive modulus of individual microgels or the storage modulus of annealed scaffolds. The hydrogel system employed

herein had completely decoupled electrical and mechanical properties, allowing for the interrogation of how these properties individually influence cell behavior.

Bioelectrical components have been previously incorporated into hydrogels for use in muscle tissue engineering, which achieved similar electrical properties as reported here.^[13] The PEDOT:PSS-containing microgel scaffold conductivity was approximately 3.5×10^{-6} S/cm, which is within a similar order of magnitude of other studies using PEDOT:PSS and polypyrrole.^[17,34] Though each of these studies characterizes changes in mechanical properties with the inclusion of conductive additives, few specifically interrogate the interplay of biomaterial electrical and physical properties on influencing cell response. The novelty of this work includes the examination of macroporosity as a physical property and how it interacts with electroactivity to affect cell behavior and myogenic differentiation.

The results of these studies established that both microporosity and conductivity were essential attributes for directing C2C12 myoblast differentiation in these hydrogels. Microgel annealed scaffolds promoted increased proliferation and gene expression compared to bulk scaffolds. We observed significantly greater DNA content when C2C12s were cultured in conductive microgel scaffolds compared to non-conductive controls, yet the metabolic activity of those cells was much lower, indicating myogenic differentiation. These results corroborate other studies in the literature demonstrating lower metabolic activity in differentiating cells.^[24] Furthermore, when probing for myogenic markers, we observed a stark increase in myosin heavy chain gene and protein expression in the C2C12s grown in the conductive scaffolds at later time points. Myosin heavy chain is a hallmark indicator for muscle cells that are maturing from myoblasts to more functional

myotubes. Markers that define earlier stages of myogenic differentiation include MyoD and myogenin, which we also interrogated.^[35–37] The expression of Myod1 was not dependent on microporosity or conductivity, and myogenin was affected mainly by scaffold physical structure and time. Other studies investigating muscle cell differentiation demonstrate strong MyoD expression at time points earlier than we measured. Additionally, since our hypothesis was that conductive microporous materials would promote myogenic differentiation, it is possible that the window in which MyoD and myogenin are expressed was narrowed outside of a feasible detectable limit. Future work could include assessing changes in myoblastic cells at the gene and protein level at earlier time points. Together, these data indicate that physical and electrical cues can effectively differentiate C2C12s without additional chemicals beyond what is suggested for myoblast culture.

Human skeletal muscle derived cells (skMDCs) were next seeded into microgel scaffolds to investigate a more clinically relevant cell type. skMDCs experienced an earlier upregulation of early-stage marker Myod1 in conductive microgels compared to non-conductive microgels, but no difference in late-stage marker Myh7. Immunofluorescent staining further confirmed a similar level of MHC expression in both conductive and non-conductive microgels. We next investigated skMDC secretome to see if conductivity influences secreted myogenic or regenerative factors. IGF-1, a growth factor associated with myofiber hypertrophy and regeneration in skeletal muscle,^[38,39] was higher in conductive microgels scaffolds at 3d compared to non-conductive microgel scaffolds. IBGFBP-2, another factor associated with myogenesis,^[40,41] was sharply increased at 1d

in conductive microgel scaffolds. Taken together, these factors indicate conductive microgel scaffolds promote myogenesis at earlier timepoints.

While the microporosity of these gels provides exciting opportunities to enhance cell proliferation and migration, microgel annealed scaffolds are limited by the random porosity inherent in their structure. Surface topography and muscle cell alignment is vital in myogenic differentiation due to the highly organized structure of muscle.^[3,42] Future work may consider orienting the microgels into an aligned structure through the application of an external electric field^[43–45] or bioprinting.^[46–48] Additionally, while MHC expression was visibly upregulated on conductive microgels on day 7, we did not observe myocyte fusion into myotubes. This may be improved with higher seeding density into the annealed constructs or incorporating mechanisms for the material to degrade and thus make room for myotubes to assemble.

To our knowledge, this is the first report of conductive, microporous microgel annealed scaffolds for muscle tissue engineering. Both electrical and biophysical properties were integral for promoting myoblast differentiation at both the gene and protein level. The bioactivity and injectable nature of the microgel scaffolds make them a promising tool for clinical translation to heal muscle wounds. Future work will investigate the translation of this platform in an in vivo model such as volumetric muscle loss.

5.5 References

- [1] B.T. Corona, J.C. Rivera, J.G. Owens, J.C. Wenke, C.R. Rathbone, Volumetric muscle loss leads to permanent disability following extremity trauma, *J. Rehabil. Res. Dev.* 52 (2015) 785–92.
- [2] H. Manring, E. Abreu, L. Brotto, N. Weisleder, M. Brotto, Novel excitation-contraction coupling related genes reveal aspects of muscle weakness beyond atrophy—new hopes for treatment of musculoskeletal diseases, *Front. Physiol.* 5 (2014).
- [3] S. Jana, S.K.L. Levengood, M. Zhang, Anisotropic Materials for Skeletal-Muscle-Tissue Engineering, *Adv. Mater.* 28 (2016) 10588–10612.
- [4] J.M. Grasman, M.J. Zayas, R.L. Page, G.D. Pins, Biomimetic scaffolds for regeneration of volumetric muscle loss in skeletal muscle injuries, *Acta Biomater.* 25 (2015) 2–15.
- [5] R. Lev, D. Seliktar, Hydrogel biomaterials and their therapeutic potential for muscle injuries and muscular dystrophies, *J. R. Soc. Interface.* 15 (2018) 20170380.
- [6] J.P. Newsom, K.A. Payne, M.D. Krebs, Microgels: Modular, tunable constructs for tissue regeneration, *Acta Biomater.* 88 (2019) 32–41.
- [7] J.M. Lowen, G.C. Bond, K.H. Griffin, N.K. Shimamoto, V.L. Thai, J.K. Leach, Multisized Photoannealable Microgels Regulate Cell Spreading, Aggregation, and Macrophage Phenotype through Microporous Void Space, *Adv. Healthcare Mater.* (2023) 2202239.
- [8] A.R. Anderson, E. Nicklow, T. Segura, Particle fraction is a bioactive cue in granular scaffolds, *Acta Biomater.* 150 (2022) 111–127.

- [9] M. Shin, K.H. Song, J.C. Burrell, D.K. Cullen, J.A. Burdick, Injectable and Conductive Granular Hydrogels for 3D Printing and Electroactive Tissue Support, *Adv. Sci.* 6 (2019) 1901229.
- [10] A. Casella, A. Panitch, J.K. Leach, Endogenous Electric Signaling as a Blueprint for Conductive Materials in Tissue Engineering, *Bioelectricity.* 3 (2021) 27–41.
- [11] X. Liu, A.L.M. Li, S. Park, B.E. Waletzki, A. Terzic, M.J. Yaszemski, L. Lu, Covalent crosslinking of graphene oxide and carbon nanotube into hydrogels enhances nerve cell responses, *J. Mater. Chem. B.* 4 (2016) 6930–6941.
- [12] B.W. Walker, R.P. Lara, C.H. Yu, E.S. Sani, W. Kimball, S. Joyce, N. Annabi, Engineering a naturally-derived adhesive and conductive cardiopatch, *Biomaterials.* 207 (2019) 89–101.
- [13] R. Dong, P.X. Ma, B. Guo, Conductive biomaterials for muscle tissue engineering, *Biomaterials.* 229 (2020) 119584.
- [14] M.-C. Chen, Y.-C. Sun, Y.-H. Chen, Electrically conductive nanofibers with highly oriented structures and their potential application in skeletal muscle tissue engineering, *Acta Biomater.* 9 (2013) 5562–5572.
- [15] S. Hosseinzadeh, M. Mahmoudifard, F. Mohamadyar-Toupkanlou, M. Dodel, A. Hajarizadeh, M. Adabi, M. Soleimani, The nanofibrous PAN-PANi scaffold as an efficient substrate for skeletal muscle differentiation using satellite cells, *Bioprocess Biosyst. Eng.* 39 (2016) 1163–1172.
- [16] K.D. McKeon-Fischer, D.P. Browe, R.M. Olabisi, J.W. Freeman, Poly(3,4-ethylenedioxythiophene) nanoparticle and poly(ϵ -caprolactone) electrospun

- scaffold characterization for skeletal muscle regeneration, *J. Biomed. Mater. Res., Part A.* 103 (2015) 3633–3641.
- [17] I.M. Basurto, M.T. Mora, G.M. Gardner, G.J. Christ, S.R. Caliarì, Aligned and electrically conductive 3D collagen scaffolds for skeletal muscle tissue engineering, *Biomater. Sci.* 9 (2021) 4040–4053.
- [18] J.M. de Rutte, J. Koh, D. Di Carlo, Scalable High-Throughput Production of Modular Microgels for In Situ Assembly of Microporous Tissue Scaffolds, *Adv. Funct. Mater.* 29 (2019) 1900071.
- [19] A. Casella, A. Panitch, J.K. Leach, Electroconductive agarose hydrogels modulate mesenchymal stromal cell adhesion and spreading through protein adsorption, *J. Biomed. Mater. Res., Part A.* 111 (2023) 596–608.
- [20] T. Gonzalez-Fernandez, A.J. Tenorio, A.M. Saiz Jr, J.K. Leach, Engineered Cell-Secreted Extracellular Matrix Modulates Cell Spheroid Mechanosensing and Amplifies Their Response to Inductive Cues for the Formation of Mineralized Tissues, *Adv. Healthcare Mater.* 11 (2022) 2102337.
- [21] G. Carpentier, Protein Array Analyzer for ImageJ, Gilles Carpentier Research Web Site: Computer Image Analysis. (2010).
http://image.bio.methods.free.fr/ImageJ/?Protein-Array-Analyzer-for-ImageJ.html&lang=en#outil_sommaire_0 (accessed June 12, 2023).
- [22] P.H. Mott, C.M. Roland, Limits to Poisson's ratio in isotropic materials, *Phys. Rev. B.* 80 (2009) 132104.
- [23] T. Gonzalez-Fernandez, P. Sikorski, J.K. Leach, Bio-instructive materials for musculoskeletal regeneration, *Acta Biomater.* 96 (2019) 20–34.

- [24] K. Martinez Villegas, R. Rasouli, M. Tabrizian, Enhancing metabolic activity and differentiation potential in adipose mesenchymal stem cells via high-resolution surface-acoustic-wave contactless patterning, *Microsyst. Nanoeng.* 8 (2022) 1–14.
- [25] A.C. Daly, L. Riley, T. Segura, J.A. Burdick, Hydrogel microparticles for biomedical applications, *Nat. Rev. Mater.* 5 (2020) 20–43.
- [26] K.L. Wilson, S.C.L. Pérez, M.M. Naffaa, S.H. Kelly, T. Segura, Stoichiometric Post-Modification of Hydrogel Microparticles Dictates Neural Stem Cell Fate in Microporous Annealed Particle Scaffolds, *Adv. Mater.* 34 (2022) 2201921.
- [27] A.S. Jeevarathinam, F. Guo, T. Williams, J.A. Smolen, J.A. Hyde, M.J. McShane, P. de Figueiredo, D.L. Alge, Enzyme functionalized microgels enable precise regulation of dissolved oxygen and anaerobe culture, *Mater. Today Bio.* 9 (2021) 100092.
- [28] L.J. Pruet, H.L. Kenny, W.M. Swift, K.J. Catallo, Z.R. Apsel, L.S. Salopek, P.O. Scumpia, P.S. Cottler, D.R. Griffin, J.J. Daniero, De novo tissue formation using custom microporous annealed particle hydrogel provides long-term vocal fold augmentation, *Npj Regener. Med.* 8 (2023) 10.
- [29] Q.L. Loh, C. Choong, Three-Dimensional Scaffolds for Tissue Engineering Applications: Role of Porosity and Pore Size, *Tissue Eng., Part B.* 19 (2013) 485–502.
- [30] N. Annabi, J.W. Nichol, X. Zhong, C. Ji, S. Koshy, A. Khademhosseini, F. Dehghani, Controlling the Porosity and Microarchitecture of Hydrogels for Tissue Engineering, *Tissue Eng., Part B.* 16 (2010) 371–383.

- [31] M.P. Lutolf, J.L. Lauer-Fields, H.G. Schmoekel, A.T. Metters, F.E. Weber, G.B. Fields, J.A. Hubbell, Synthetic matrix metalloproteinase-sensitive hydrogels for the conduction of tissue regeneration: Engineering cell-invasion characteristics, *Proc. Natl. Acad. Sci. U.S.A.* 100 (2003) 5413–5418.
- [32] V.G. Muir, S. Weintraub, A.P. Dhand, H. Fallahi, L. Han, J.A. Burdick, Influence of Microgel and Interstitial Matrix Compositions on Granular Hydrogel Composite Properties, *Adv. Sci.* 10 (2023) 2206117.
- [33] S. Zhang, Y. Chen, H. Liu, Z. Wang, H. Ling, C. Wang, J. Ni, B. Celebi-Saltik, X. Wang, X. Meng, H.J. Kim, A. Baidya, S. Ahadian, N. Ashammakhi, M.R. Dokmeci, J. Travas-Sejdic, A. Khademhosseini, Room-temperature-formed PEDOT:PSS hydrogels enable injectable, soft, and healable organic bioelectronics, *Adv. Mater.* 32 (2020) e1904752.
- [34] A.G. Guex, J.L. Puetzer, A. Armgarth, E. Littmann, E. Stavriniidou, E.P. Giannelis, G.G. Malliaras, M.M. Stevens, Highly porous scaffolds of PEDOT:PSS for bone tissue engineering, *Acta Biomater.* 62 (2017) 91–101.
- [35] H. Hwangbo, H. Lee, E. Jin, Y. Jo, J. Son, H.M. Woo, D. Ryu, G.H. Kim, Photosynthetic Cyanobacteria can Clearly Induce Efficient Muscle Tissue Regeneration of Bioprinted Cell-Constructs, *Adv. Funct. Mater.* 33 (2023) 2209157.
- [36] Y.-N. Jang, E.J. Baik, JAK-STAT pathway and myogenic differentiation, *JAK-STAT.* 2 (2013) e23282.
- [37] P. Fortini, E. Iorio, E. Dogliotti, C. Isidoro, Coordinated Metabolic Changes and Modulation of Autophagy during Myogenesis, *Front. Physiol.* 7 (2016) 237.

- [38] M.E. Coleman, F. DeMayo, K.C. Yin, H.M. Lee, R. Geske, C. Montgomery, R.J. Schwartz, Myogenic Vector Expression of Insulin-like Growth Factor I Stimulates Muscle Cell Differentiation and Myofiber Hypertrophy in Transgenic Mice, *J. Biol. Chem.* 270 (1995) 12109–12116.
- [39] A. Musarò, K. McCullagh, A. Paul, L. Houghton, G. Dobrowolny, M. Molinaro, E.R. Barton, H. L Sweeney, N. Rosenthal, Localized Igf-1 transgene expression sustains hypertrophy and regeneration in senescent skeletal muscle, *Nat. Genet.* 27 (2001) 195–200.
- [40] A.P. Sharples, N. Al-Shanti, D.C. Hughes, M.P. Lewis, C.E. Stewart, The role of insulin-like-growth factor binding protein 2 (IGFBP2) and phosphatase and tensin homologue (PTEN) in the regulation of myoblast differentiation and hypertrophy, *Growth Horm. IGF Res.* 23 (2013) 53–61.
- [41] C.W. Ernst, D.C. McFarland, M.E. White, Expression of insulin-like growth factor II (IGF-II), IGF binding protein-2 and myogenin during differentiation of myogenic satellite cells derived from the turkey, *Differentiation.* 61 (1996) 25–33.
- [42] H. Gao, J. Xiao, Y. Wei, H. Wang, H. Wan, S. Liu, Regulation of Myogenic Differentiation by Topologically Microgrooved Surfaces for Skeletal Muscle Tissue Engineering, *ACS Omega.* 6 (2021) 20931–20940.
- [43] W. Kim, H. Lee, C.K. Lee, J.W. Kyung, S.B. An, I.-B. Han, G.H. Kim, A Bioprinting Process Supplemented with In Situ Electrical Stimulation Directly Induces Significant Myotube Formation and Myogenesis, *Adv. Funct. Mater.* 31 (2021)

- [44] I.-C. Liao, J.B. Liu, N. Bursac, K.W. Leong, Effect of Electromechanical Stimulation on the Maturation of Myotubes on Aligned Electrospun Fibers, *Cell Mol Bioeng.* 1 (2008) 133–145.
- [45] M. Flaibani, L. Boldrin, E. Cimetta, M. Piccoli, P.D. Coppi, N. Elvassore, Muscle Differentiation and Myotubes Alignment Is Influenced by Micropatterned Surfaces and Exogenous Electrical Stimulation, *Tissue Eng., Part A.* 15 (2009) 2447–2457.
- [46] S. Ostrovidov, S. Salehi, M. Costantini, K. Suthiwanich, M. Ebrahimi, R.B. Sadeghian, T. Fujie, X. Shi, S. Cannata, C. Gargioli, A. Tamayol, M.R. Dokmeci, G. Orive, W. Swieszkowski, A. Khademhosseini, 3D Bioprinting in Skeletal Muscle Tissue Engineering, *Small.* 15 (2019) 1805530.
- [47] T. Fan, S. Wang, Z. Jiang, S. Ji, W. Cao, W. Liu, Y. Ji, Y. Li, N. Shyh-Chang, Q. Gu, Controllable assembly of skeletal muscle-like bundles through 3D bioprinting, *Biofabrication.* 14 (2021) 015009.
- [48] G.H. Yang, W. Kim, J. Kim, G. Kim, A skeleton muscle model using GelMA-based cell-aligned bioink processed with an electric-field assisted 3D/4D bioprinting, *Theranostics.* 11 (2021) 48–63.

Chapter 6: Results and Future Directions

This chapter summarizes the findings of Chapters 3-5 and discusses their implications. I highlight the limitations associated with this work and discuss future directions.

6.1 Results and Implications

In this dissertation, we aimed to establish an easy-to-use microgel platform that examined how microgel diameter, stiffness, and peptide presentation influenced clinically relevant cell types. Aim 1 focused on developing a rapid and robust microgel annealing system and interrogated how different microgel diameters influenced cell aggregation, spreading, and macrophage polarization. We successfully used photoannealing to assemble microgels in as little as 1 minute and formed microgel scaffolds that were 1 cm thick which demonstrated photoannealing works with clinically relevant dimensions. Rapid annealing is an important aspect for clinical accessibility as it minimizes the time a patient needs to remain static. Furthermore, the scaffolds withstood cyclical compression which is applicable to tissues which undergo cyclical force such as knee articular cartilage during locomotion.

The second part of Aim 1 examined how large and small microgels result in differences in void space and influence cell behavior. We first modeled how void space is related to microgel diameter and demonstrated how a larger microgel diameter results in increased porosity. The ability to predict void space is important as microgels can be designed to promote a specific porosity. We then demonstrated that although scaffolds of both microgel sizes promoted rapid spreading from cell spheroids, large microgel

scaffolds promoted increased cell aggregation. Finally, we assessed how macrophage phenotype is influenced by microgel size. Both *in vitro* and *in vivo*, we saw a decrease in M1 phenotype in large microgel scaffolds. Additionally, *in vivo* we saw an increase in M2 macrophages in the large microgel scaffolds. These results are significant as immune response is pivotal in determining if a biomaterial implant is successful.^[1] As a result, microgel diameter can be tuned to promote a pro-regenerative macrophage phenotype. This contributes to the growing body of work that has demonstrated pore size influences macrophage polarization.^[2,3]

In Aim 2 we investigated how microgels can be tuned to control MSC differentiation with the overarching goal of osteochondral repair. By modulating stiffness and adding instructive peptides, we successfully fabricated microgels that supported both osteogenic and chondrogenic differentiation, and which outperformed bulk gel controls. We used the modularity of the microgels to form a bilayer scaffold of chondrogenic and osteogenic microgels. Notably, there was seamless interface between the microgel layers, which is often not the case with bulk hydrogels which are prone to delamination.^[4] We saw increased osteocalcin deposition on the bone side of the scaffold, and increased aggrecan deposition on the cartilage side of the scaffold. Spatial transcriptomics confirmed osteogenic and chondrogenic genes were upregulated in their respective microgel regions. These findings demonstrate how microgel modularity can be harnessed to spatially direct MSC differentiation. Furthermore, this showcases the potential for microgels to mimic mechanical, chemical, and structural gradients found throughout the body.^[5,6]

Aim 3 of this work sought to apply microgels to muscle tissue by further functionalizing them with the conductive additive PEDOT:PSS. We used the microgel platform to examine the interplay of porosity and conductivity on myogenesis, an area which is currently lacking in study.^[7] We found both components to be critical in directing C2C12 myoblast differentiation, with C2C12s grown on conductive microgels expressing increased MHC compared to non-conductive microgels and conductive bulk gels. When conductive microgel scaffolds were seeded with human skeletal muscle derived cells, a more clinically relevant cell type, they promoted earlier expression of myogenic markers. Aim 3 showcases the ability of microgels to be further functionalized with bioinstructive additives, and that microporosity can act synergistically with conductivity.

Taken together, Aims 1-3 demonstrate the versatility of microgels. Microgels outperformed their bulk counterparts in all studies, increasing cell proliferation, migration, and differentiation. Their microporosity makes them superior to bulk gels, and their modularity makes them ideal for repairing complex tissues. Furthermore, their injectability makes them a promising candidate for use in the clinic.

6.2 Future Directions and Limitations

This dissertation describes a rapidly annealing microgel platform applicable to wide variety of tissue types. We primarily used *in vitro* models to study how microgels influence cells, with short term subfascial implantations performed to study preliminary cell interactions *in vivo*. The next step for these experiments would be to fabricate microgels suitable for long-term implantation *in vivo*, implant them in their relevant tissue types, and continue to optimize microgel properties to guide cell behavior.

In Aim 1, we established a PEG-VS microgel platform that can anneal both small and large microgels with UV light with the photoinitiator VA-086. However, this wavelength is highly absorbed by tissue and may pose an issue if wanting to non-invasively implant scaffolds deep beneath the skin.^[8] It would be beneficial to explore annealing with further-penetrating visible wavelengths which is possible with photoinitiators such as Eosin Y.^[9] Another limitation is the reliance on adding additional crosslinker before annealing. Microgel chemistry using heterofunctional maleimide/methacrylamide (MethMal) has recently been developed which separates the initial microgel gelation functional group from the annealing moiety, and would bypass the need for this additional step.^[9] Additionally, further efforts would need to explore crosslinkers outside of the non-degradable PEG-DT. For implantation *in vivo*, it would be necessary to design formulations using degradable crosslinkers such as the MMP-susceptible crosslinker GPQ-A used in our bulk gels. It would also be beneficial to extend our cryopreservation experiment beyond one month to ensure long-term storage is viable for our microgel chemistries.

In Aim 2 we developed osteogenic and chondrogenic microgels. While we saw significant changes in osteogenic and chondrogenic markers on each side of the osteochondral bilayer scaffold, markers from both lineages were ubiquitously present. While this could partially be attributed to the exogenous signals from the mixed media, a larger gradient in osteochondral markers would increase the significance of this work. Future studies might examine adding other instructive cues such as TGF- β ^[10] or BMP-2 loaded hydroxyapatite nanoparticles.^[11] Another limitation is the discrete nature of the bilayer construct we designed. To replicate the native continuous gradient, another

method of fabrication may be necessary such as syringe pumps operating at inverse flow rates to create a gradient from one microgel population to the other.^[12] Finally, a rabbit osteochondral defect model would verify the microgels' ability to facilitate osteochondral repair *in vivo*. The *in situ* cues from the native bone and cartilage could promote a natural gradient throughout the scaffold.

In Aim 3 we designed a conductive microgel scaffold which promoted differentiation of myoblastic cells. One limitation of using a microgel scaffold is the tortuous porosity found throughout. The structured alignment of muscle along with surface topography has been shown to be vital in myogenic differentiation.^[13] As a result, further efforts may consider an alignment mechanism such as 3D printing. Additionally, we observed limited myocyte fusion into myotubes. This could be improved by seeding at a higher density, or potentially with the addition of a degradable crosslinker. Similar to the osteochondral microgels, this work would benefit from an *in vivo* component such as a murine model of volumetric muscle loss.

Finally, the overarching goal of this research is to see translation from the bench to the clinic. Microgels represent a promising therapeutic due to their injectability, versatility, and ability to be cryopreserved. Given the time-consuming process of clinical trials and FDA approval, it is important to identify a microgel platform in terms of fabrication, annealing, and formulation that can be consistently used across treatments. Once a universal base formulation is established, it will be easier to build upon preexisting chemistries to treat a variety of tissue types.

6.3 Final Conclusions

As tissue engineering continues to advance there is a growing need for personalized medicine which can match the complexity of the human body. Microgels are a step towards fulfilling that role, offering tunability, modularity, and clinical accessibility. This work contributes to the growing field of knowledge and tools we can use to heal damaged tissue.

6.4 References

- [1] E. Mariani, G. Lisignoli, R.M. Borzì, L. Pulsatelli, Biomaterials: Foreign Bodies or Tuners for the Immune Response?, *Int. J. Mol. Sci.* 20 (2019) 636.
- [2] E.M. Sussman, M.C. Halpin, J. Muster, R.T. Moon, B.D. Ratner, Porous Implants Modulate Healing and Induce Shifts in Local Macrophage Polarization in the Foreign Body Reaction, *Ann. Biomed. Eng.* 42 (2014) 1508–1516.
- [3] L.J. Pruet, C.H. Jenkins, N.S. Singh, K.J. Catallo, D.R. Griffin, Heparin Microislands in Microporous Annealed Particle Scaffolds for Accelerated Diabetic Wound Healing, *Adv. Funct. Mater.* 31 (2021) 2104337.
- [4] B.A. Harley, A.K. Lynn, Z. Wissner-Gross, W. Bonfield, I.V. Yannas, L.J. Gibson, Design of a multiphase osteochondral scaffold III: Fabrication of layered scaffolds with continuous interfaces, *J. Biomed. Mater. Res.* 92A (2009) 1078–1093.
- [5] J.M. Lowen, J.K. Leach, Functionally Graded Biomaterials for Use as Model Systems and Replacement Tissues, *Adv. Funct. Mater.* 30 (2020) 1909089.
- [6] A. Pattnaik, A.S. Sanket, S. Pradhan, R. Sahoo, S. Das, S. Pany, T.E.L. Douglas, R. Dandela, Q. Liu, J. Rajadas, S. Pati, S.C. De Smedt, K. Braeckmans, S.K. Samal, Designing of gradient scaffolds and their applications in tissue regeneration, *Biomaterials.* 296 (2023) 122078.
- [7] R. Lev, D. Seliktar, Hydrogel biomaterials and their therapeutic potential for muscle injuries and muscular dystrophies, *J. R. Soc. Interface.* 15 (2018) 20170380.
- [8] J.L. Sandell, T.C. Zhu, A review of in-vivo optical properties of human tissues and its impact on PDT, *J. Biophoton.* 4 (2011) 773–787.

- [9] B.N. Pfaff, L.J. Pruetz, N.J. Cornell, J. de Rutte, D. Di Carlo, C.B. Highley, D.R. Griffin, Selective and Improved Photoannealing of Microporous Annealed Particle (MAP) Scaffolds, *ACS Biomater. Sci. Eng.* 7 (2021) 422–427.
- [10] Y. Deng, A.X. Sun, K.J. Overholt, G.Z. Yu, M.R. Fritch, P.G. Alexander, H. Shen, R.S. Tuan, H. Lin, Enhancing chondrogenesis and mechanical strength retention in physiologically relevant hydrogels with incorporation of hyaluronic acid and direct loading of TGF- β , *Acta Biomater.* 83 (2019) 167–176.
- [11] J. Whitehead, A. Kothambawala, J. Kent Leach, Morphogen Delivery by Osteoconductive Nanoparticles Instructs Stromal Cell Spheroid Phenotype, *Adv. Biosys.* 3 (2019) 1900141.
- [12] O. Jeon, D.S. Alt, S.W. Linderman, E. Alsberg, Biochemical and Physical Signal Gradients in Hydrogels to Control Stem Cell Behavior, *Adv. Mater.* 25 (2013) 6366–6372.
- [13] S. Jana, S.K.L. Levengood, M. Zhang, Anisotropic Materials for Skeletal-Muscle-Tissue Engineering, *Adv. Mater.* 28 (2016) 10588–10612.